Focused Ion Beam Created Refractive and Diffractive Lens Techniques for the Improvement of Optical Imaging through Silicon

vorgelegt von

Dipl.-Ing.

Philipp Scholz

aus Berlin

Von der Fakultät IV - Elektrotechnik und Informatik
der Technischen Universität Berlin
zur Erlangung des akademischen Grades
Doktor der Ingenieurwissenschaften
Dr.-Ing.

genehmigte Dissertation

Promotionsausschuss:
Vorsitzender: Prof. Dr.-Ing. Stephan Völker
Berichter: Prof. Dr.-Ing. Christian Boit
Berichter: Prof. Derryck T. Reid

Tag der wissenschaftlichen Aussprache: 19.12.2011

Berlin 2012

D 83

Zusammenfassung

In ihrem Kern befasst sich diese Arbeit mit der Erzeugung refraktiver und diffraktiver Festkörperimmersionslinsen (SILs) aus Silizium (Si) mit einer fokussierten Ionenstrahlanlage (FIB). SILs werden zur optischen Auflösungsoptimierung benötigt, wenn aktive Gebiete nur durch die Rückseite des Chips untersucht werden können. Kommerzielle SIL-Objektive lassen sich, z.B. bei engen Gehäuseöffnungen, nur eingeschränkt nutzen. FIB-erzeugte SILs können an beliebiger Stelle geformt werden. Zwei Konzepte werden präsentiert: kugelförmige refraktive SILs (rSILs) für spektral breitbandige Analysen, jedoch nicht leicht in großen Dimensionen herzustellen, und binäre diffraktive SILs (dSILs), nur für monochromatisches Licht aber aus flachen Strukturen auf großen Flächen realisierbar. Drei konkrete Modelle FIB-erzeugter SILs wurden entwickelt: eine dSIL und zwei rSILs, wobei rSIL (1) durch reines FIB-Fräsen erzeugt wird und rSIL (2) durch gasunterstütztes FIB-Ätzen. Die rSIL-Kugelstruktur wird auf Segmente begrenzt, um einen effizienten und machbaren FIB-Prozess zu erreichen. rSIL (1) benötigt weniger als 20 Min. Prozesszeit und verbessert die mikroskopische Auflösung um den Faktor 1,8. rSIL (1) wurde auch mit einer Antireflexionsschicht verwendet, was die Anzahl erkennbarer Details sowie den Bildkontrast erheblich erhöhte. Die in weniger als 60 Min. geätzte rSIL (2) bietet einen größeren Öffnungswinkel. Eine noch größere SIL ließ sich mit der dSIL in 15 Min. Prozesszeit, ebenfalls durch FIB-Ätzen, erreichen. Wie rSIL (1) zeigten auch rSIL (2) und dSIL eine sichtbare Verbesserung in Auflösung und Kontrast. Das Potential der vorgestellten Technik ist eine numerische Apertur (NA) von 1,5 (rSIL) bzw. 2,5 (dSIL). Diese Perspektive sowie die präsentierten Versuchsergebnisse bilden die wissenschaftliche Grundlage, auf der sich FIB-erzeugte SILs zu wertvollen optischen Komponenten in der Funktionsanalytik von integrierten Schaltkreisen entwickeln lassen.

Abstract

The research core of this work is the creation of refractive and diffractive Solid Immersion Lenses (SILs), carved into silicon (Si) by a focused ion beam (FIB) machine. SILs are needed to optimize optical resolution, if active parts can only be analysed through the backside of an integrated circuit (IC). Commercial SIL objectives have limited application, e.g. close to edges of IC package openings. FIB created SILs can be formed at any requested location. Two concepts are presented: spherical refractive SILs (rSILs) for broad spectral application, but challenging to shape in large dimensions, and binary diffractive SILs (dSILs), requiring monochromatic light, made of shallow structures, possibly being created over large areas. Three specific models of FIB created SILs are developed: one dSIL and two rSILs, rSIL (1) shaped by unassisted FIB milling and rSIL (2) FIB-etched with gas assistance. The rSILs are spherical caps of a hemisphere to achieve an efficient and feasible FIB process. rSIL (1) needs less than 20 min processing time and improves the microscopic resolution by a factor of 1.8. rSIL (1) was also used with an anti-reflective coating, significantly improving visible details and image contrast. rSIL (2), FIB-etched in less than 60 min, offers a larger opening angle. An even larger lens shape was achieved by the dSIL created in 15 min also by FIB etching. Like rSIL (1), rSIL (2) and dSIL also demonstrate a visible improvement in resolution and contrast. The potential of this technique is a numerical aperture (NA) of at least 1.5 (rSIL) or 2.5 (dSIL). This perspective, along with the presented results and detailed process information, make this work the scientific basis upon which FIB-created SILs can be developed into valuable optical components for the functional analysis of integrated circuits.

Danksagung

Ich möchte besonders meinem Chef und Betreuer Prof. Christian Boit danken. Ich schätze seine wertvollen Ratschläge und seine Anleitung sehr. Seit meinen Anfängen als Tutor vor acht Jahren gab es keinen Tag, an dem ich es bereut habe, bei ihm zu arbeiten. Ich danke Prof. Derryck Reid für sein Interesse an meiner Arbeit und für mehr Licht in meiner Welt der Optik. Ted Lundquist wurde meine Verbindung zum Silicon Valley und eine stetige Inspiration, vielen Dank. Meinen Kollegen Rudolf Schlangen und Clemens Helfmeier sei gedankt, für große Unterstützung am OptiFIB, in der Lehre und in den Pausen. Clemens half zudem bei den Anfängen der Bitmap-Programmierung in Octave. Außerdem möchte ich danken: Uwe Kerst für die hilfsbereite Leitung unseres Labors; Andreas Eckert für Hilfe bei Probenpräparation und mehr; Frank Zachariasse für wertvolle Diskussionen über dSILs; meiner Frau Johanna, die mir Hoffnung gibt und mein Leben auch während dieser Arbeit in Ordnung gehalten hat; meinen Eltern Ute und Eckhard für Ihre Unterstützung in allem was ich tue, Ihren Glauben an mich und einfach dafür, dass sie tolle Eltern sind; meiner „amerikanischen Familie“ Sabina, Udo und Phillip für die Erweiterung meines sprachlichen Horizontes und eine zweite Heimat; meinen Schwiegereltern Anne und Rainer für alltägliche Hilfe und für ihre Tochter; meinem lieben Freund Henning für das gesellige Schreiben einer Doktorarbeit an fast jedem Tag der vergangenen drei Monate - möge die „Relevanz des Stakeholder Commitments im Sanierungsprozess“ die Welt retten. Außerdem danke ich Karl-Theodor zu Guttenberg. Wegen ihm hatte im letzten Jahr meiner Arbeit jeder einen schlauen Spruch parat. Und ja, ich habe alle meine Quellen angegeben. Abschließend möchte ich allen Mitarbeiterinnen und Mitarbeitern des Fachgebietes „Halbleiterbauelemente“ danken. Sie machen die TU nicht nur zu einem wichtigen Teil meiner Arbeit, sondern auch zu einem schönen Teil meines Lebens.

Acknowledgements

Most of all I want to thank my boss and mentor Prof. Christian Boit. I greatly value his advice and guidance on being a scientist and everything connected to it. There has not been one day in the past eight years during which I regretted joining his group and working with him from then on. I want to thank Prof. Derryck Reid for his interest in my work, and for shedding more light into my world of optics. Ted Lundquist became my link to the Silicon Valley and a consistent inspiration, thank you. Thanks go to my dear colleagues Rudolf Schlangen and Clemens Helfmeier. They were a great support at the OptiFIB, for teaching and at lunch time. Clemens also helped me in the initial phase of bitmap programming in Octave.

I further want to thank: Uwe Kerst for support and taking care of our lab; Andreas Eckert for helping out with sample preparation and much more; Frank Zachariasse for valuable discussions on dSILs; my wife Johanna, who always gives me hope and kept my life intact during the final part of the thesis, as well as before and after that; my parents Ute and Eckhard for supporting me in everything I do, believing in me and simply being great parents; my “American family” Sabina, Udo, and Phillip for broadening also my linguistic horizon and giving me a second home; my parents-in-law Anne and Rainer for their everyday help and their daughter; my dear friend Henning for joining me in writing a PhD thesis almost every single day in the past three months, and for keeping me sane - may “The Relevance of Stakeholder Commitment in Turnaround” save the world. I would also like to thank Karl-Theodor zu Guttenberg for giving everybody I talked to something to comment on during my last year of writing. And yes, I did cite all my sources. Finally I want to thank the staff and my colleagues at “Halbleiterbauelemente”, for making TUB not only a great place to work, but also a nice place to live.

Eidesstattliche Versicherung

Ich versichere an Eides statt, dass ich die vorliegende Dissertation selbstständig verfasst habe. Die benutzten Hilfsmittel und Quellen sind in der Arbeit vollständig angegeben.

Affidavit

I hereby declare that this thesis is my own work and that it contains no material previously published or written by another person, except where due acknowledgment has been made in the text.

"For myself I am an optimist
- it does not seem to be much use being anything else."

Sir Winston Churchill

Abbreviations

ARC	Anti-Reflective Coating
CAD	Computer-Aided Design
CMP	Chemical-Mechanical Polishing
dSIL	Diffractive Solid Immersion Lens
FIB	Focused Ion Beam
FOV	Field Of View
GUI	Graphical User Interface
LMIS	Liquid Metal Ion Source
LSM	Laser Scanning Microscope
NA	Numerical Aperture
OS	Operating System
PECVD	Plasma Enhanced Chemical Vapour Deposition
PEM	Photon Emission Microscopy
PMT	Photomultiplier Tube
RIE	Reactive Ion Etch
rSIL	Refractive Solid Immersion Lens
SEM	Scanning Electron Microscope
SIL	Solid Immersion Lens
SNR	Signal-to-Noise Ratio
TIFF	Tagged Image File Format
TUB	Technische Universität Berlin

(Referring to the department of Semiconductor Devices at TUB)

(..), ((..))	Equation, repeated Equation
[...] p. 1	Reference with page number
Fig. …	Figure
Tab. ...	Table
1.2.3	Chapter

Table of Contents

1 Optical imaging in the analysis of semiconductor devices - from Moore to SIL

Decades have passed since the invention of the transistor. Electronic devices with an amount of processing power for which entire buildings would have been needed not too long ago, are nowadays our daily companions, carried in our pockets. This evolution is partially owed to the development of integrated circuits (ICs). They combine diodes, transistors as well as passive components and can be produced cost efficiently in large quantities on silicon wafers. A schematic cross section of part a of an IC showing transistors connected via the metal layers can be seen in Fig. 1.

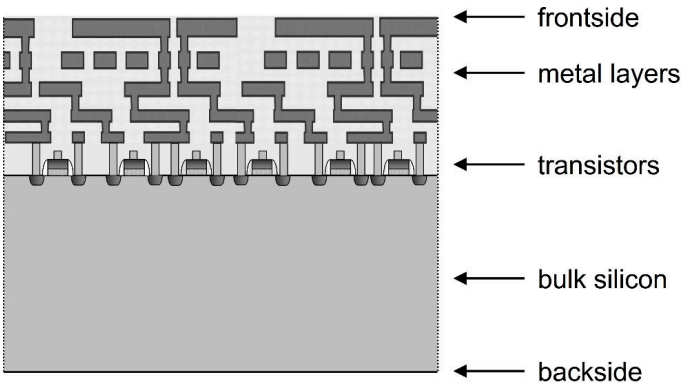

Fig. 1: Schematic cross section of a part of an integrated circuit illustrating transistors created on silicon (transistors and metal layers are not drawn to scale). While this figure shows only five metal layers, current technologies frequently use ten and more.

A key factor for the development in processing power is the increasing number of components realized in a single IC. This is possible due to a

decrease in the size of IC structures. Moore's law is generally quoted to describe the amount of transistors on a single chip, which is said to double every two years [1]. At the same time, the feature size, particularly the gate length of a field effect transistor (FET), is to decrease by a factor of 0.7 (Fig. 2) [2].

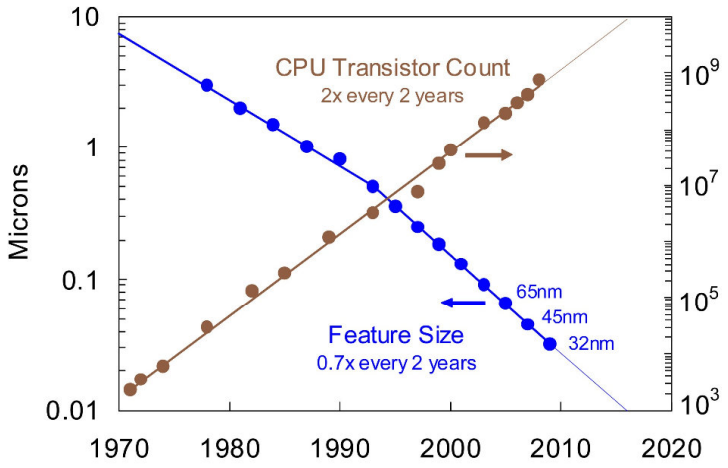

Fig. 2: Evolution and forecast of the transistor count on a single chip according to Moore's Law and of the feature size [2].

The increased amount of transistors also leads to an increase in connections, which are needed between the components and also need to be accessible from the outside. The first is being dealt with by more metal layers (compare Fig. 1) and the second addressed by flip chip package design. Both methods make an optical approach from the frontside of a microchip difficult or impossible.

Using optical means to inspect a microchip is part of the failure analysis (FA) process of semiconductor devices. FA plays a significant role in successfully manufacturing a product and establishing it in the markets. Samples come into FA because they showed faulty behaviour when being tested in production, during a reliability check right after production or while they were in use and returned by the (usually commercial) customer.

FA becomes particularly essential for producing a semiconductor device if a new type of technology process is used to create circuits of further reduced dimensions. It is then very likely that the first physical prototype (called "first silicon") does not perform the way it was expected from the software design and the simulations. Timing requirements, for example, might not be met. Therefore the device would not run at and could not be sold for the designated operating frequency.

Being able to deliver to the market earlier than competing companies is crucial to the success of a new semiconductor product. A key factor for a short time to market is the debugging of the first silicon, which partially consists of electrical testing and physical analysis. In practice, most failures can be identified by electrical testing. This is efficient and not as cost-intensive per chip, compared to a physical analysis, but does not always lead to the needed solution. A general overview of FA (including electrical testing and physical analysis) is given in Fig. 3.

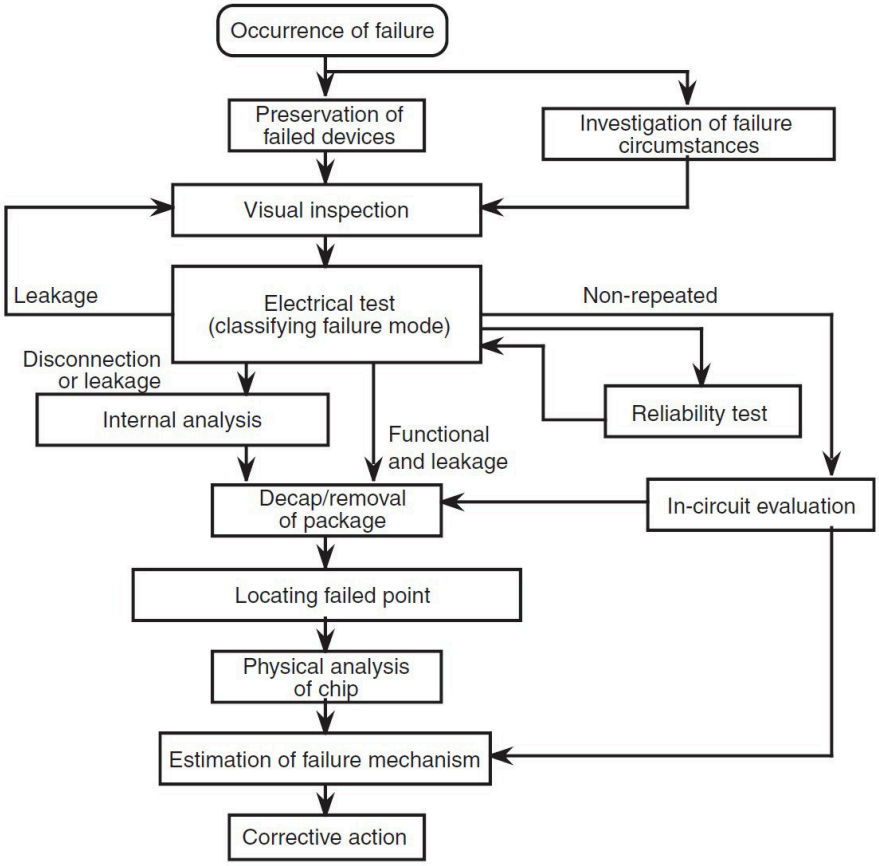

Fig. 3: General overview of a failure analysis process from [3]. The majority of failures can be dealt with by electrical testing. If a physical analysis (e.g. optically) is needed, it becomes essential for determining the corrective action, but it also consumes more time.

If electrical testing is not successful in identifying the failure, a physical analysis becomes necessary. Optical analysis and focused ion beam (FIB, see chapter 4.1) processing are two main aspects of the physical analysis. Fig. 4 explains under which circumstances these two might be applied in FA and also introduces an additional option for optical analysis: the solid immersion lens (SIL) [4], [5].

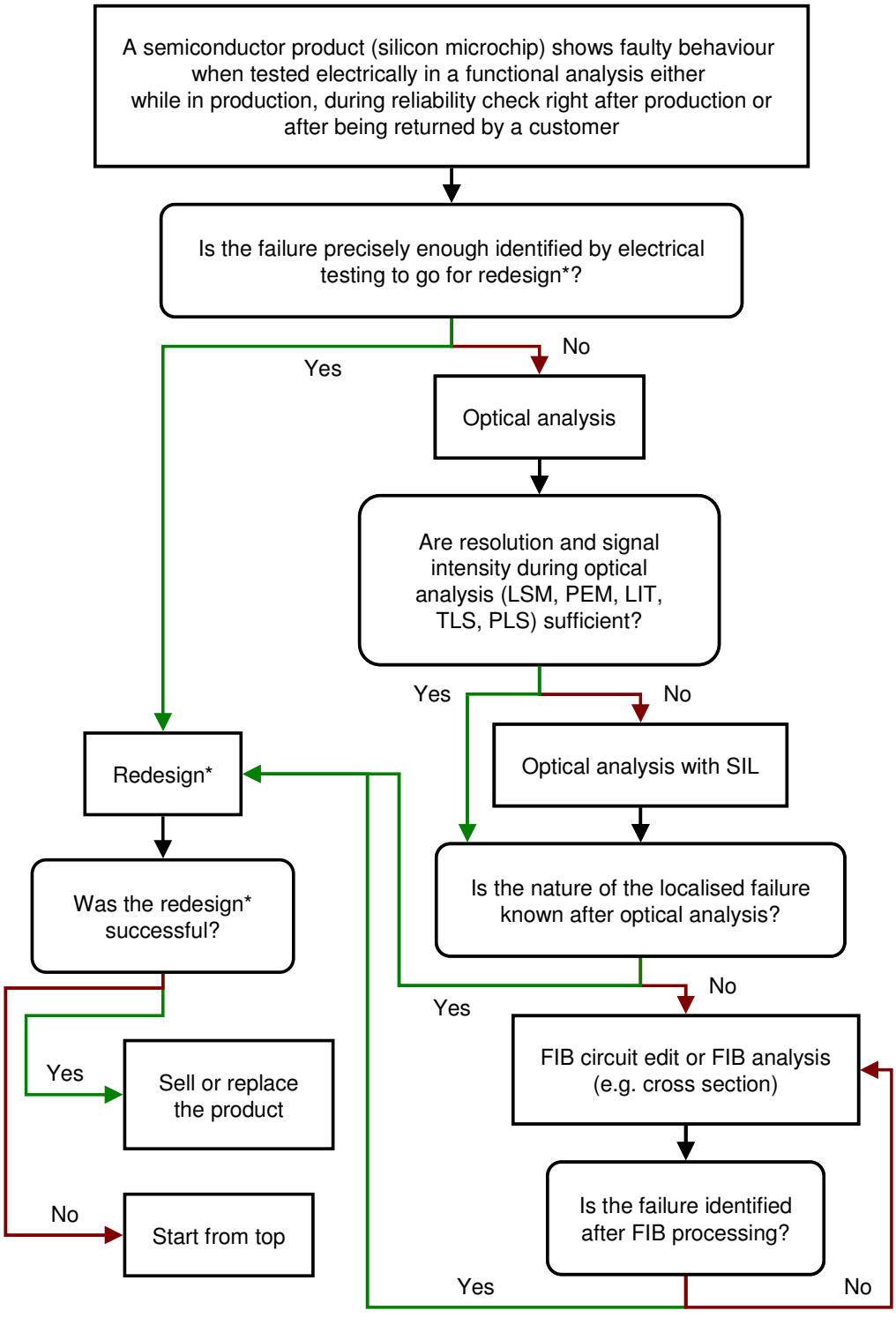

Fig. 4: Failure analysis flow demonstrating the possible application of a solid immersion lens (SIL). Redesign* means a new circuit design, new simulations and a new layout design to create the highly expensive new masks for the production process.

The methods mentioned in Fig. 4 as part of the optical analysis are laser scanning microscopy (LSM - see 2.8 and 2.9), photon emission microscopy (PEM) [6], lock-in thermography (LIT) [7], thermal laser stimulation (TLS) [8] and photoelectric laser stimulation (PLS) [9]. The *redesign** stands for a new circuit layout, new simulations and a new layout design, leading to the creation of highly expensive new masks with which a new version of the chip can be produced. If you notice the closed loop in the bottom right corner of Fig. 4, be aware that despite the fact of a FIB being a very powerful tool, this solution might not work in every case. To sum up the meaning of Fig. 4 for the purpose of this work, it can be said that optical analysis is a vital part of failure analysis and can be enhanced by using a solid immersion lens.

One condition for an optical analysis (and a physical analysis in general) is to have access to the chip. For already packaged chips this means removing or opening the package [10] (mentioned previously in Fig. 3). Two packaged microchips can be seen in Fig. 5, one of which is partially opened for backside analysis.

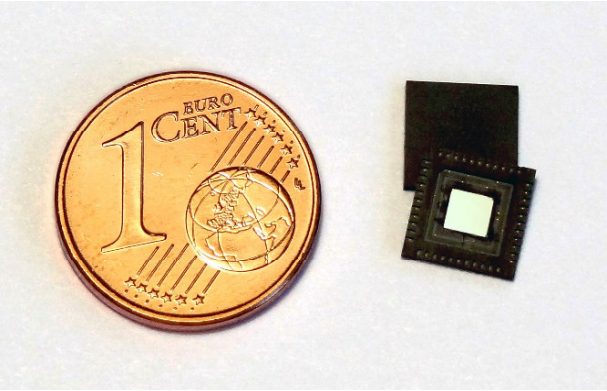

Fig. 5: Two packaged microchips. One is seen from the frontside (top) and the other from the backside (bottom). The package of the bottom chip is opened for backside analysis, exposing the polished silicon die.

Due to the previously mentioned increased number of metal layers and flip chip package designs it frequently becomes necessary to analyse a chip from the backside through the bulk silicon (Fig. 6).

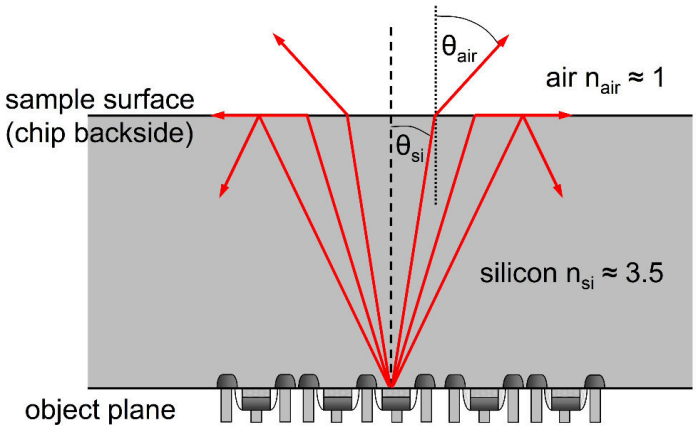

Fig. 6: Approaching a chip from the backside through the bulk silicon to analyze semiconductor devices in the object plane (silicon thickness and devices are not drawn to scale). Only a small part of the optical signal can be used due to refraction at the silicon-air-interface.

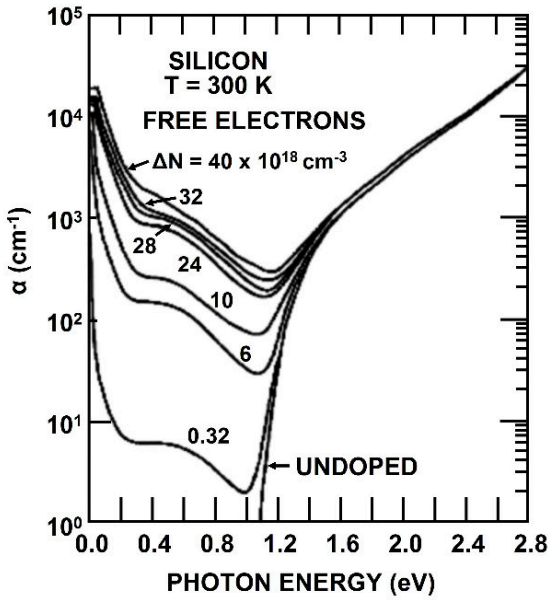

Fig. 7: Absorption spectra of crystalline silicon at various free electron densities, based on [11].

The bulk silicon material limits the part of the spectrum, which can be used for inspection. Silicon has a significantly reduced absorption for photons with energies below its band gap energy of about 1.12 eV or, respectively, a wavelength above 1100 nm (Fig. 7).

Therefore, optical imaging through silicon of considerable thickness relies on the spectral range of the infrared. Particularly the near infrared (NIR) with about 1 µm - 3 µm wavelength and 1.2 eV - 0.4 eV photon energy is commonly used. Since the wavelength directly relates to the resolution, the resolving power of an average 0.5 NA microscope at 1 µm wavelength is ultimately limited to roughly 1 µm (see chapter 2.5 for details on resolution), coming short of modern feature sizes by approximately one order of magnitude. A wise use of the absorbing silicon material can significantly improve the resolution using the shortened wavelength according to its index of refraction n. However, for subsurface imaging through a planar surface, this benefit is compensated by refraction at the silicon-air-interface as previously described in Fig. 6. This is the point at which a solid immersion lens (SIL) made of silicon can be beneficial. Fig. 8 illustrates the basic concept of a refractive SIL in a central or hemispheric set-up, with a distance between top of SIL and desired object plane equal to the radius of curvature of the SIL. This ideal set-up avoids refraction by letting the rays from the centre of the field of view pass from silicon to air at a perpendicular angle. Thereby a larger opening angle can be used inside the silicon, where the wavelength is shortened by the index of refraction n and the resolution is theoretically improved by the same factor. More details on SILs and also the difference between refractive and diffractive SILs (rSILs and dSILs) can be found in chapter 3.

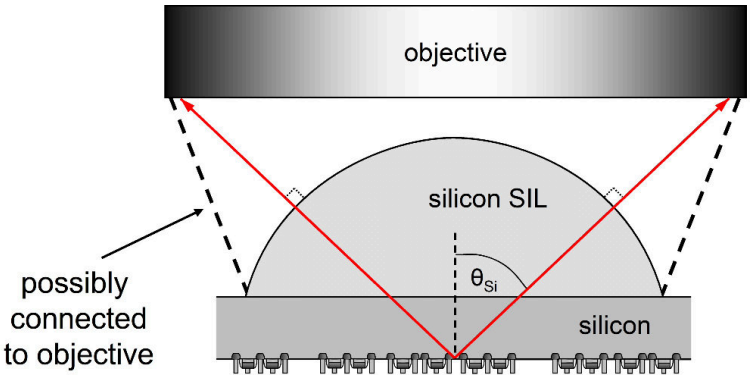

Fig. 8: Basic illustration of a refractive SIL used in a central set-up, with a distance between top of SIL and desired object plane equal to radius of curvature of the SIL. Depending on the SIL concept used, it might be physically connected to the microscope (see Fig. 9 for SIL concepts).

There are several ways in which a SIL can be used for imaging. Fig. 9 gives an overview. The SIL is attached to a microscope's objective in most commercial systems [12], [13], and some experimental ones [7], [14]. Other published works attach a SIL to a cantilever or a micromanipulator ([15] for rSILs, [16] for dSILs). A common solution in experimental rSIL work is to create the SIL from part of a silicon sphere and place it directly on the surface of the sample [17], [18]. The fourth SIL concept creates the lens shape directly out of the sample material itself ([19] for rSILs, [20] for dSILs). While the first three concepts externally place the SIL on the sample, the last concept can be considered to create the SIL internally and is also the scope of this work.

Several things have to be kept in mind when using external SILs (the first three types in Fig. 9) and are demonstrated with a SIL attached to an objective in Fig. 10. Generally an air gap between SIL and sample needs to be avoided, because it has a negative influence on resolution. The impact of the air gap on the imaging properties are discussed in detail in [5]. One condition for good SIL imaging is that the SIL is placed evenly on the sample, without tilt. Another one requires even polishing and a clean

surface. The last presented condition shows that external SILs can not be applied if the point of interest is too close to an obstacle, like the edge of the package opening. This might be the case, if the package can not be removed entirely and leaves only a small window (see sample in Fig. 5 for example).

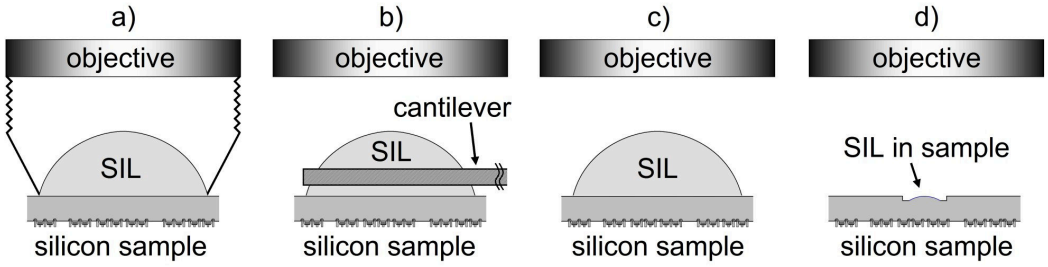

Fig. 9: Comparison of different SIL concepts: a) attached to a microscope's objective, b) attached to a cantilever or micromanipulator, c) freely placed on the surface, d) created out of the sample material. a), b), c) can be called external, while d) is internal.

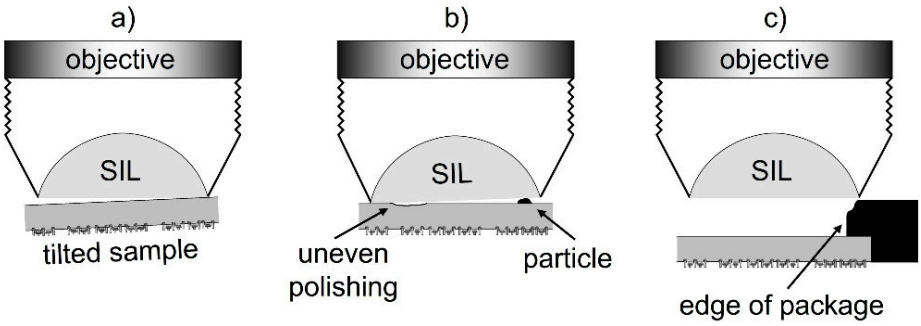

Fig. 10: Conditions that need to be kept in mind when using external SILs: a) SIL needs to be placed evenly on the sample without tilt, b) the sample needs to be well polished and clean, c) external SIL can not be applied, if area of interest is close to the edge of the package opening (see Fig. 5 for an opened package).

In practice, condition a) of Fig. 10 does not occur for SILs freely placed on the surface or made out of the sample material (last two SILs in Fig. 9). Condition b) is a problem which applies to all external SILs and so is c). Tapering the bottom of an rSIL [7] instead of using a flat one reduces part of these problems, but doesn't solve them entirely and might also reduce

the opening angle. The necessity of having physical contact with the sample in a possibly restricted space remains for all external SILs. Since the internal SIL can be created directly out of the sample material, an air gap never occurs. With the right design it is furthermore possible to create a SIL out of sample material, which is large enough to provide optical benefits, but also small enough to allow for a creation in crucial spots. That is the reason why this work deals with the creation of SILs directly out of the silicon material of a microchip using a focused ion beam machine. Two concepts are applied: a spherical refractive SIL (rSIL, chapter 3.2) and a binary diffractive SIL (dSIL, chapter 3.3), as illustrated in Fig. 11.

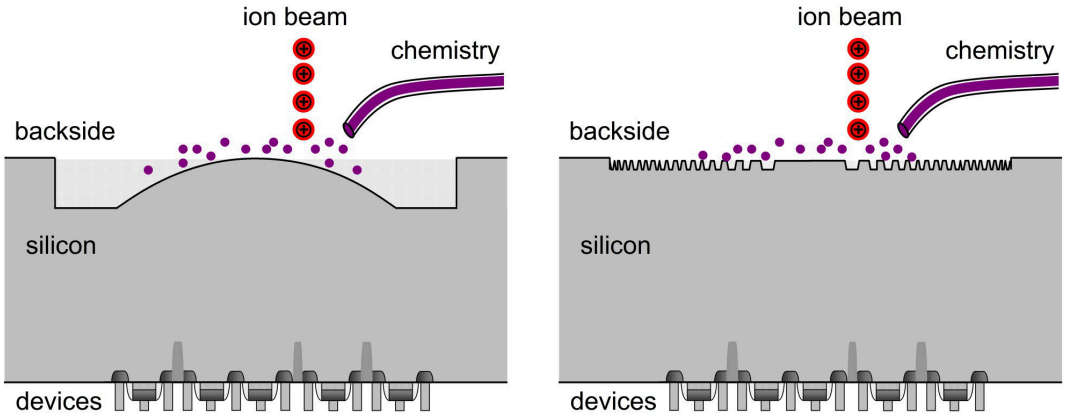

Fig. 11: Solid immersion lens (SIL) concepts realized in this work: left refractive SIL (rSIL) and right diffractive SIL (dSIL), see chapter 3.

Previous published works have created an rSIL shape out of sample material with a computer numerical controlled lathe [19], which permanently altered the sample and was not pursued further. A more popular method for experimentally creating dSILs out of sample material involves combining FIB patterning and reactive ion etching [14], [20]. However, to the author's knowledge, there are no previous works which develop and demonstrate SILs created out of the backside of a silicon sample in a single FIB process.

This work lists an excerpt of the experiments carried out during the development of FIB created rSIL and dSIL techniques. Theoretical basics are explained and process details are illustrated. The experimental results prove that the presented techniques work well and this document includes the needed information to further develop them to their full potential.

2 Optical theory

The common purpose of an optical device is to collect and reshape part of an incident wavefront, usually to form an image of an object. Due to physical limitations, an optical system can generally only accept a segment of the wavefront. Therefore the initial propagation of the wave is restricted and influenced by diffraction. The created image is blurred to some extend (see Airy pattern in 2.5). It follows that a real optical imaging system is diffraction-limited. It can be called so, if the resolution of the system is not limited by imperfections of the lens(es), but merely by diffraction. This chapter discusses and calculates the effects of an aperture and a lens in the path of light, leading to definitions of resolution and the design of a confocal laser scanning microscope.

2.1 Basic imaging through an aperture

When describing light as a simplified plane wave travelling along the x-axis, it can be presented as

$$A(x,t) = A_0 \cos(\omega t - kx + \varepsilon). \quad (1)$$

Complex numbers can be used to avoid trigonometric functions, leading to

$$U(x,t) = A_0 e^{j(\omega t - kx + \varepsilon)}. \quad (2)$$

In either case, it consists of amplitude A_0, angular frequency ω, time t, wavenumber $k = 2\pi/\lambda$ with wavelength λ, position x and initial phase ε.

The latter can be put into an individual phase factor $e^{j\varepsilon}$ and included in the complex amplitude U_0 being $U_0 = A_0\, e^{j\varepsilon}$. This yields

$$U(x,t) = U_0\, e^{j(\omega t - kx)} \tag{3}$$

with Re [U(x,t)] = A(x,t).

In the upcoming sections the amplitude of this wave is used to calculate the effect of diffraction while light travels through an aperture or lens, illuminating a following screen. Finally the intensity of the wave and its pattern is determined from the squared amplitude to discuss various definitions of resolution. The equations and the train of thought are mostly based on [21].

The set-up of Fig. 12 is to be considered. Light hits an aperture in the plane of x_1 and y_1 and travels the distance z to a screen in the plane of x_2 and y_2. It is assumed, that the aperture is evenly illuminated.

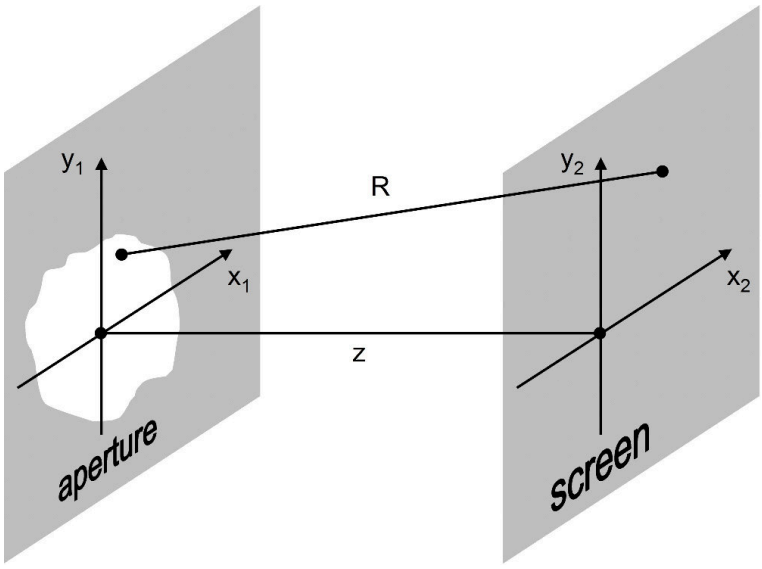

Fig. 12: Basic set-up of a screen illuminated from the left through an arbitrary aperture.

Kirchhoff's diffraction formula (4) is used to begin the calculations. It puts Huygens' principle into a mathematical equation [22]. Huygens stated that

every part of a wavefront U_1 can be considered to create a spherical wave proportional to U_1. The moving wave is then the sum of these spherical waves [22]. This is expressed mathematically by the double integral, which sums all elements of the waves e^{-jkR}/R. The amplitude on the screen can thereby be derived from the distribution at the aperture.

$$U_2(x_2,y_2) = \int_{-\infty}^{+\infty}\int \frac{1}{j\lambda R} U_1(x_1,y_1) e^{-jkR} dx_1 dy_1 \tag{4}$$

U_1 and U_2 are expected to be close to the optical axis in relation to the axial distance z. Following this expectation with maximum values of x_1, y_1 & x_2, $y_2 << z$ offers the ability to replace R by z in the denominator and approximate R in the exponent as the square root of x^2,y^2,z^2-components. This is done by using the binomial theorem or Heron's method as a specific application of Newton's method. The result is the *Fresnel approximation*

$$U_2(x_2,y_2) = \frac{e^{-jkz}}{j\lambda z} \int_{-\infty}^{+\infty}\int U_1(x_1,y_1)\, e^{-\frac{jk}{2z}((x_2-x_1)^2+(y_2-y_1)^2)} dx_1 dy_1 . \tag{5}$$

The Fresnel approximation of the Kirchhoff diffraction formula can be used, if z is significantly larger than the maximum x- and y-values. If the maxima of x_1 and y_1 relate to z even more so, that

$$z >> \frac{1}{2} k(x_1^{\,2} + y_1^{\,2})_{max} \tag{6}$$

(see part of exponent), then the $x_1^{\,2}$ and $y_1^{\,2}$ terms can be neglected. This creates the *Fraunhofer approximation* (7)

$$U_2(x_2,y_2) = \frac{e^{-jkz}}{j\lambda z} e^{-\frac{jk}{2z}(x_2^2+y_2^2)} \int_{-\infty}^{+\infty}\int U_1(x_1,y_1) e^{\frac{jk}{z}(x_1x_2+y_1y_2)} dx_1 dy_1 . \quad (7)$$

The *Fresnel number* N_F can be defined based on (6) using $k = 2\pi/\lambda$ and dividing by z.

$$N_F = \frac{\pi}{\lambda z}(x_1^2 + y_1^2)_{max} \quad (8)$$

or for a circular aperture with radius r

$$N_F = \frac{\pi r^2}{\lambda z} . \quad (9)$$

The general rule to distinguish between near-field and far-field, and respectively Fresnel and Fraunhofer diffraction, is that the latter is expected if $N_F << 1$. This corresponds to a set-up where the screen is, compared to the area of the aperture, far away from the aperture. More discussions on the Fresnel number will follow in chapter 2.10.

In the next step, the two-dimensional Fourier transform $\tilde{U}(m,n)$ of $U(x,y)$ can be applied. Its main advantage, being the fundamentals of Fourier optics, is the fact that an aperture or lens creates a Fourier transform of the wave pattern from an object. The Fourier transform of the aperture or lens function can therefore be used to calculate the diffraction pattern. Wilson [21] defines the Fourier transform as

$$\tilde{U}(m,n) = \int_{-\infty}^{+\infty}\int U(x,y) e^{2\pi j(mx+ny)} dxdy \quad (10)$$

and the inverse Fourier transform as

$$U(x,y) = \int_{-\infty}^{+\infty}\int \tilde{U}(m,n)\, e^{-2\pi j(mx+ny)} dmdn\,. \qquad (11)$$

Based on (10) with $m = x_2/\lambda z$ and $n = y_2/\lambda z$, expression (7) turns into

$$U_2(x_2,y_2) = \frac{e^{-jkz}}{j\lambda z} e^{-\frac{jk}{2z}(x_2^2+y_2^2)} \tilde{U}_1(x_2/\lambda z, y_2/\lambda z)\,. \qquad (12)$$

This illustrates how the illumination on a screen, which is the distance z away from an aperture, can be defined by the Fourier transform of the field at the aperture. While making this statement, it should to be noticed that it is not entirely valid for every value of numerical aperture (NA). The presented calculations use scalar theory and can be applied to systems of low to moderate NA. For high-NA systems, the vectorial nature of light needs to be taken into account, to describe the electromagnetic field properly. More details can be found e.g. in chapter 3 of [23].

2.2 Imaging through a circular aperture

A common application of (12) is presented in the kind of a circular aperture with radius a and illustrated in Fig. 13.

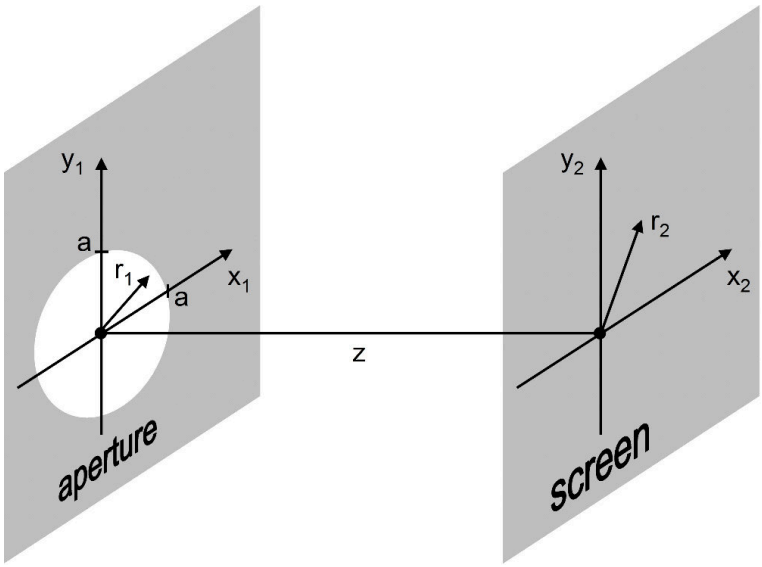

Fig. 13: Set-up of a screen illuminated from the left through a circular aperture.

The circular aperture is expected to be evenly illuminated and can be described by the circ function written in terms of circ(r_1/a), with $r_1/a = r$ and defined as

$$\mathrm{circ}(r) = \begin{matrix} 1 & ,r<1 \\ 0 & ,r>1 \end{matrix}. \tag{13}$$

The field amplitude adapted for this set-up based on (12) is

$$U_2(r_2) = \frac{e^{-jkz}}{j\lambda z} e^{-\frac{jkr_2^2}{2z}} \tilde{U}_1(ar_2/\lambda z). \tag{14}$$

where $\tilde{U}_1(ar_2/\lambda z)$ can be calculated using a Fourier-Bessel (or Hankel) transform with zeroth- and first-order Bessel functions of the first kind (J_0 and J_1)

$$\tilde{U}(\rho) = \int_0^{+\infty} 2\pi r\, U(r)\, J_0(2\pi\rho r)dr. \tag{15}$$

Further utilising

$$\int_0^1 2\pi r\, J_0(2\pi\rho r)dr = (1)^2 \frac{J_1(2\pi\rho)}{\rho} = \pi(1)^2 \frac{2J_1(2\pi\rho)}{2\pi\rho} \tag{16}$$

with $\rho = ar_2/\lambda z$ and r going from 0 to a instead of 0 to 1 leads to the diffracted amplitude

$$U_2(r_2) = \frac{e^{-jkz}}{j\lambda z} e^{-\frac{jkr_2^2}{2z}} \pi a^2 \frac{2J_1(2\pi a r_2 / \lambda z)}{2\pi a r_2 / \lambda z}. \tag{17}$$

2.3 Basic imaging through a thin lens

The previous two sections led to the far-field diffraction pattern on a screen well behind an aperture which was hit by a plane wave. Now this aperture is filled with a focusing lens. This enables the screen to be placed closer to aperture and lens, in the focal plane of the lens at z = f, without changing the diffracted pattern. The set-up is comparable to that in Fig. 12 with an additional (arbitrarily shaped) lens. The lens is to be a thin lens with the characteristic that rays passing through it do not experience a lateral offset. The general equation (12) shows that if the lens should create the same pattern as the aperture alone, the change of phase introduced by the lens must be such as to multiply the amplitude by

$$t(x,y) = e^{\frac{jk}{2f}(x^2+y^2)}, \tag{18}$$

see [21]. A thin lens made of dielectric material with two spherical surfaces has been shown to create this phase change [24]. The physical properties of the lens, such as size, absorption and reflection, are considered by the pupil function of the lens P(x,y), which is not being dealt with in detail at this point.

Illumination by a plane wave leads to the following amplitude right behind the lens

$$U_1(x_1, y_1) = P(x_1, y_1)\, e^{\frac{jk}{2f}(x_1^2 + y_1^2)} \quad . \tag{19}$$

The term (19) represents a spherically shaped wave converging on a point at the distance f behind the lens.

The Fresnel approximation (5) is used to calculate the general diffracted amplitude at a distance z behind the lens. The corresponding term is

$$U_2(x_2, y_2) = \frac{e^{-jkz}}{j\lambda z} \int_{-\infty}^{+\infty}\int P(x_1, y_1)\, e^{\frac{jk}{2f}(x_1^2 + y_1^2)} e^{-\frac{jk}{2z}[(x_2 - x_1)^2 + (y_2 - y_1)^2]} dx_1 dy_1 . \tag{20}$$

The x_1^2 and y_1^2 terms from the second and third exponent cancel each other, once z is set to be equal to f (diffracted amplitude on the screen). This leads to

$$U_2(x_2, y_2) = \frac{e^{-jkz}}{j\lambda z} e^{-\frac{jk}{2f}(x_2^2 + y_2^2)} \int_{-\infty}^{+\infty}\int P(x_1, y_1)\, e^{\frac{jk}{f}(x_1 x_2 + y_1 y_2)} dx_1 dy_1 . \tag{21}$$

2.4 Imaging through a radially symmetric lens

The term (21) of the diffracted amplitude can be adapted to fit a radially symmetric lens, which enables the (partial) mathematical description of a set-up equal to an eye, camera lens, telescope, or microscope [25]. It results in a set-up similar to that of Fig. 13, but with a radially symmetric lens. The integral of (21) is the Fourier transform of the pupil function, comparable to the aperture in equations (7) and then (12). Applying the geometry of the radially symmetric lens also leads to the Fourier-Bessel transform, just like the radial aperture in (15), and to

$$U_2(r_2) = \frac{e^{-jkf}}{j\lambda f} e^{-\frac{jkr_2^2}{2f}} \int_0^{+\infty} 2\pi r_1 \, P(r_1) J_0\left(\frac{2\pi r_1 r_2}{\lambda f}\right) dr_1 . \tag{22}$$

With a circular lens of radius a, the just defined amplitude (22) becomes similar to that of the circular aperture in (17), but with an image at the distance of the focal length f.

$$U_2(r_2) = \frac{e^{-jkf}}{j\lambda f} e^{-\frac{jkr_2^2}{2f}} \pi a^2 \frac{2J_1(2\pi a r_2 / \lambda f)}{2\pi a r_2 / \lambda f} \tag{23}$$

[21] introduces a normalised optical coordinate v (not connected to velocity in any way) including the numerical aperture of the lens (NA = n sinθ) in air with $n_{air} \approx 1$. It is furthermore assumed that the distance between lens and screen is large compared to the radius of the lens ($\sin\theta = a / R \approx a / f$).

$$v = kr_2 NA = kr_2 \sin\theta = \frac{2\pi}{\lambda} r_2 \sin\theta = \frac{2\pi a r_2}{\lambda f} \tag{24}$$

With this, the equation (23) can be written as

$$U_2(v) = -jN_F e^{-jkf} e^{-\frac{jv^2}{4N_F}} \frac{2J_1(v)}{v}, \tag{25}$$

where N_F is again the Fresnel number in terms of

$$N_F = \frac{\pi a^2}{\lambda z} . \tag{26}$$

The intensity on the screen at a distance f to the lens can be calculated from (25) as the magnitude (or absolute value, or modulus) of the amplitude squared:

$$I_2(v) = N_F^2 \frac{4J_1^2(v)}{v^2} \tag{27}$$

Fig. 14 shows a corresponding plot, normalised to 1. This pattern of the intensity on a screen is commonly referred to as the point spread function (PSF), which is the response of the described optical system to a point source.

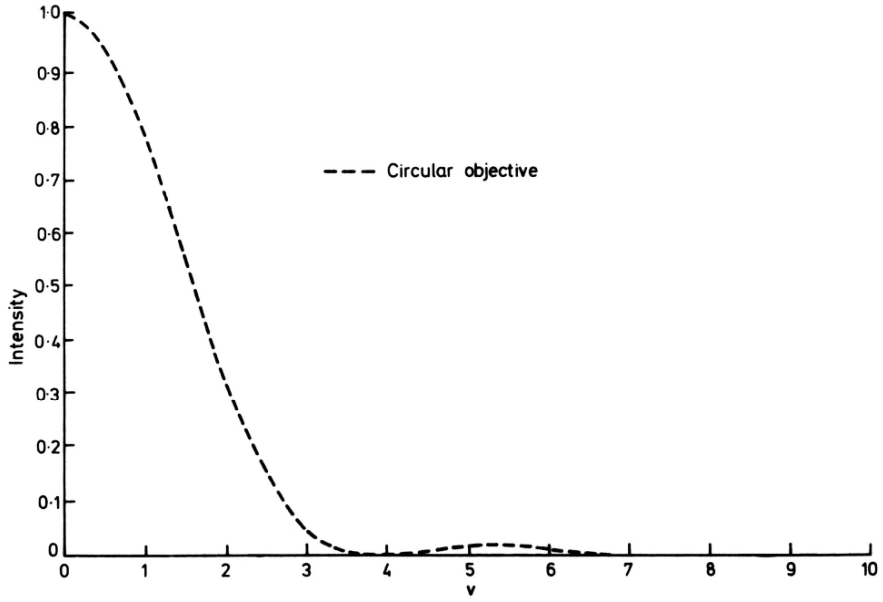

Fig. 14: Pattern of the normalised intensity focused on a screen through a radially symmetric lens. See equation (24) for the optical coordinate v. Image was modified from [21] by showing only the circular objective.

Hecht [25] points out, that the current term for “intensity” is “irradiance”. Since most of chapters 2.1 through 2.7 are based on Wilson and Sheppard [21], the author sticks to their terminology and uses “intensity”, while noting that it may not be up-to-date.

2.5 Airy disk and spatial resolution

Plotting the intensity values calculated in (27) and illustrated in Fig. 14 on the x-y-plane brings out the 3D sketch of Fig. 15 and the greyscales of Fig. 16. For these two plots, equation (27) was applied to the base matrix described in chapter 4.4 and the Appendix. The value of every element of the base matrix is its distance to the centre and can therefore also be defined by the optical coordinate v from (24).

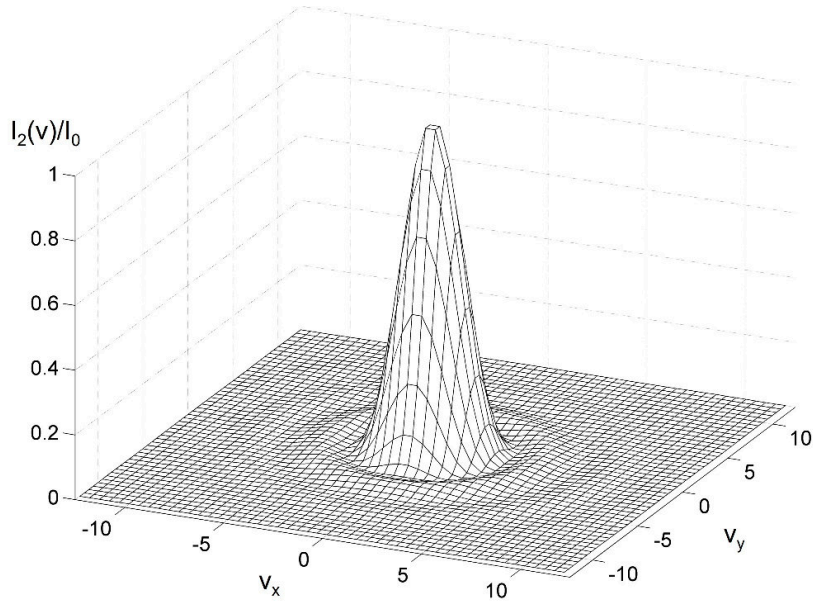

Fig. 15: Three-dimensional intensity distribution illustrating equation (27) and thereby the Airy pattern. The horizontal plane resembles the screen and the vertical height the intensity values.

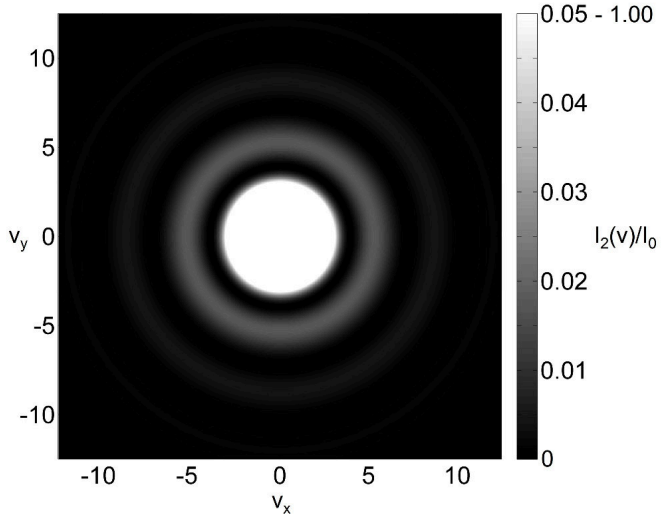

Fig. 16: Intensity distribution based on equation (27) leading to the Airy pattern with the Airy disk in its centre. The illustration only distinguishes between the first 5% of the intensity values from Fig. 15 to improve the visibility of the outer rings.

The inner bright spot shown in Fig. 16 is called the Airy disk, named after George Biddell Airy [26]. On the surrounding dark ring, the $J_1(v)$ Bessel function first reaches zero. This happens when the optical coordinate v has a value of 3.83. Using this condition with the definition of v in (24) and solving for r_2 gives the radius of the Airy disk

$$r_{Airy} = r_2(v = 3.83) = \frac{3.83}{\pi}\frac{f\,\lambda}{2a} = 1.22\frac{f\,\lambda}{2a}. \tag{28}$$

Lord Rayleigh and C. H. Sparrow used two overlapping Airy patterns to define their resolution criteria. Resolution is commonly described as the minimum resolvable distance that two objects need to be apart in order to be distinguishable in an image. Lord Rayleigh defined two ideal point sources to be resolved, if the peak of one Bessel function falls onto the first zero of the other [27] (Fig. 17), which is equal to the previously mentioned radius of the Airy disk. For the presented set-up this can be expressed as

$$Res_{Rayleigh} = 1.22\frac{f\lambda}{2a} = \frac{0.61\lambda}{\sin\theta}. \quad (29)$$

2a is the diameter of the lens. a / f = sinθ is the numerical aperture in air ($n_{air} \approx 1$) with the opening angle against the optical axis θ and the assumption that the distance between lens and screen is much larger than the radius of the lens. In SIL imaging (see chapter 3) the index of refraction differs from 1, therefore a more general description of the Rayleigh criterion using the numerical aperture NA is useful:

$$Res_{Rayleigh} = \frac{0.61\lambda}{n\sin\theta} = \frac{0.61\lambda}{NA} \quad (30)$$

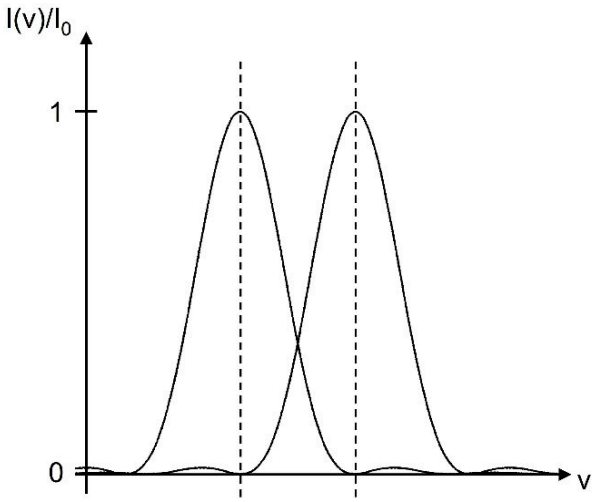

Fig. 17: Illustration of the Rayleigh criterion, which declares two point sources (vertical dashed lines) to be resolved in an image, if the maximum intensity of one source meets the first zero value of the next. For coordinate v see (24).

C. M. Sparrow chose a more appropriate definition (according to [25]) by naming the two point sources resolved, if the sum of their intensity profiles becomes flat [28] (Fig. 18). Mathematically speaking, this is the case when the second derivative just turns zero as the sources come closer. The

resolvable distance between two point sources in terms of λ and NA is therefore

$$\mathrm{Res}_{\mathrm{Sparrow}} = \frac{0.51\lambda}{\mathrm{NA}}. \tag{31}$$

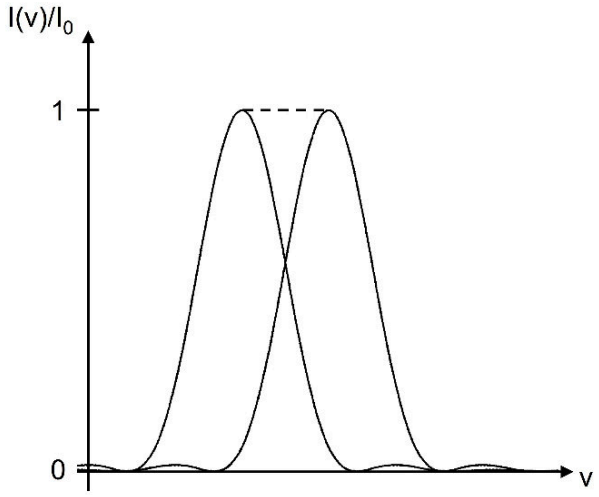

Fig. 18: Illustration of the Sparrow criterion. With this, two point sources are defined as resolved in an image, if the sum of their intensities (dashed line, also normalised to 1) is flat. For coordinate v see (24).

Another definition based on the intensity profiles is the Houston criterion or full width at half maximum (FWHM) [29] (Fig. 19). It states that two points are resolved, if the distance between their centres is equal to the full width of their intensity profile at half its maximum value. In other words, their profiles have to meet at half maximum. The resolution can be calculated similar to the radius of the Airy disk in (28) by taking the radial value from the intensity distribution or point spread function (Fig. 14) at half its maximum (0.5 at v = 1.61). Twice this value of v (2 · 1.61) is the distance between the two points. Solving for r_2 leads to

$$Res_{Houston} = \frac{0.51\lambda}{NA}. \tag{32}$$

This result shows that the Sparrow criterion is consistent with the FWHM of the point spread function for plane wave illumination.

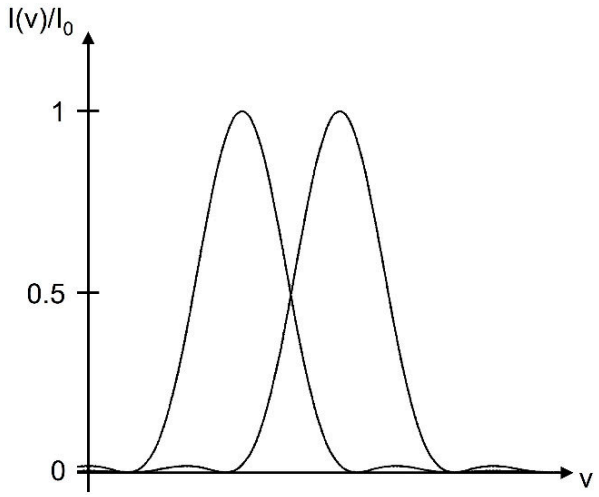

Fig. 19: Illustration of the Houston criterion of full width at half maximum (FWHM). In this case the resolution is determined by the width of the intensity pattern of one ideal point source at half its maximum value. The two points are therefore resolved if their intensity curves meet at half maximum. For coordinate v see (24).

The Houston criterion is popular for its mathematical simplicity, the Sparrow criterion is often applied especially for astronomical studies and the Rayleigh criterion is found to be a common standard (though not necessarily the most accurate one). Apart from the previously shown theoretical consistency between the definitions from Sparrow and Houston, it was also demonstrated experimentally that the Houston criterion applied to a Gaussian function closely matches the Sparrow criterion (see [14] p. 30). A detailed comparison of the criterions for various profile functions can be found in [30].

2.6 The Gaussian beam

It was shown in chapter 2.4 how the field amplitude at a lens connects to that on a following screen, leading to the Airy pattern (Fig. 16) on page 33. It were practical if the incoming waves could be described by a function which maintains its general shape even after traversing the lens. The Gaussian function is such a case. Furthermore it is not only practical, but evident that for most lasers, the emission corresponds to a Gaussian beam, which is characterized by a Gaussian beam profile (Fig. 20). The distribution of the intensity in the beam profile can be described by

$$I(r) = I_0 e^{\frac{-2r^2}{w^2(z)}}. \tag{33}$$

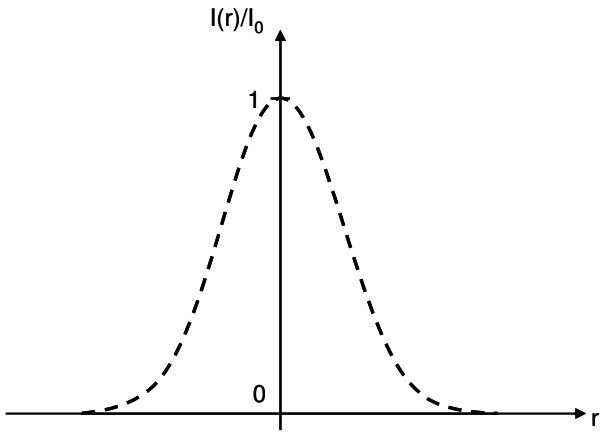

Fig. 20: Intensity distribution of a Gaussian beam.

Comparing the intensity pattern behind an aperture, created by a plane wave and created by a Gaussian beam, shows close resemblance especially in the central part of the Airy pattern, namely within the Airy disk. A detailed comparison can be seen in Fig. 21 and is calculated in [31].

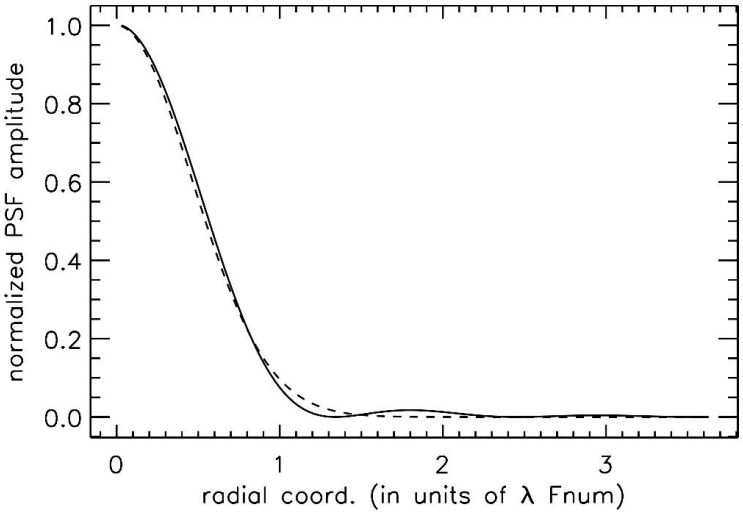

Fig. 21: Comparison of an Airy pattern and a Gaussian beam [32].

The smallest spot, onto which a laser or Gaussian beam can be focused, is twice the beam waist w_0. The general half-width of the beam in relation to the distance z is

$$w(z) = w_0 \sqrt{1 + \frac{z}{z_R}} \tag{34}$$

with the Rayleigh range

$$z_R = \frac{\pi w_0^{\,2}}{\lambda}. \tag{35}$$

At $z = z_R$ the half-width of the beam is $\sqrt{2}\, w_0$. Therefore the area of the cross section doubles at this point, which indicates why the Rayleigh range is a convenient measure for the divergence of the beam. The total angular spread or full-angular width is determined by θ. All the mentioned parameters are illustrated in Fig. 22 along with beam profiles before and after the focal point. Note that θ describes a full angle only for the Gaussian beam. For all other applications in this work, it is the angle with respect to the optical axis.

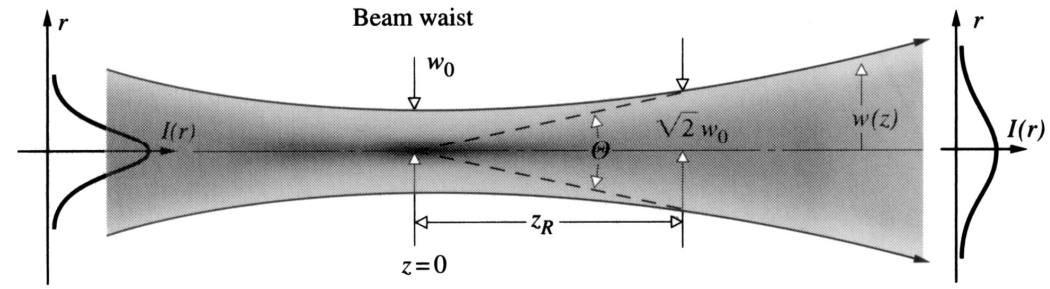

Fig. 22: Parameters of a Gaussian beam illustrating its half-width w(z) and the intensity profile I(r) as the beam progresses along the x-axis [25].

The fact that light, even in the form of a laser, cannot be focused down to an infinitely small spot governs the limit of resolution. The upcoming chapter 2.7 presents a way to further reduce this spot size by adding a stop in the centre of the aperture. The following set-up of a confocal laser scanning microscope in chapter 2.8 and 2.9 shows how modifying the spot size not only on the object, but also on the detector can optimize the imaging capabilities of a microscope. Finally, chapter 2.10 concludes the topic of “Optical theory” by pointing out conditions under which analysis and calculation can be simplified by the means of geometrical optics.

2.7 Imaging through an annular aperture and lens

A promising modification of the circular aperture and lens is the annular set-up having a circular stop in the centre (see Fig. 23). The idea was applied to refractive SILs placed on a sample [17], [18] and also considered for the FIB created rSILs presented in this work. However, it could not yet be realized by the author. One limiting factor of the annular set-up is the loss in intensity, which can be compensated by laser illumination. Another one is the needed large opening angle maintaining enough open lens area around the stop. The latter was not yet achieved by the FIB created rSILs of this work. The theoretical background should

be presented at this point nonetheless for reference and future developments.

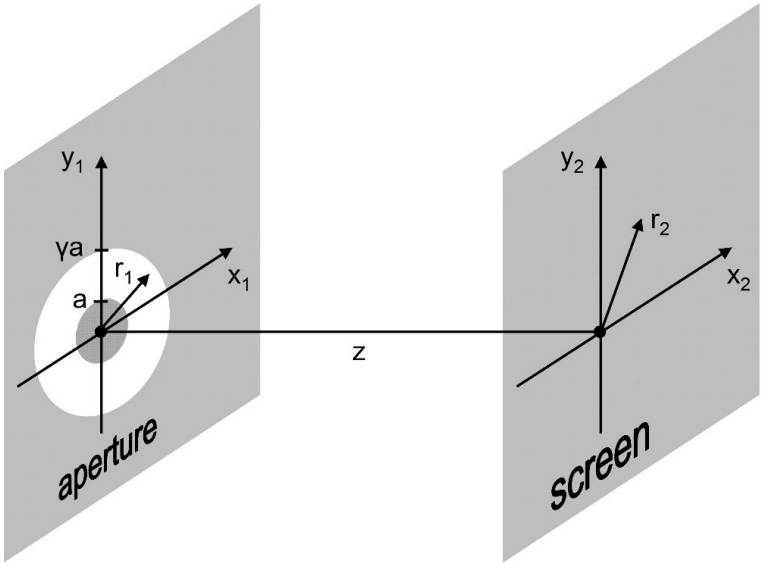

Fig. 23: Set-up of a screen illuminated from the left through an annular aperture.

The diffracted amplitude of the annular aperture can be calculated similar to that of a circular one. For details see [21]. With an inner radius a and an outer radius γa (see Fig. 23) it is

$$U_2(r_2) = \frac{e^{-jkz}}{j\lambda z} e^{-\frac{jkr_2^2}{2z}} 2\pi(a - \gamma a) J_0(2\pi a r_2 / \lambda z). \tag{36}$$

Placing a lens in the annular aperture leads to an amplitude in the focal plane of

$$U_2(v) = -2jN_F\left(\frac{a - \gamma a}{a}\right) e^{-jkf} e^{-\frac{jv^2}{4N_F}} J_0(v). \tag{37}$$

For v see 24 and for N_F see 26. The resulting intensity is

$$I_2(v) = 4N_F^2\left(\frac{a - \gamma a}{a}\right)^2 J_0^2(v)\,. \qquad (38)$$

Its profile is plotted, also normalised to 1, in Fig. 24 in direct comparison to the intensity of a circular lens without stop (previously shown in Fig. 14). A narrower central spot can be observed, but also stronger outer rings.

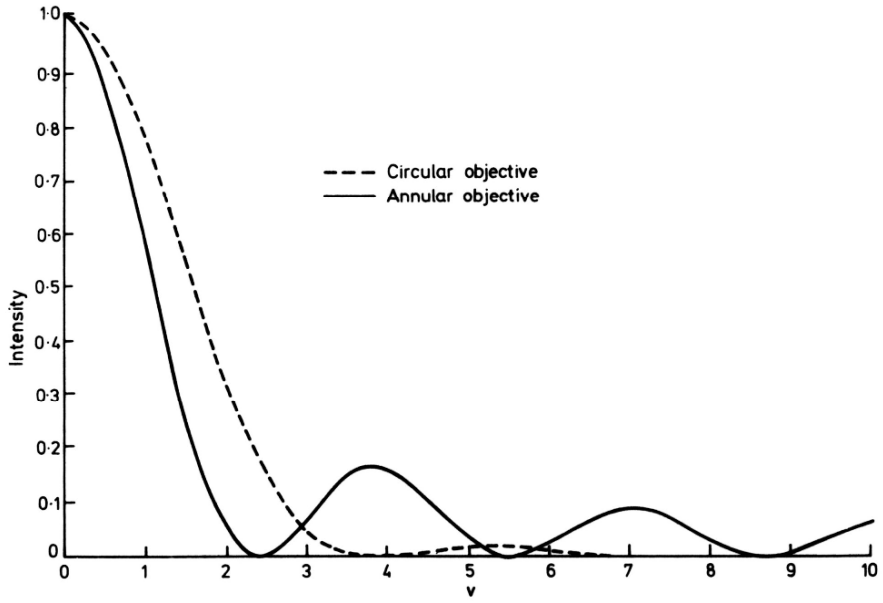

Fig. 24: Comparison of the intensity pattern created by a circular lens and by an additional annular stop. Image was modified from [21] by adjusting the legend.

Wilson and Sheppard [21] applied the annular set-up to a confocal microscope and compared it to a regular confocal microscope as well as to a conventional microscope (Fig. 25). The annular set-up again achieves the smallest spot size at the cost of stronger side lobes and a loss in absolute intensity.

More details on the set-up of a confocal scanning microscope can be found in [21] and will follow in chapter 2.8.

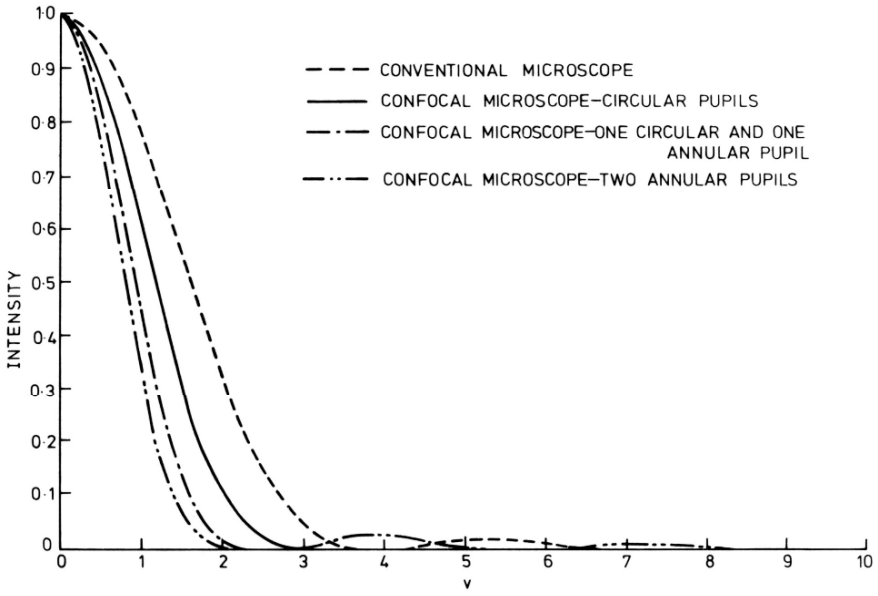

Fig. 25: Different set-ups for a microscope in comparison. Image source is [21].

2.8 The confocal laser scanning microscope

Fig. 26 illustrates a set-up of a confocal laser scanning microscope. Starting from the source, a laser is used for coherent illumination. The collimator turns the laser light from being close to a point source into a plane wave, which is reflected off a dichromatic mirror or beam splitter. From that point on, the illuminating light and the detected signal have the same path. The laser light is continuously deflected by scanning mirrors and then focused through the objective onto the focal plane. This leads to a single scanning spot. The thereby excited sample reflects (or emits) light. The objective collects a certain part of it, depending on its numerical aperture. The reflected light is then deflected by the scanning mirrors in the same way the illumination was. It continues on a separate path after passing the beam splitter and is focussed onto the confocal pinhole. The confocal pinhole can be considered a key feature of the confocal laser scanning microscope. Emission collected from outside the objective's focal

plane is blocked by this aperture. Thereby only the desired signal reaches the detector (e.g. a photodiode) and contributes to the final image. The laser is focused to a diffraction-limited spot in the focal plane, which itself is focused onto the pinhole, and creates the confocal beam path.

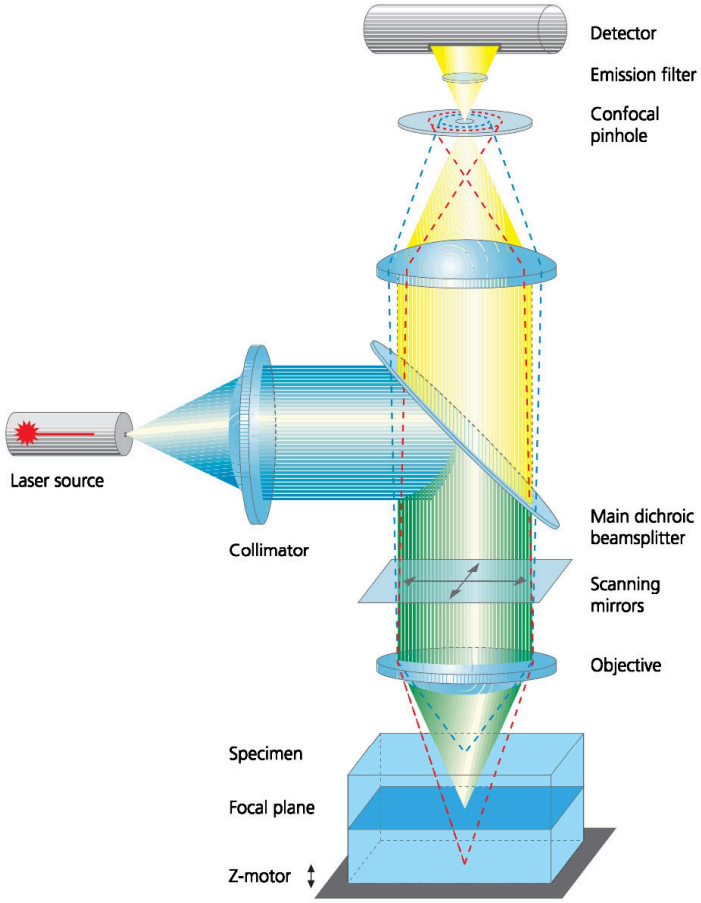

Fig. 26: Set-up of a confocal laser scanning microscope from [33].

The part, which is not included in Fig. 26, but in fact creates the final image, is the computer hardware. Two signals are mainly used: On the one hand the x- and y-coordinates gathered from the scanning mirrors and on the other hand the intensity signal from the detector. Both are combined to form the final image in a pixel matrix. This makes it quite clear, why a laser scanning microscope can only create a digital image

and not a directly observable one, like that from a conventional microscope. The significant improvement in image quality, of a confocal microscope compared to a conventional widefield one, leads to the statement that “confocal technology is proving to be one of the most important advances ever achieved in optical microscopy” [34]. For further introduction to and overview of confocal scanning microscopy see [33] or [34]. For in depth theory see [21].

2.9 Hardware used: Phemos 1000

The confocal laser scanning microscope used in this work is a Phemos 1000 from Hamamatsu Photonics (Fig. 27). The precise description is infrared confocal emission microscope with laser stimulation option. The functionality most valuable to the author for the presented work is the ability to create reflective images through the bulk silicon material of a microchip’s backside. Two infrared lasers with 1064 nm and 1300 nm wavelength are available for illumination. They can also be used for laser stimulation. The first with a mostly photoelectric effect [9] where the photons have enough energy to create electron-hole pairs, and the second with a mostly thermal effect [8] where the photons have less energy and excite the sample only thermally. Furthermore the cooled CCD camera C4880 can be used for photon emission analysis [6] as done in chapter 5.1.6. For more technical details see [35].

Fig. 27: Infrared confocal emission microscope Phemos 1000 from Hamamatsu Photonics.

The Phemos 1000 in the lab of “Semiconductor Devices” at Technische Universität Berlin (TUB) offers five objectives: 0.8x with 0.4 NA, 5x with 0.14 NA, 20x with 0.4 NA, 50x with 0.7 NA and 100x with 0.5 NA. Except for the 0.8x macro lens, they can all be seen along with the microscope apparatus and the cooled CCD camera C4880 in Fig. 28.

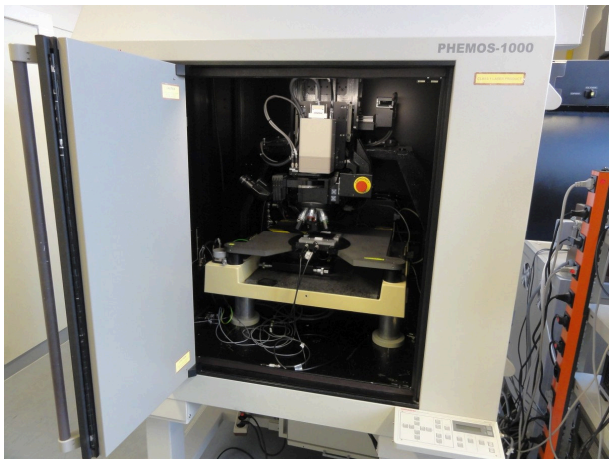

Fig. 28: Inside of the Phemos 1000 with microscope objectives and cooled CCD camera.

From the available objectives the 50x or 100x were used with the FIB created SILs in this work. Laser scanning images of a resolution test pattern (Fig. 29) taken with these objectives by the 1064 nm and 1300 nm

laser are presented next, to give an impression of imaging from the front and backside of a chip without SIL. The thickness of the bulk silicon is about 70 µm in Fig. 29 to Fig. 33. The test pattern is part of an “Azuma Optical Probe Test Chip” supplied to the author by DCG Systems. It consists of floating metal structures on the first of the overall six metal layers. Each pattern is made up by several elements with their corresponding element numbers on the side. One element is a set of horizontal and vertical lines. The elements are collected in groups with their corresponding group numbers above. The pattern is based on the USAF 1951 bar target. The line width in mm can be calculated by

$$\text{line width in mm} = 2^{\frac{\text{element \#}}{6} - \text{group \#}}. \tag{39}$$

Multiplying the calculated line width by 2000 gives the pitch size in µm. The pitch size is defined to be the line width plus the spacing, which is equal to twice the line width for this bar target.

A certain amount of experiments in this work are demonstrated on these patterns. They could, however, not be used for all of them, due to a relatively high demand of samples during the development and a limited supply of the test patterns. For the 50x objective (Fig. 30, Fig. 31), the visually observed limits of resolution (for the settings used during this acquisition) are roughly the same for both lasers and both sides. Structures between pattern 9-10 and 9-11 can be identified, corresponding to a pitch size of 1100 nm to 1230 nm. The 100x objective (Fig. 32, Fig. 33) shows a stronger difference between the two lasers. The resolution from front and backside is again quite similar. For the 1064 nm laser, and 100x objective, pattern 9-10 (1230 nm pitch size) can still be seen and for the 1300 nm laser pattern 9-8 (1550 nm pitch size). All these pitch sizes are visually observed limits of resolution, which is how the performance of the FIB created SILs was measured in this work. For future

experiments with FIB created SILs it has to be mentioned that an edge signal can be used for quantitative resolution analysis. This means collecting intensity values over a sharp edge in an image by doing a line scan. These intensity values are then fitted with an error function, from which the derivative is created to obtain a Gaussian point spread function. The full width at half maximum of the Gaussian point spread function finally gives the resolution according to the Houston criterion and consistent with the Sparrow criterion (see page 36). Further details and examples of this quantitative resolution analysis can be found in [36] and [18].

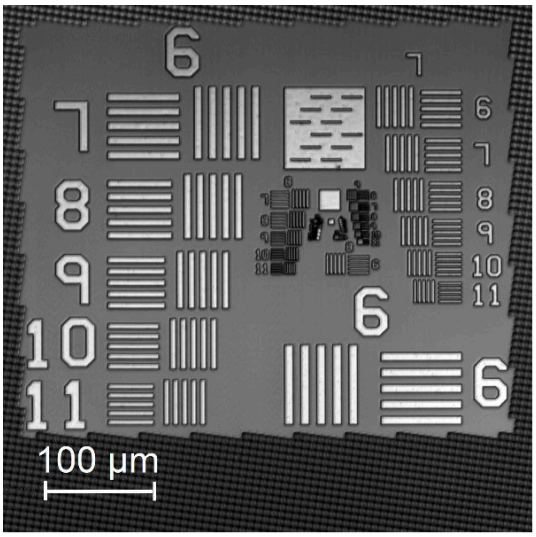

Fig. 29: Overview of a resolution test pattern acquired from the back of a chip through bulk silicon (at 20x, 0.4 NA, 1064 nm). Pitch sizes vary from 15.63 µm down to 0.27 µm.

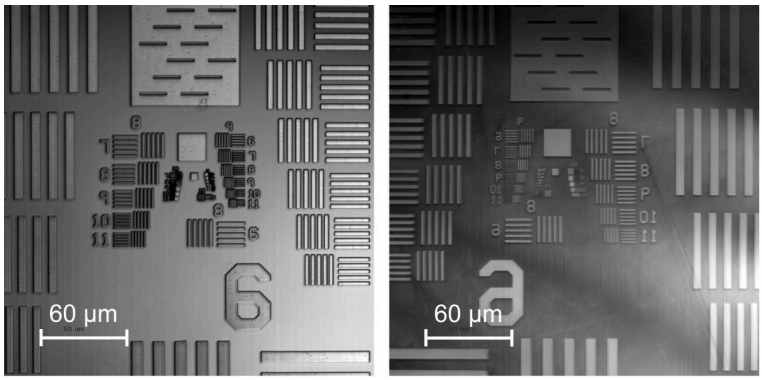

Fig. 30: Image of a resolution test pattern from the front (left) and through the backside (right) of a chip. A 50x, 0.7 NA objective and 1064 nm wavelength was used.

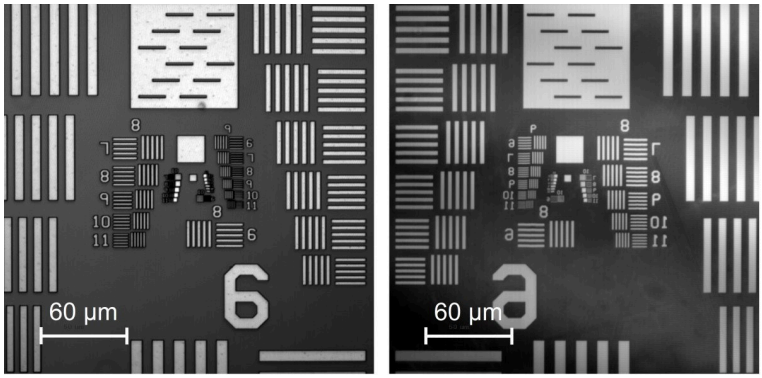

Fig. 31: Image of a resolution test pattern from the front (left) and through the backside (right) of a chip. A 50x, 0.7 NA objective and 1300 nm wavelength was used.

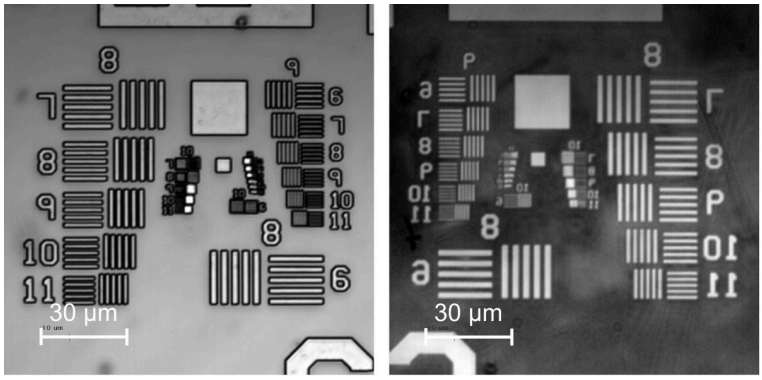

Fig. 32: Image of a resolution test pattern from the front (left) and through the backside (right) of a chip. A 100x, 0.5 NA objective and 1064 nm wavelength was used.

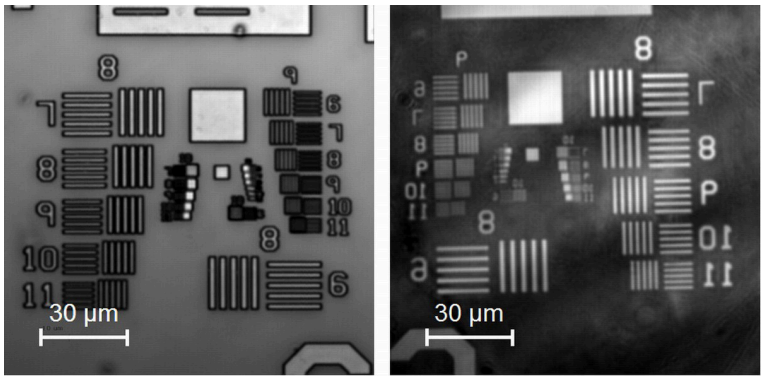

Fig. 33: Image of a resolution test pattern from the front (left) and through the backside (right) of a chip. A 100x, 0.5 NA objective and 1300 nm wavelength was used.

From the images in Fig. 30 to Fig. 33 it can be observed that the main problem for backside imaging is the reduced contrast and the additional distortions from defects in the volume or on the surface of the silicon material. Both of which are to be compensated by using FIB created SILs.

2.10 Towards neglecting diffraction - geometrical optics

After analyzing the effect of diffraction on the imaging properties of an optical system and showing how the corresponding calculations can be simplified by approximations and Gaussian beams, the next level of simplification is to neglect diffraction overall. The influence of diffraction is reduced, if the optical system has apertures or lenses with physical dimensions much larger than the wavelength. One parameter, which helps to define this condition, is the previously introduced Fresnel number

$$N_F = \frac{\pi r^2}{\lambda z}. \qquad ((9))$$

It can be used to distinguish between Fresnel (near-field) and Fraunhofer (far-field) diffraction, as mentioned earlier in chapter 2.1. The relation between the dimension of the aperture r and its distance to the screen z is

the key parameter for this distinction, while keeping the wavelength λ constant. The general rule is that Fraunhofer diffraction can be used if $N_F << 1$. Pedrotti [37] further refines this definition and extends it to the field of geometrical optics. It states that Fraunhofer diffraction occurs if $N_F < 10^{-2}$, Fresnel diffraction if $10^{-2} \leq N_F \leq 10^2$, and geometrical optics can be used if $N_F > 10^2$. Bergmann and Schaefer [38] further add that for geometrical optics $z >> z_R$ is needed, with z_R being the Rayleigh range (see (35)).

The concept of an infinitely small wavelength is the basis for geometrical optics. It neglects interference and diffraction arising from the wave nature of light. Wavefronts or rays are assumed to be manipulated merely by reflection and refraction. This approximation can in many cases be well accepted due to its convenient handling. Doing so while adding the condition that only rays close to the optical axis (paraxial rays) are to be considered, leads to an opening angle $\sin \alpha \approx \alpha$, and thereby to what is called first-order, paraxial or Gaussian optics. It is an efficient way of doing lens calculations and also used in the practical example in chapter 5.1.9.

This chapter discussed the effects of diffraction on the imaging process, leading to the definition of resolution and how it can be improved during the set-up of a confocal laser scanning microscope (LSM) by an additional aperture. The capabilities of the LSM used in this work were illustrated in terms of resolution, and finally it was shown under which circumstances the simplified methods of geometrical optics can be applied.

3 Immersion microscopy in silicon

3.1 Subsurface imaging in silicon

When a light wave travels from one medium to another medium of higher optical density, e.g. during an optical backside analysis of a microchip from air to bulk silicon, wavelength and speed are reduced while the frequency remains constant. Imaging inside a material with a higher index of refraction n (Fig. 34) should therefore be instantly beneficial to the resolution – we will see shortly why it is not always like that.

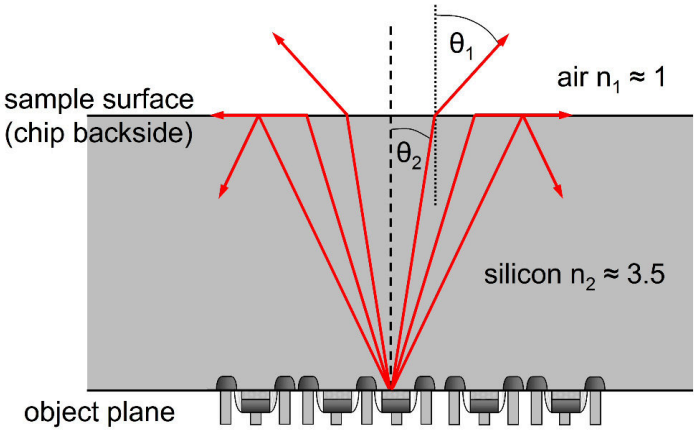

Fig. 34: Refraction at the silicon-air-interface during an optical investigation of a microchip from the backside. The angle θ_2 is illustrated at about 11°. Once θ_2 approaches 17°, total internal reflection occurs and the reflected or emitted signal beyond this angle is lost. Due to the absorption of silicon only light in the infrared range is transmitted, where $n_{Si} \approx 3.5$.

Fig. 34 illustrates why a material of higher optical density does not instantly improve the resolution. Refraction at a surface coplanar to the

object plane limits the opening angle in object space and thereby the resolution. The angle θ_2 is illustrated at about 11° in the presented example (Fig. 34). Once θ_2 approaches around 17°, total internal reflection occurs inside the silicon for infrared imaging and the reflected or emitted signal beyond this angle is lost. The angles at the interface can be described by Snell's Law.

$$n_1 \sin\theta_1 = n_2 \sin\theta_2 \tag{40}$$

Either side of Snell's Law can be found again in the numerical aperture (41), if corresponding to an opening angle against the optical axis used for microscopy.

$$NA = n \sin\theta \tag{41}$$

Ernst Abbe introduced the concept of the numerical aperture (NA) (41) [25] p. 215. At the same time he also recognized a general definition of the resolving power [25] p. 215 upon which the Rayleigh criterion (29) for resolution in air ($n_{air} \approx 1$), or either of the other criterions mentioned in chapter 2.5, are based. It can be said that the smallest resolvable pitch size is proportional to the vacuum wavelength, divided by the refractive index in object space, times the sine of the opening angle in object space. Writing this in terms of the parameters from Fig. 34 leads to equation (42).

$$Res_{Rayleigh} = \frac{0.61\lambda}{\sin\theta} \tag{(29)}$$

$$Res \propto \frac{\lambda_0}{n_2 \sin\theta_2} \tag{42}$$

3.2 Refractive solid immersion lenses in silicon

It can be seen in (42) that, for a coplanar sample, the reduced wavelength (λ_0/n_2) does not contribute to a better resolution, but is compensated by the opening angle (θ_2 in $n_2 \sin\theta_2$). This motivated solid immersion lens microscopy as invented by Mansfield and Kino [4] and the concept of a central refractive solid immersion lens (rSIL). Two types of SILs are used in the course of this work, those working by the principles of refraction (rSILs) and those by diffraction (dSILs). The basic principle of a central rSIL in silicon is to bring θ_2 closer to θ_1 by creating a round surface, which is part of a virtual hemisphere. Several solutions with silicon rSILs placed on the surface of the sample have been successfully presented [14], [17], [18]. The concept of this work is to create rSILs (and dSILs) directly out of the bulk silicon, as illustrated in Fig. 35 and motivated in chapter 1. The modified surface of the sample thereby becomes part of the imaging system immersed in silicon. An improvement in resolution can thus be achieved without modifying the microscope, or having any physical contact between microscope and sample. Furthermore the SIL is created in closest contact to the sample possible, without an air gap. The influence of the air gap is discussed in [5]. The SIL out of bulk silicon can be precisely positioned and is attached to the sample (until removed, see chapter 5.1.8). This reduces the effect of vibrations or thermal drift during long term acquisition. A focused ion beam (FIB) is used to create the SILs (see chapters 4 and 5). Only the cap of a virtual hemisphere is actually exposed for the rSIL in order to have an efficient process which can be realized with the FIB and still be removed by polishing, if needed (5.1.8). A similar idea was presented by Koyama [19] using mechanical milling with a computer numerical controlled (CNC) lathe to “form silicon substrate into solid immersion lens” (FOSSIL). It showed impressive optical results, but permanently altered the sample and, to the author’s knowledge, was not pursued any further. The overall goal is to develop an efficient SIL creating

FIB process, which is to improve the resolution of an infrared microscope for backside analysis through bulk silicon.

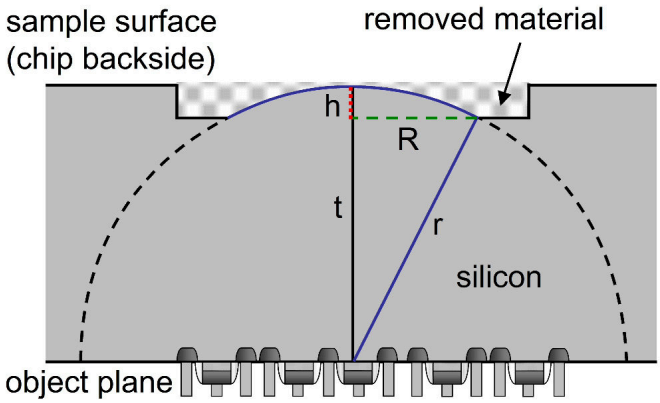

Fig. 35: A central rSIL created out of silicon with height *h*, radius of rSIL *R*, radius of curvature *r* and sample thickness *t*. Only the cap of a virtual hemisphere is actually exposed in order to have an efficient process which can be realized with the FIB. A practical aspect of a central rSIL is the large tolerance regarding *t* and *r*. *t* does not have to be exactly equal to *r*, as in this illustration.

The central rSIL in Fig. 35 is illustrated with a sample thickness *t* equal to the radius of curvature *r*. However, the central rSIL still brings significant optical benefit, even if this condition is not satisfied. The experiments in chapter 5.1 show that the central rSIL can improve resolution over a wide range of $t < r$. Further details on this topic are discussed during the analysis of experimental results in chapter 5.1.9. A drawback of this deviation is that, according to the SIL theory presented by Born and Wolf [22], aberration-free imaging inside a high-index sphere only occurs in the aplanatic points. The ideal central rSIL focuses on the first aplanatic point, which is in the centre of the virtual hemisphere. The second aplanatic point lies $r \cdot n_{air}/n_{si}$ below the centre, which leads to the set-up of the aplanatic rSIL. The sample thickness for an aplanatic rSIL is $r + r / n_{Si}$ with the parameters of Fig. 35. The aplanatic rSIL does not only reduce the expansion of the opening angle in air but focuses it towards the objective.

It offers even more optical improvement than the central rSIL: the magnification and inversely the resolution are influenced in the central case by n and in the aplanatic by n^2. Furthermore spherical aberration and coma are zero in both cases, and astigmatism as well for the aplanatic rSIL [39]. Unfortunately the aplanatic rSIL achieves all that at the cost of a significantly reduced tolerance in sample thickness with respect to radius of curvature and a larger needed lens area. Both of which can not yet be accepted for the presented FIB SIL processes. This is why the central set-up is used for the rSILs in this work.

3.3 Diffractive solid immersion lenses in silicon

Apart from SILs relying on the principles of refraction (rSILs), as introduced in the previous chapter, SILs utilizing the diffraction of light (dSILs) are also a topic of this work. Fig. 36 compares four types of SILs, which can be used for subsurface imaging. The just introduced spherical rSIL works in a wide spectral range, if the transparency of the material allows for that. A relatively large amount of material needs to be removed to create such a shape, though.

Augustin-Jean Fresnel invented the Fresnel lens [40] in search for a lens with imaging properties comparable to a spherical lens, but a reduced demand in material. The Fresnel lens can be seen as a flat version of the spherical lens, while maintaining the same radius of curvature. This is achieved by virtually cutting angular segments of the spherical surface and shifting them onto the same level. Such a shape can be generated in small dimensions e.g. with a diameter of 600 µm by direct laser patterning [41] or with a diameter of 250 µm by using a design from computer generated holography in a combined FIB patterning and reactive ion etching process [42]. Meeting the ideal surface topology is challenging in either case.

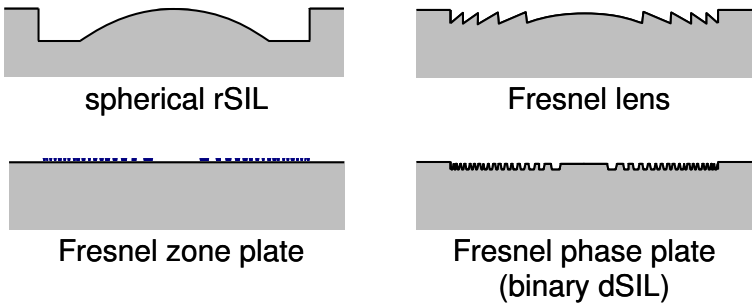

Fig. 36: Profiles of four possible ways to modify the surface of a sample creating a SIL in silicon. The spherical refractive SIL and the binary diffractive SIL are the two types realized in this work.

A helpful simplification can be made, if the lens is to be used in a narrowband or monochromatic application such as laser scanning imaging. In that case, the surface of the sample can be divided into circular areas from which neighbouring rays reach the focal point P (see Fig. 37) by a difference in path length of an even or odd multiple of half a wavelength. Accordingly they interfere constructively or destructively, and the first is needed to create an image. The circular areas, called zones, leading to destructive interference can be blocked by an opaque layer and create a Fresnel zone plate. Depending on the design of the zones, it can behave comparable to a spherical lens, while being entirely flat. A drawback of this type of lens, though simple in its making, is a low efficiency. Not surprisingly, since a significant amount of the lens surface is blocked. Calculations of the zonal radii were presented by Brunner et al. [43] and are discussed in chapter 3.4.

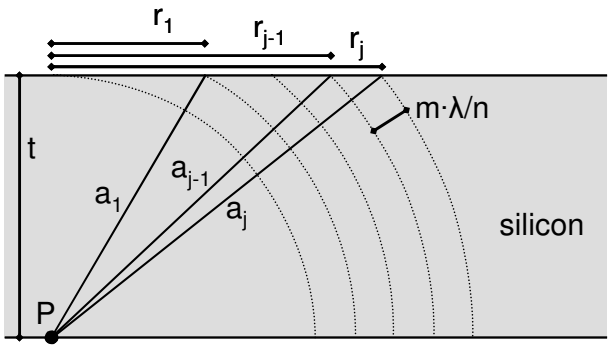

Fig. 37: Defining radii on the surface from which neighbouring rays reach the point *P* in constructive or destructive interference according to the theory presented by Brunner et. al. [43].

More efficient than the Fresnel zone plate, while being only slightly more complex to create, is the Fresnel phase plate. For this, the areas leading to destructive interference in the focal point do not get blocked, but instead are shifted (Fig. 38). Thereby the path length is adjusted to an even multiple of half a wavelength, resulting in constructive interference and a working immersion lens. The first and last SIL presented earlier in Fig. 36, the spherical rSIL and the Fresnel phase plate, are the two types realized in this work by FIB processing. The latter is referred to as binary dSIL or just dSIL from now on.

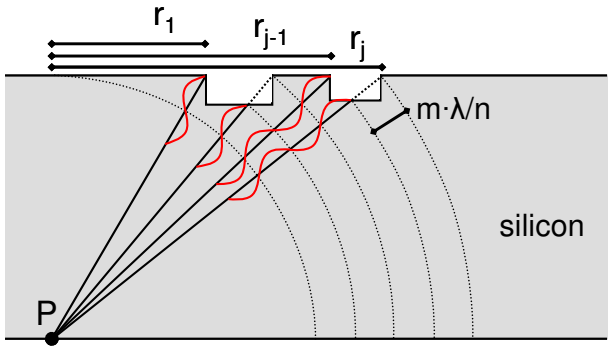

Fig. 38: Creating a Fresnel phase plate based on the calculations illustrated in Fig. 37. The areas of destructive interference on the silicon surface are shifted, thereby shortening the path length of the rays and creating constructive interference.

3.4 Calculating the radii of a binary diffractive solid immersion lens

Brunner et al. [43] demonstrated the calculation of the zonal radii r_1 - r_j, as illustrated in Fig. 37 and Fig. 38. Based on this, they created a dSIL with “a circular aperture of 1.6 mm” in a combined electron-beam and reactive ion etching process. Their calculations are quoted and discussed in this chapter for better understanding and to apply them to the dSIL creating FIB process. The parameters are the sample thickness *t*, the focus shift factor k (not to be mistaken for the $k = 2\pi / \lambda$ from chapter 2), the virtual radius of curvature kt, the refractive index of silicon n, the order of diffraction m, the used wavelength in air λ_0 and an enumerating integer j. The latter is not to be mistaken for the imaginary unit in this context. These parameters and the distances a_j, a'_j, Δl_j and $\Delta l'_j$ (as illustrated in Fig. 39) are used to calculate the zonal radii.

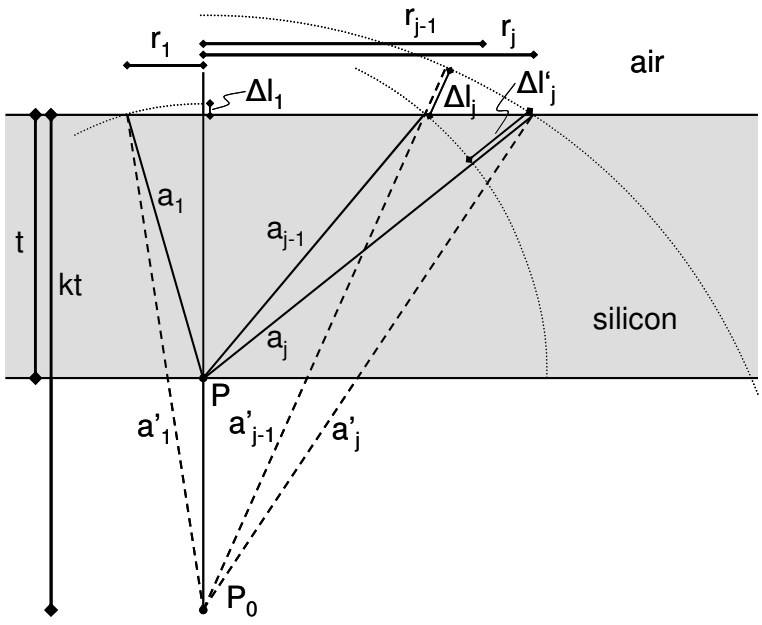

Fig. 39: Illustration of the parameters used for calculating the zonal radii of the dSIL based on [43]. Due to their radial symmetry, radii to the left and right of the centre are treated equally.

The zonal radii are defined as a function of the optical path length to the focal point P_0. Finally this length is expressed as a multiple of half a wavelength to determine constructive or destructive interference. (Note that all “l”s are small “L”s and not capital ”i”s.)

The calculations start out by expressing the two distances in air Δl_1 and Δl_j by the same multiple of a wavelength, which means corresponding rays would interfere constructively. Distances inside the silicon are multiplied by n to achieve an optical path length.

$$na_1 - (\Delta l_1 + nt) = m\lambda_0 \tag{43}$$

$$na_j - (\Delta l_j + na_{j-1}) = m\lambda_0 \tag{44}$$

Next, the difference between the two adjacent outer rays going from P to the surface is defined, and similarly between those going from P_0 to a circular path around P_0.

$$a_j - a_{j-1} = \Delta l'_j \tag{45}$$

$$a'_j - a'_{j-1} = \Delta l_j \tag{46}$$

Solving (44) for $(a_j - a_{j-1})$ and combining it with (45) leads to

$$n\Delta l'_j = m\lambda_0 + \Delta l_j. \tag{47}$$

The primary rays from P and P_0 are $a_1 = t + \Delta l'_1$ and $a'_1 = kt + \Delta l_1$ for the starting value of $j = 1$. The following rays can be calculated by iteration and for a_j by additionally using (47).

$$a_j = t + j\frac{m\lambda_0}{n} + \frac{1}{n}\sum_j \Delta l_j \tag{48}$$

$$a'_j = kt + \sum_j \Delta l_j \tag{49}$$

Solving each equation for the iteration and inserting it into the other yields

$$a_j = t + j\frac{m\lambda_0}{n} + \frac{1}{n}(a'_j - kt) \text{ and} \tag{50}$$

$$a'_j = na_j + t(k - n) - jm\lambda_0 . \tag{51}$$

The next two equations are derived from Fig. 39 while using the Pythagorean theorem.

$$t^2 + r_j^2 = a_j^2 \tag{52}$$

$$k^2t^2 + r_j^2 = a'_j{}^2 \tag{53}$$

(52) is solved for r_j^2 and put into (53). From this, a'_j is determined and inserted into (51). The result is

$$\alpha a_j^2 + \beta a_j + \chi = 0 \tag{54}$$

with

$$\alpha = (1 - n^2) , \tag{55}$$

$$\beta = 2n[t(n - k) + jm\lambda_0] \text{ and} \tag{56}$$

$$\chi = t^2(2kn - n^2 - 1) + 2t(k - n)\, jm\lambda_0 - j^2(m\lambda_0)^2 . \tag{57}$$

The equations of (54), (55), (56), and (57) are verified in the Appendix 7.1. In the second to last step a_j is calculated from (54) with the quadratic equation $x^2 + px + q = 0$. Its solutions are $x_{1,2} = \frac{p}{2} \pm \sqrt{\frac{p^2}{4} - q}$, and in this case $x = a_j$, $p = \beta / \alpha$ and $q = \chi / \alpha$. The final step is to express r_j according to (52) as

$$r_j = \sqrt{a_j^2 - t^2} \tag{58}$$

and to insert the solutions of a_j from the quadratic equation. A compact result can be found for a focal shift factor of k = 1 (t = kt), which optically creates a dSIL corresponding to a central rSIL, and with an order of diffraction m = 1. This results in zonal radii, which have a difference in optical path length of a full wavelength and thereby create constructive interference in the focal point P.

$$r_{j(k=1)} = \sqrt{2j\frac{\lambda_0}{n-1}t + (j\frac{\lambda_0}{n-1})^2} \tag{59}$$

For the zones of the dSIL, also the radii of destructive interference need to be calculated. This is achieved by setting m = 0.5, leading to values of radii which create a difference in path length of 0.5, 1.0, 1.5 … wavelengths and thereby alternating destructive and constructive interference. The area between every other pair of adjacent radii is shifted during the making of the dSIL to achieve constructive interference for all rays coming from the lens surface. An important final aspect is the largest usable radius of the dSIL in order to have an upper limit for the calculation of the radii. It depends on the numerical aperture of the microscope objective used with the dSIL. For a dSIL with k = 1 it is

$$r_{max} = t \cdot \tan(\sin^{-1} NA_{Obj}). \tag{60}$$

This entire theory is applied in the program code creating the bitmaps for the dSIL FIB process in chapter 7.4.

4 Basics for refractive and diffractive FIB created SILs

4.1 Hardware used: OptiFIB

Focused Ion Beam (FIB) machines qualify for wide use in microelectronics due to an enormously useful combination of interactions. A liquid metal tip as source plus particle beam optics are used to form an ion beam that is scanned over previously selected areas and acts like a local plasma. It can perform many functions on a small spot that plasma reactors apply to the whole chamber: pure ion milling (called sputtering in plasma reactors), reactive ion etching (called gas assisted etching in FIBs), and material deposition (PECVD in plasma reactors). All these microinvasive techniques are accompanied by secondary electron or ion emission that can be used for real time imaging while the material gets modified.

Our laboratory is equipped with the OptiFIB from DCG Systems, a specific FIB edition that plays a very important role in the presented experiments. The OptiFIB is a focused ion beam tool with the unique feature of a coaxial ion/photon beam for non-invasive real-time imaging of the sample through the bulk silicon of a chip's backside and through a passivated frontside, e.g. of samples planarized by chemical-mechanical polishing (CMP). This feature is used mainly for circuit edit, to create probe points connecting buried conductors and for sample analysis by cross sectioning. This work also utilises the tool's ability to do micro machining for the creation of optical elements in silicon.

The three main parts of the OptiFIB can be seen in Fig. 40: computer workstation, electronics console unit and ion column unit. In our case the “Visually Integrated Software for Test and Analysis” (“VISTA”) running on a UNIX operating system is the graphical user interface (GUI) of the workstation. Current systems are being equipped with the Windows-based “FUSION” software. The electronics console unit contains power supplies, several controllers, the xenon light source and the roughing pump, among other things. One benefit of the separate console unit is to keep vibrations away from the ion beam column. The ion column unit (Fig. 41) includes the turbo pump, two ion pumps, the vacuum/specimen chamber, the ion column control boards, the chemical delivery system, the ion column (Fig. 42, Fig. 43, Fig. 44) itself and more.

Fig. 40: The OptiFIB tool with its three main parts – computer workstation, electronics console unit and ion column unit. It was purchased while DCG Systems was part of NPTest.

Fig. 41: The OptiFIB's ion column unit.

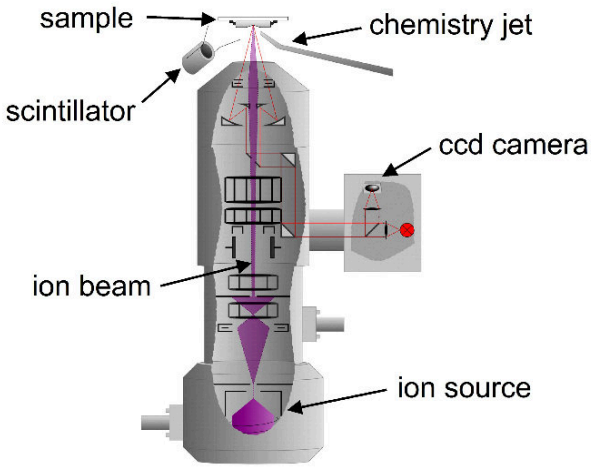

Fig. 42: Sketch of the OptiFIB's ion column based on [44]. The drawing shows the ion beam and the coaxial optical beam. Note that not only the ion column is operated at vacuum, but also the sample in the specimen chamber. The individual elements, particularly the ion source, are not drawn to scale for better illustration.

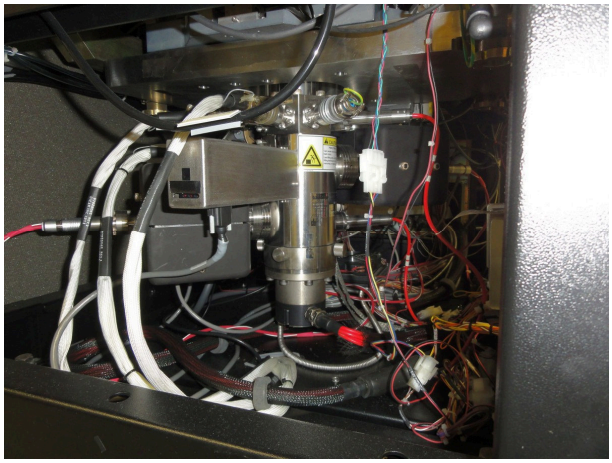

Fig. 43: The OptiFIB's ion column. The ion source is inside the column at the very bottom.

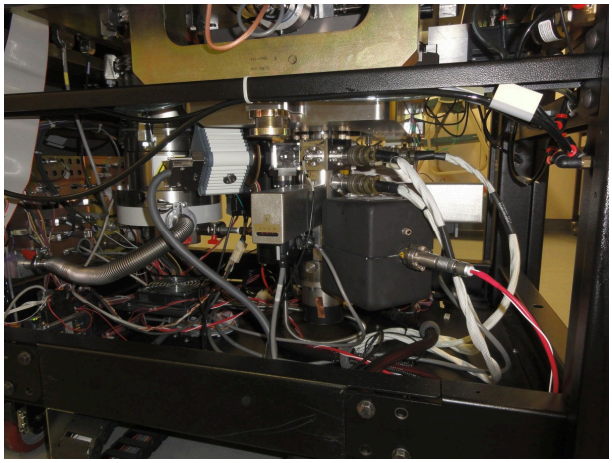

Fig. 44: The OptiFIB's ion column. Among other things, the CCD camera can be seen close to the middle with its light grey cooling fins.

As mentioned earlier, a specific characteristic of the OptiFIB is the photon imaging system coaxial to the ion beam [45] for real-time observation of the sample without particle beam scanning. This is possible by the application of Schwarzschild-Cassegrainian optics. In this optical set-up, the centre of the path of light is not directly occupied by lenses. Thereby the ion beam can pass through unaffected (see final lens of the OptiFIB column in Fig. 45, taken from [46]). The optical image is illuminated by a

xenon lamp sitting in the electronics console unit and connected to the column through a light guide. The spectrum can be influenced by a set of five optical filters. At TUB, four of these filters have a bandwidth of 70 nm at 500 nm, 850 nm, 950 nm and 1000 nm. The fifth has a narrower bandwidth of 10 nm at 950 nm. A 9 x 7 mm, 1380 x 1024 pixel, infrared-sensitive Hamamatsu C4742-95ER CCD camera (Fig. 44) captures the final image.

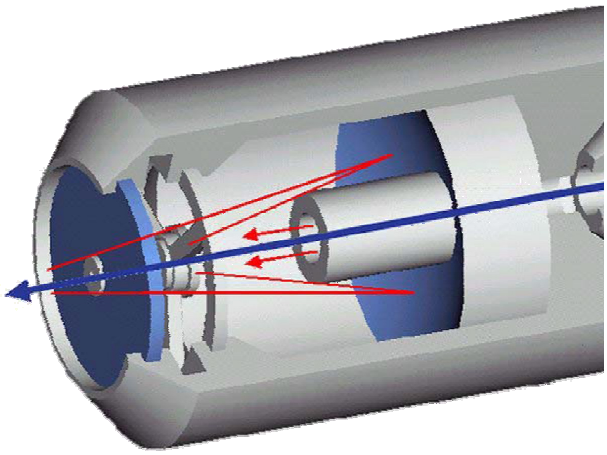

Fig. 45: The final lens in the OptiFIB column with Schwarzschild objective from [46].

Apart from the optical image, a common secondary electron FIB image can also be acquired in the OptiFIB. The secondary electrons created by the ions impacting on the surface of the sample are used for this. A scintillator (Fig. 46) inside the specimen chamber in the Everhart-Thornley configuration [47] p. 249 captures secondary electrons, which are guided by antennas. The voltage at the antennas should be kept at the lowest possible level, in order to avoid influence on the ion beam placement. The scintillator generates photons when the secondary electrons are scattered. These photons are guided to a photomultiplier tube (PMT) by a light pipe. The PMT converts the photons into electrons and amplifies their signal. The reason for the conversion from secondary electrons to photons and again to electrons is that the multiplier tube needs to be sealed from the

FIB chamber. The intensity of the final signal along with the position of the ion beam, at the time of scanning, is used to create the FIB image.

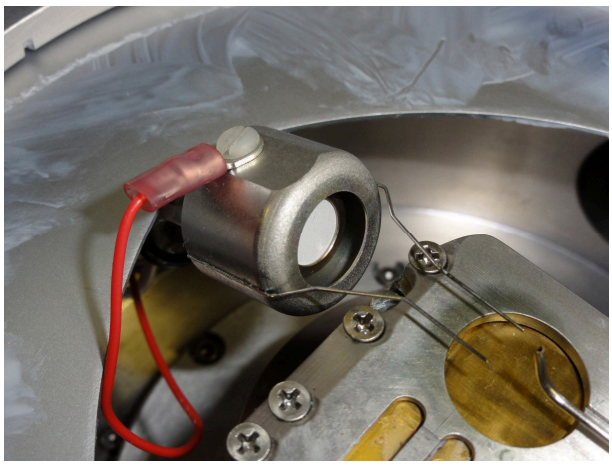

Fig. 46: Scintillator inside OptiFIB's specimen chamber.

Imaging is just one application of the OptiFIB. Another important task is the modification of material. Several options exist in this area. The tool available to the author offered two types of chemistries for insulator deposition and a molybdenum chemistry ($Mo(CO)_6$) for conductor deposition. Furthermore a selection of etch chemistries helps to remove material more efficiently and selectively than by unassisted ion beam milling alone: Xenon difluoride (XeF_2) for dielectric as well as semiconductor etch and the iodine-based chemistry ethylene diiodide (EDI, $C_2H_4I_2$) generally used for metal etch. EDI can also be added for silicon etching, as discussed in 4.3. The chemistry option developed by DCG Systems specifically for copper etch, was not installed. All of these chemistries are kept in their temperature controlled crucibles in the chemistry manifold (Fig. 47) and are supplied to the specimen chamber via the chemistry injector jet (Fig. 48).

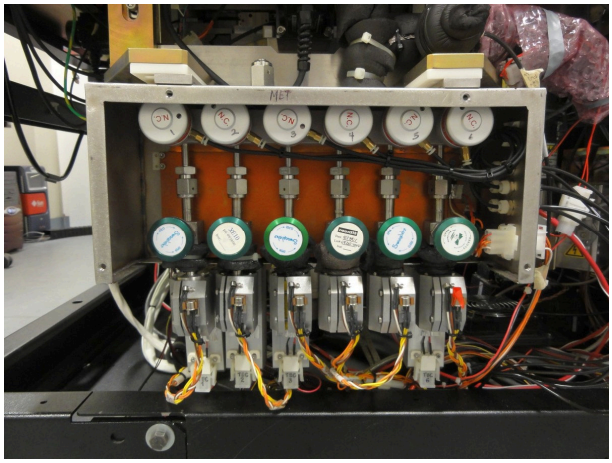

Fig. 47: Chemistry manifold in the OptiFIB ion column unit.

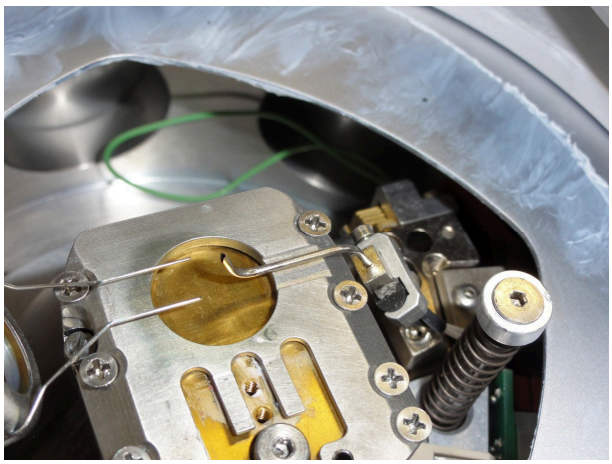

Fig. 48: Chemistry jet supplying the chemistries to the OptiFIB's specimen chamber.

Both of the available etch chemistries were taken into account for the creation of SILs in silicon. While the first SILs presented in this work were successfully created just by FIB milling alone (chapter 5.1), this method showed certain limitations (see 4.2), which led to EDI-assisted FIB processes (chapters 5.2 and 5.3).

A very important factor for the properties of FIB induced reactions are the exact parameters of the ion beam. It is made up of gallium ions emitted from a liquid metal ion source (LMIS) (Fig. 49). The LMIS is partially

heated and consists of a reservoir feeding liquid gallium to a needle from which the ions are drawn by a strong electric field [48]. A series of electrostatic lenses then focuses the beam inside the column and finally onto the sample. Tab. 3 in the Appendix on page 163 lists a series of ion beam diameters at various beam currents. These are useful for estimating the micro machining behaviour of the ion beam (e.g. later in 5.3.4). For further details on the construction of the OptiFIB column, see [46] or [49].

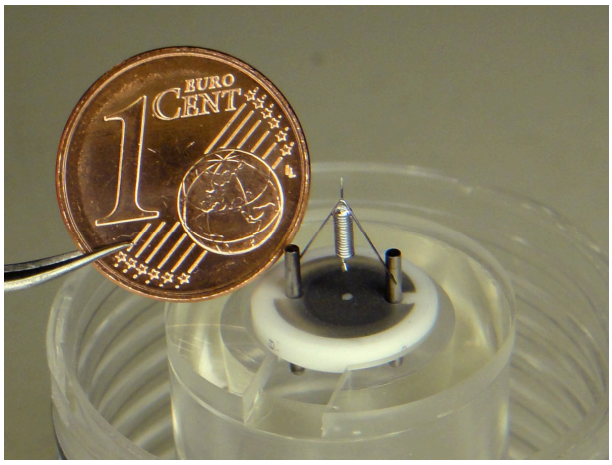

Fig. 49: The liquid metal ion source creating the gallium ion beam.

Controlling the scanning of the ion beam determines how the sample is being processed. The beam of the OptiFIB generally scans the area defined by the user (FIB box) line by line. In regular mode, it moves continuously throughout each line and then retraces back to the starting point. During this scanning, every spot on the sample within the FIB box is exposed to the ion beam for a certain amount of time, which is called the dwell time. One of the key features of the OptiFIB for the development of focused ion beam created refractive and diffractive lens techniques is the bitmap mode. It can be used to precisely control the motion of the ion beam. In this mode, a bitmap file is loaded into the OptiFIB system to control the dwell time of the ion beam inside the FIB box within a 512 by 512 array. The bitmap file needs to have an equivalent resolution of 512 by

512 pixels, 8-bit greyscale values (“0”-“255”) and has to be saved as an uncompressed TIFF file. The dwell time of every pixel area can be calculated from its pixel value using formula (61). Higher greyscale values result in a brighter pixel colour and a longer dwell time. This is demonstrated in Fig. 50 and Fig. 51.

$$DT = 200\ ns,\ \text{if } gs = 0 \text{ or } 1 \text{ (beam is blanked at 0)} \qquad (61)$$
$$DT = 300\ ns + 50(gs - 2)\ ns,\ \text{if } gs \in \{2, \dots, 255\}$$

DT : dwell time [ns]
gs : greyscale value [-]

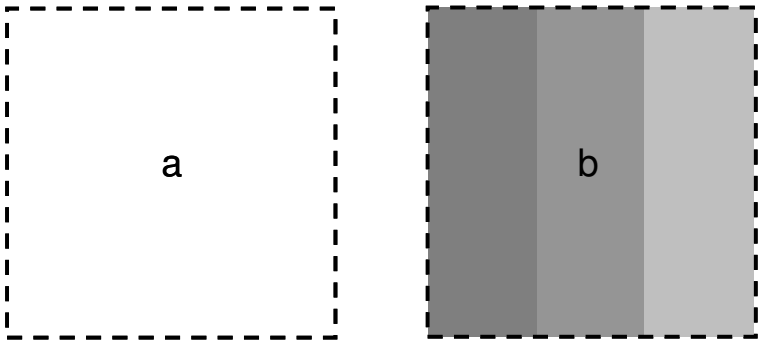

Fig. 50: Explaining the OptiFIB bitmap mode. Case “a” showing regular beam scanning without a bitmap (constant dwell time) and case “b” with a simple 3-level bitmap drawn into the FIB box for illustrating purposes (brighter pixel colours create longer dwell times).

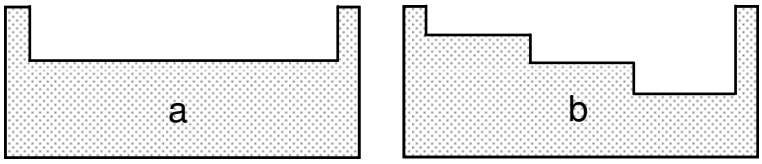

Fig. 51: Explaining the OptiFIB bitmap mode. Theoretical cross sections created with the FIB boxes from Fig. 50: case “a” showing a flat trench due to regular beam scanning and case “b” a stair-shaped trench according to the 3-level bitmap used in this example.

The bitmaps used to create SILs with the OptiFIB are more complex than the one in Fig. 50 case “b”, though they follow the same basic formula (61). A bitmap for a refractive SIL with a spacer around the lens can be seen in Fig. 52. Brighter pixels towards the edge of the lens shape lead to a slower movement of the ion beam and to the removal of more material. This type of bitmap is used in chapter 5.2 for a single-step chemistry-assisted rSIL FIB process. Fig. 53 presents a bitmap used for binary diffractive SILs or Fresnel phase plates in chapter 5.3. It basically consists of two greyscale values distributed in a fixed pattern. The pattern is determined by properties of the sample and the desired qualities of the dSIL as discussed in chapter 3.3 and 3.4.

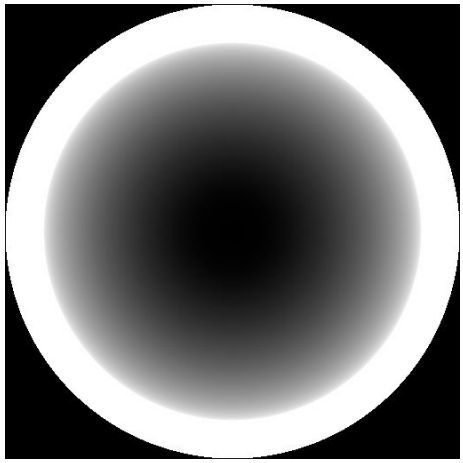

Fig. 52: Example of a bitmap used to shape a refractive SIL in bitmap mode, including a spacer around the lens itself (bright outer ring).

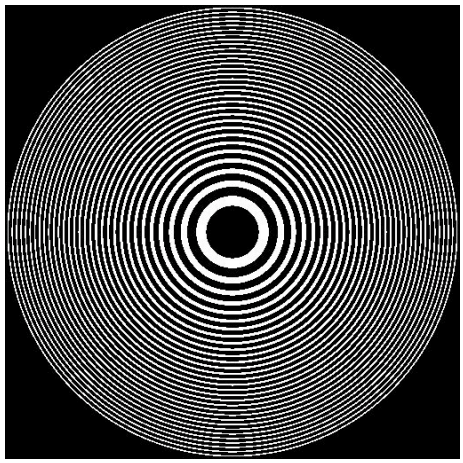

Fig. 53: Example of a bitmap used to shape a binary diffractive SIL in bitmap mode.

4.2 Etching and milling with the OptiFIB

Numerous efforts were made at TUB to fully characterize the FIB etching processes in search for the ideal SIL creating FIB recipe [49–52]. A series of parameters have to be taken into account for the characterization. Among them are the ion beam current and its corresponding beam diameter. From this the beam overlap can be calculated when combined with the FIB box size. Beam overlap occurs, if the ion beam diameter (see Tab. 3 on page 163) is bigger than the pixel size, which is the FIB box size divided by 512. The dwell time of the ion beam can be controlled as previously explained in Fig. 50 and Fig. 51. Summing up the dwell times of all of the pixels in the FIB bitmap leads to the frame time, also referred to as retrace time, which indicates the time it takes the ion beam to reach its starting position after one full scan of the FIB box. A minimum retrace time can be set in the “FIB operation recipe” panel of the GUI to avoid gas depletion during a chemistry-assisted process. Further parameters, which are usually well monitored and held constant, are the temperature during the process and the pressure inside the FIB chamber. Especially important

for a chemistry-assisted process are also the type of chemistry used and the distance of the chemistry jet to the sample surface.

Using specific values for the mentioned beam parameters and a certain processing time lets one define the amount of ions hitting the sample. The number of silicon atoms removed during the etching process can be determined by analysing the etched geometry. The ratio of these two values is the yield of the characterized etching process. This theory was carried out in practice in the above mentioned works [49–52]. The chosen etch geometries were stair shapes comparable to the theoretical structures of Fig. 51 and shown in a FIB image in Fig. 54. Unfortunately the thereby collected and calculated data could not be applied to the creation of spherical shapes for rSILs. The shapes created on the basis of this information did not meet the requirements of a spherical rSIL (Fig. 55, Fig. 56). One explanation for this is the angle of the ion beam incidence [53], [54], which stays perpendicular for the stair shapes and therefore does not have any influence. This is not the case for the spherical rSILs where the shape and thereby the angle of incident changes during the process. Another crucial difference between the stairs and the rSIL shapes for a chemistry assisted FIB process is the gas flow around the spherical rSIL, which can not be considered while characterising the process by stair shapes. All this led to the decision of directly working on spherical surfaces and thereby determine the needed processing parameters. From this, the process of the binary dSILs was also derived.

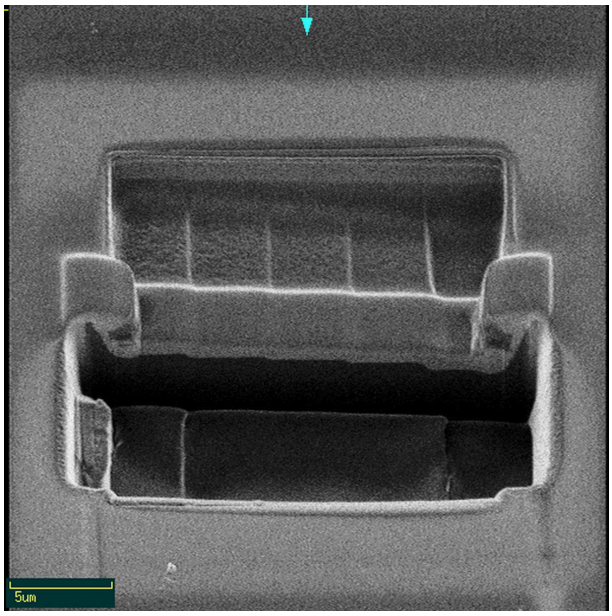

Fig. 54: Experiment carried out before the author's work. Characterising the XeF_2 FIB process by etching stair shapes into silicon [51].

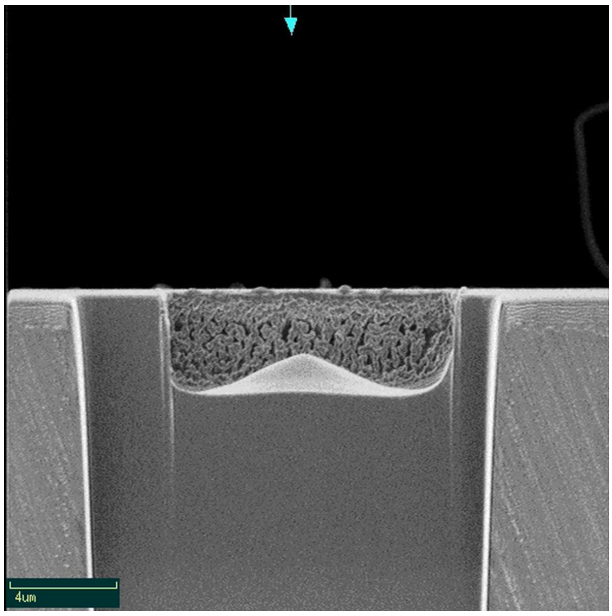

Fig. 55: An earlier experiment, prior to the author's work, in cross section. An rSIL creation based on the data gathered from characterising the FIB XeF_2 etching process was attempted. The result was a conical shape in a deep trench [49].

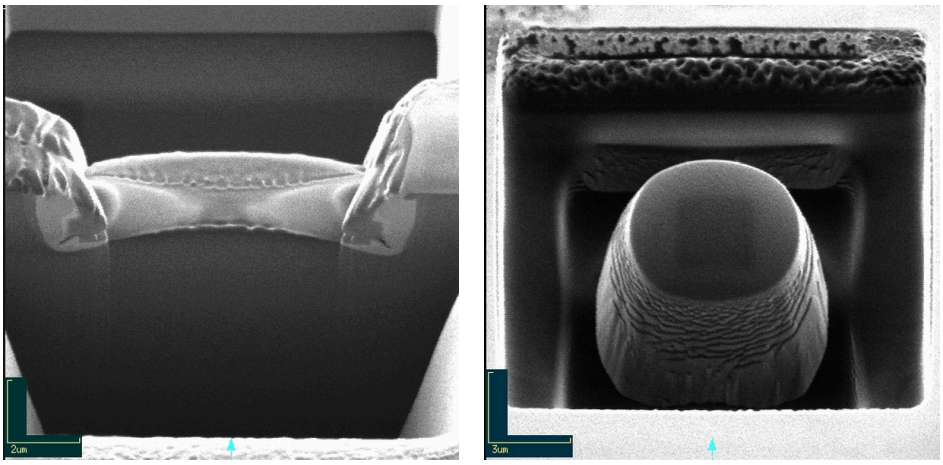

Fig. 56: Further experiments aiming at the rSIL creation by a XeF_2-assisted FIB etching process prior to the author's work. Both viewed at 30°. The resulting shapes were small and shallow (left) or closer to a cylinder than to a sphere (right). Both images taken from [50].

Creating an rSIL shape by unassisted FIB milling was the first chosen method. The basic parameters were set to be fixed within values which were found reasonable during preliminary experiments. They were a FIB box of about 37 by 37 μm^2, a 6 nA beam current and 10 minutes of processing time. With these basic parameters the ideal dwell times were identified: The removal of silicon material by unassisted FIB milling showed a linear correlation between dwell time and milled depth for values up to approximately 7.7 µs. This corresponds to a maximum greyscale value of 150 (out of 256). These values were measured from the experiment illustrated in Fig. 57. The cross section of a spherically etched shape was needed, because stair shapes could not be used for characterisation, as described in the previous paragraph. A FIB bitmap similar to the one introduced later in Fig. 58 and Fig. 59 with the full range of greyscales was applied. It can be seen in Fig. 57 that the material removal saturates at a certain point towards the edge. The border between metal, deposited for protection of the SIL surface in the cross section processing, and the original silicon surface do not match the expected

shape anymore. The greyscale value at this point was determined by measuring its distance from the centre of the lens shape in µm. This distance in µm can be expressed in numbers of pixels by using the size of the FIB box in µm and in pixels (fixed to be 512 by 512). Cross-multiplication leads to the distance between the point of interest and the centre in pixels, the corresponding greyscale value can then be taken from the bitmap used during the experiment. In the presented case it was around 150, setting the dwell time to 7.7 µs.

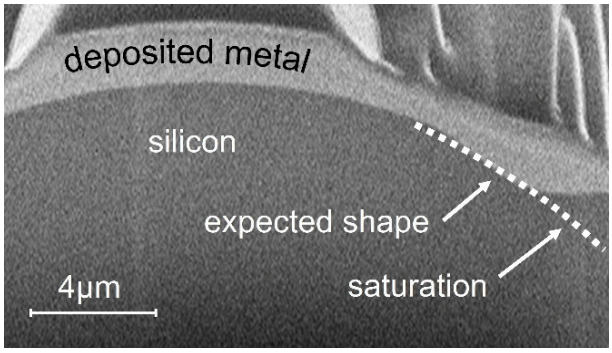

Fig. 57: Detailed feature of the point at which the material removal of unassisted ion beam milling saturates (= where the border between deposited metal and silicon leaves the expected shape), virtually tilted to a perpendicular viewing angle. Metal is deposited prior to the analysis to preserve the original surface during cross sectioning.

Using the just determined maximum greyscale value of 150 (out of 256) and the model of a hemisphere led to the creation of small rSIL shapes using unassisted FIB milling. The mathematical basis for the FIB bitmaps is the formula of a sphere (62), solved for z and using only positive z-values. For unassisted FIB milling as presented in chapter 5.1, these values were scaled linearly by the factor $s_{5.1}$ (63) to achieve the maximum dwell time of 7.7 µs on the edge of the rSIL (see limit of linearity between dwell time and material removal in previous paragraph). Fig. 58 shows the scaled model of a hemisphere, which needs to be shifted and inverted to achieve the final greyscale values as illustrated in Fig. 59. The full code for

programming the bitmaps including further details can be found in chapter 7.2. With this knowledge of the milling behaviour of the FIB and the programming of the FIB bitmaps, rSILs could be successfully created by unassisted FIB milling. Chapter 5.1 starting on page 87 presents the according lens shape and its optical benefits.

$$a^2 = x^2 + y^2 + z^2 \tag{62}$$

$$z_{5.1} = s_{5.1} \cdot (a^2 - x^2 - y^2)^{1/2} \tag{63}$$

x, y, z : Cartesian coordinates of the model of the sphere

a : value corresponding to the radius of the sphere

$z_{5.1}$: z values used to calculate the greyscale values for the rSILs of chapter 5.1

$s_{5.1}$: scaling factors used to calculate the z values for the rSILs

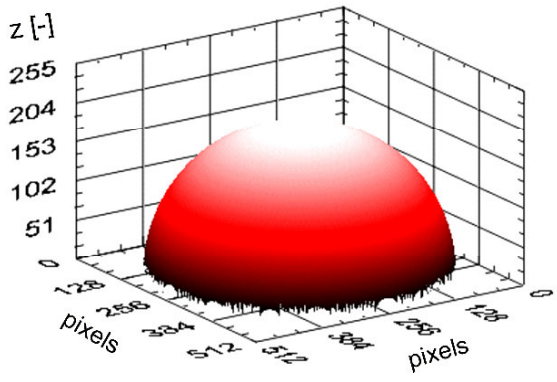

Fig. 58: 3D model of a hemisphere used to calculate the FIB bitmap for the creation of refractive SILs in silicon with FIB.

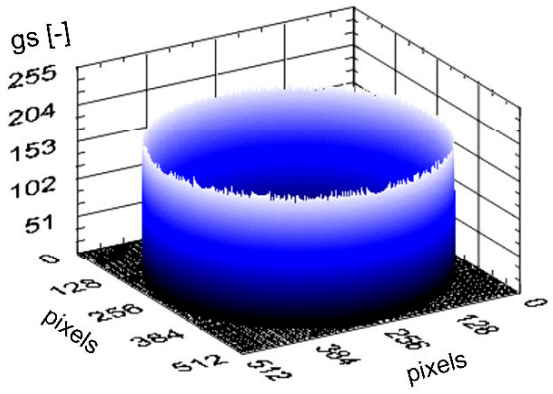

Fig. 59: 3D illustration of greyscale values of a FIB bitmap used to create refractive SILs in silicon with FIB.

4.3 Comparing chemistry-assisted etching processes of the OptiFIB

Even though the small rSILs created by unassisted FIB milling (chapter 5.1) showed to be of good shape and to bring significant optical benefit, the dimensions achievable by this method are limited. The material removed by unassisted FIB milling either successfully dissipates in the vacuum or redeposits. The latter is the reason for a saturation of the removal process beyond a certain dwell time, which limits the maximum achievable depth within the presented basic parameters. This also constrains the rSIL from having a stronger curvature and thereby a larger opening angle. Increasing the area of the lens to achieve an rSIL with larger opening angle by unassisted FIB milling doesn't help either, because the problem of redeposited material remains and the processing time increases drastically. A promising solution to all this is a chemistry-assisted FIB etching process like the one used in chapter 5.2, reducing redeposition [55] and removing material more efficiently.

The probably most common chemistry for FIB editing is xenon difluoride (XeF_2) [56], [57], also applied in the previously mentioned works [49–52]. It already initiates a chemical reaction when adsorbed by the silicon surface

[56], and the reactivity increases strongly when ions are added, which significantly improves the etching efficiency. The trade-off for this is the fact that it also etches spontaneously without the ion beam, possibly damaging the sample surface outside the area of interest. In addition it has a relatively complex etching characteristic, compared to the iodine-based chemistry EDI, which can also be used in the OptiFIB system available to the author.

For a brief comparison of the chemistries' impact on SiO_2 and aluminium, which are common materials for frontside FIB editing, chemistry-assisted FIB etching with XeF_2 removes SiO_2 at least ten times faster than unassisted FIB milling [58], [59], while the removal of aluminium stays mostly the same [60]. FIB etching with EDI removes SiO_2 about four times as fast and aluminium about twenty times as fast, again compared to unassisted FIB milling [61]. Note that all these processes depend on gas pressure. EDI is the second chemistry taken into account for rSIL creation. Its initial purpose is to etch aluminium in a FIB circuit editing process. The advantages of this iodine-based chemistry are the improved material removal, even for silicon, the absence of spontaneous etching and an etching behaviour very suitable for 3D surface modelling. The first step of the material removal with EDI is the milling of the ion beam, which is then enhanced by the chemistry. The removed particles are turned into volatile products, which do not redeposit and are therefore removed more efficiently. One drawback of the iodine-based chemistry is its lower efficiency on silicon compared to XeF_2. In summary, the iodine-based chemistry was chosen nonetheless, since the better definable etching characteristics, and the absence of unassisted etching (also discussed in the next paragraph) met the requirements of the rSIL creation in a single-step chemistry-assisted FIB process.

Being able to place SILs close to one another and also to examine the structure around the SIL is essential to the development and the application of the FIB created SILs. Both of these abilities are influenced by the effect of spontaneous etching during the FIB SIL process. Fig. 60 shows an experiment from the development of the method presented in chapter 5.2, which analyses this effect. The shape of the rSIL is not the primary interest at this point, but rather the area around the rSIL. Both images on the left of Fig. 60 show the rSIL creation with XeF_2 and those on the right with the iodine-based chemistry. The two top LSM images are focused on the background and thereby the structure around the rSIL. Distortions in these images indicate a change in surface topology and transparency. The two bottom images are focused on the surface of the sample. These images can show a change in reflectivity due to a rough and damaged surface. In conclusion it can be said that the absence of spontaneous etching, when using the iodine-based chemistry, had a positive effect on the area surrounding the rSIL, just as expected. The image in the top right of Fig. 60 is free from distortions even close to the rSIL. The structure in the background shows no influence from the rSIL. Also the reflectivity just outside the FIB created rSIL, seen in the bottom right of Fig. 60, is unaltered. Both of these images prove that using the iodine-based chemistry for chemistry-assisted rSIL creation is a good choice, better than XeF_2 for the purpose of this work, which showed strong distortions and a roughened surface around the rSIL (top and bottom left of Fig. 60). Just as importantly, it has to be mentioned that an rSIL created with the iodine-based chemistry was easier to bring close to the desired shape, compared to one created with XeF_2. An attempt of an rSIL created with XeF_2 was presented earlier in Fig. 55 and Fig. 56.

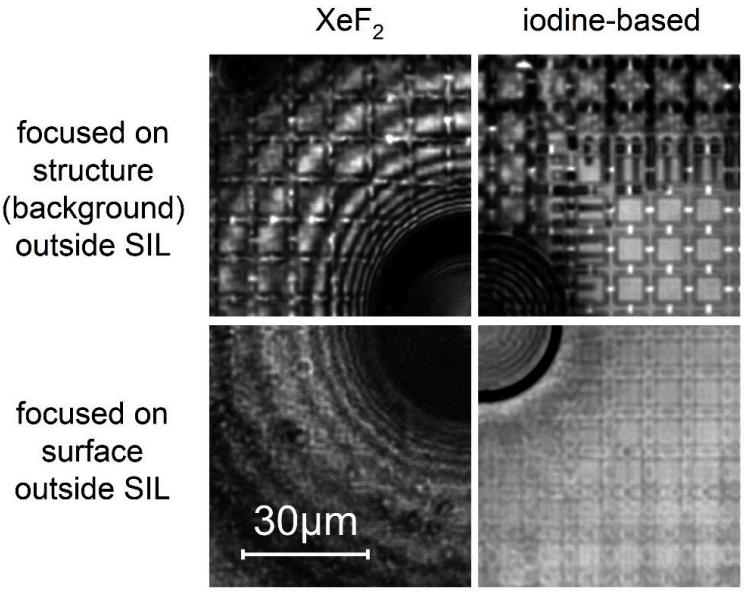

Fig. 60: The two main etch chemistries of the OptiFIB system (XeF_2 and an iodine-based chemistry) were taken into account for SIL creation. In all four LSM images the area around the SIL was analysed to show the global effect of each chemistry. The two top images are focused on the background to show the influence on transparency and surface topography. The two lower images are focused on the surface of the sample to analyse the change in reflectance and surface roughness. XeF_2 showed to be too aggressive for this application. It severely damaged the area around the SIL, which the iodine-based chemistry did not, and furthermore its etching behaviour was even harder to characterise.

The code used to program the bitmaps for the rSIL creation in a single-step chemistry-assisted FIB process can be found in 7.3 along with detailed bitmap parameters. Most important for this method is the exponent in the initial sphere formula previously shown in equation (62) and for better reference again in (64). The height of this virtual sphere is the main parameter adjusted for the bitmaps of the unassisted FIB milling in chapter 5.1 (63). This is due to the behaviour of the milling process. The main advantage of using the exponent (65) instead of the height of the sphere formula as a parameter is that the whole range of dwell times can be used. This gives the ability to adjust the rSIL shape more accurately

and to create an rSIL shape with steeper curvature, resulting in a larger opening angle. The FIB bitmaps used during this process and the thereby created rSIL shapes are presented in chapter 5.2 starting on page 127.

$$a^2 = x^2 + y^2 + z^2 \tag{64}$$

$$z_{5.2} = (a^2 - x^2 - y^2) \text{ ^ } s_{5.2} \tag{65}$$

x, y, z : Cartesian coordinates of the model of the sphere

a : value corresponding to the radius of the sphere

$z_{5.2}$: z values used to calculate the greyscale values for the rSILs of chapter 5.2

$s_{5.2}$: scaling factors used to calculate the z values for the rSILs

4.4 Designing application-specific bitmaps for FIB control

The program code for the FIB bitmaps, used for each type of SIL created by FIB in this work, is presented and explained in the Appendix. It can be used in Octave and MATLAB. The common elements of each set of code are the base coordinates and the base matrix. The base coordinates are two square matrices. In the case of the “x”-matrix, it is created by multiplying an “nxy” long column of ones with a row going from 0 to 1 in “nxy” steps. Every element of the resulting matrix is then reduced by 0.5 and multiplied by 2 in order to achieve the final matrix “x”. The “y”-matrix is created similarly, except that rows and columns are swapped.

```
%------------------- create base coordinates --------------------
nxy = 512; % amount of pixels in x- and y-direction

% x-coordinate (nxy equal rows going from -1 to 1 in nxy steps)
x = (([0:1:nxy-1]*0+1)'*([0:1:nxy-1]/(nxy-1))-0.5)*2;
% y-coordinate (nxy equal columns going from -1 to 1 in nxy steps)
y = (([0:1:nxy-1]/(nxy-1))'*([0:1:nxy-1]*0+1)-0.5)*2;
```

Both base coordinates are then used to create the base matrix, in which the value of every element is its distance to the centre. These values are

in case of the rSIL created by unassisted FIB milling (Appendix 7.2) programmed to be between 0 and 362 pixels ($\sqrt{2} \cdot 256$). The code of the rSILs created in a chemistry-assisted FIB process (Appendix 7.3) uses universal distances without units between 0 and $\sqrt{2}$. The base matrix for the dSIL (Appendix 7.4) is in units of µm, since the entire dSIL design is wavelength-dependent. The general code is Octave and MATLAB compatible and was supported by the author's colleague Clemens Helfmeier.

4.5 Custom sample holder for the development of FIB SILs

In order to apply the fundamentals of theory and hardware from the previous chapters, a custom-made sample holder system (Fig. 61, Fig. 62) was needed. It had to be suitable for efficient and reliable sample preparation and analysis during the entire development of the FIB created SILs.

Fig. 61: Custom-made sample holder for SIL sample preparation and analysis with an already polished sample.

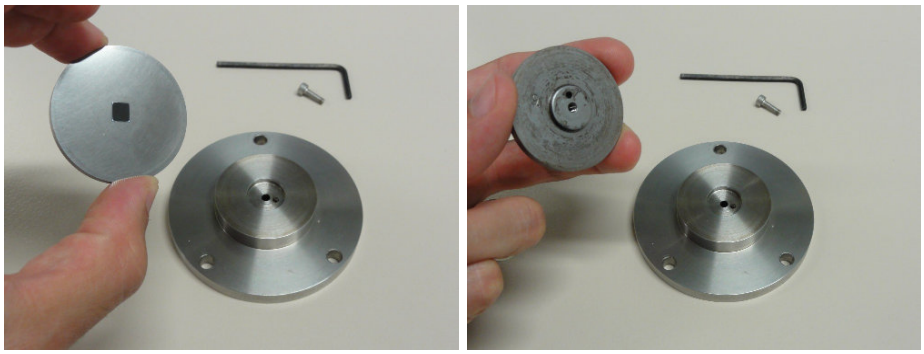

Fig. 62: Top and base part of custom-made sample holder with polished sample. Some residue from polishing chemicals remains underneath top part.

The individual operations performed on the sample throughout this work include thinning and polishing, creation of the SIL with the FIB (Fig. 63), analysis of the surface with the AFM (Fig. 64, Fig. 65) and analysis of the optical properties with the LSM (Fig. 66).

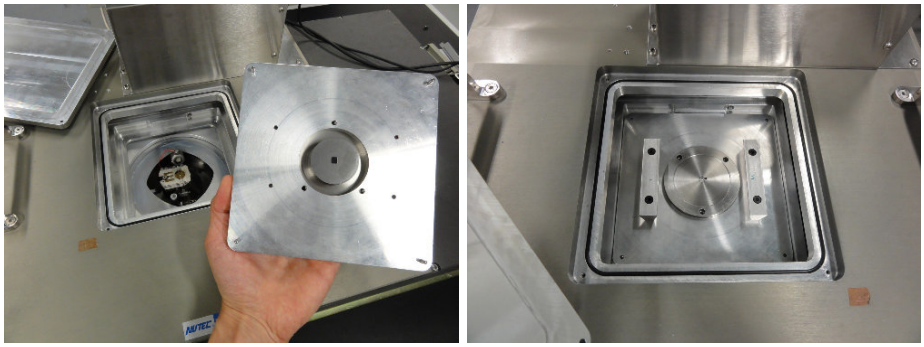

Fig. 63: Inserting custom SIL sample holder into OptiFIB using custom FIB frame.

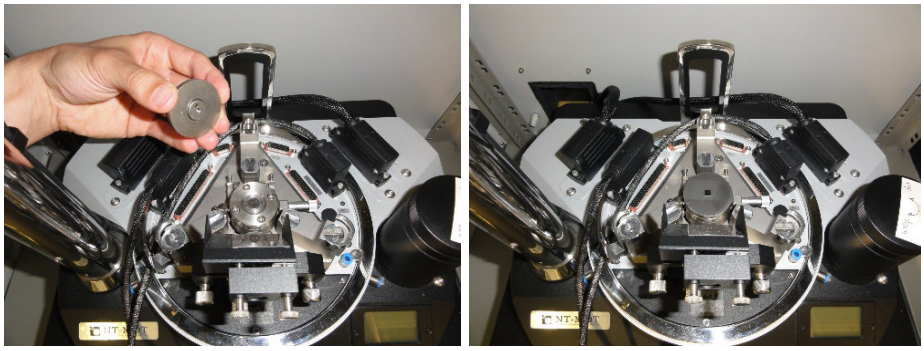

Fig. 64: Top part of custom-made sample holder, which is made to fit into “NTEGRA Aura” AFM. Magnetic material was chosen to have the sample holder connect reliably with the magnet situated in the centre of the AFM sample support.

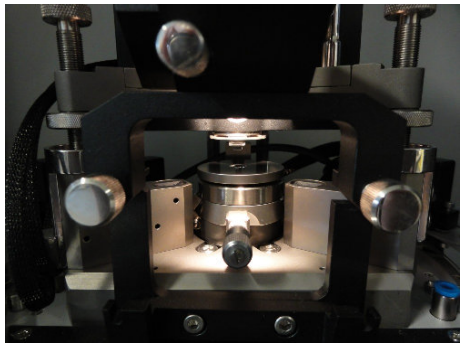

Fig. 65: Custom-made SIL sample holder inside “NTEGRA Aura” AFM ready for scanning.

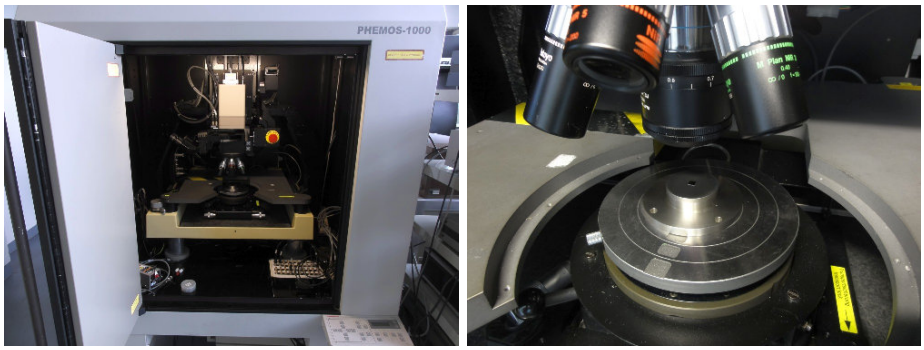

Fig. 66: Using custom SIL sample holder during LSM analysis in the Phemos1000.

The main advantage of the custom SIL sample holder is the ability to have a fixed support for the sample throughout the entire development process.

This reduces unwanted modifications of the sample while stripping it from and reattaching it to a carrier. Furthermore it enables the user to easily handle even extremely thin samples. The repolishing of a sample as presented in chapter 5.1.8 (Flexible FIB SIL – removing FIB SILs by polishing) is also possible. To achieve the best coplanarity among two polishing steps, the sample holder should not be removed from its base part (as done in Fig. 62). A set of base parts and numerous sample holders were built with the assistance of the workshop at TUB. Thereby the custom-made SIL sample holder system was able to serve as logistical basis for the experiments of this work.

5 Methods for refractive and diffractive FIB created SILs

5.1 rSIL creation by unassisted FIB milling

5.1.1 Basic concept of unassisted FIB milled rSILs

During the analysis of FIB milling behaviour (see 4.2) it was found, that ion beam milling alone can create working refractive solid immersion lens shapes of small dimensions. One specific design of an rSIL 32 µm wide, 1.4 µm thick and with a radius of curvature of 95 µm is being introduced, demonstrated and discussed in this chapter.

The process is illustrated in Fig. 67 to Fig. 70. It mostly consists of the first main step shaping the lens using only ion beam milling and the previously mentioned bitmap (4.1, 7.2), which can be seen on the right of Fig. 68. Since the ion beam implants gallium and damages the upper layer of the silicon surface [62], [63], this amorphous layer needs to be removed by a short flush with the iodine-based chemistry and a low ion beam dose at 400 ns dwell time (Fig. 69). A theoretical shape of the FIB milled rSIL can be seen in Fig. 70, along with an approximated shape of the sidewalls really achieved (dotted line in Fig. 70). In practice, the sidewalls do not have a significant optical influence, even though they are close to the lens shape. This can be explained by the relatively shallow depths of this rSIL and the fact that the real sidewalls are slightly tapered. The rSIL presented in this chapter 5.1 will be referred to as “rSIL created by unassisted FIB

milling" or "FIB milled rSIL" throughout this work, even though the last short cleaning requires chemistry assistance. This terminology is chosen to clearly differentiate between this and the "rSIL created in a single chemistry-assisted FIB process" of chapter 5.2, also called "FIB etched rSIL".

Fig. 67: Initially polished silicon surface before FIB milled rSIL creation.

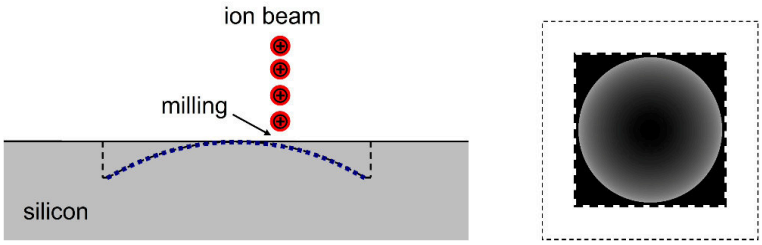

Fig. 68: First step of FIB milled rSIL creation – shaping the lens (with bitmap used for ion beam control).

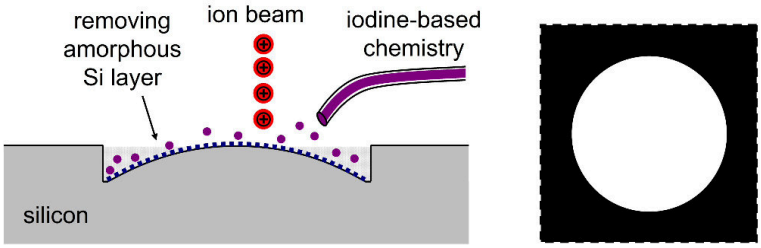

Fig. 69: Second step of FIB milled rSIL creation – cleaning the lens (with bitmap used for ion beam control). Bright greyscale values were increased for illustrating purposes.

Fig. 70: Ideal lens shape after FIB milled rSIL creation. Dotted line indicates sidewalls achieved in reality. The sidewalls did not show significant influence due to shallow depth and tapered shape.

5.1.2 Analysis of lens shape using FIB cross section

A cross section was cut through the centre of the lens shape with the FIB, in order to analyse the shape of the rSIL created by unassisted FIB milling. This method is commonly used in a FIB machine to retrieve topology and subsurface information from a sample. The surface was covered with platinum to protect the initial lens surface from damage during the cross sectioning process. Furthermore the platinum layer contrasts well with silicon. Fig. 71 shows a cross section of such a FIB created rSIL at an angle of 52° in a scanning electron microscope. The bulk silicon and the deposited metal can be well distinguished from one another. Two main parameters can also be measured in this image: the height *h* and the radius *R* (or half width) of the rSIL. The reader should not be confused by the radius *R* of the rSIL and the next introduced radius of curvature *r*. Both were chosen to be labelled “radius”, because it is the best way to describe the spherical shape and also the radial dimension of the rSIL when looking at it top down.

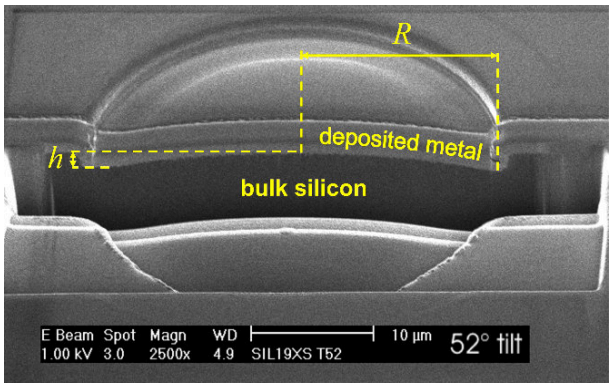

Fig. 71: Scanning electron image of a cross sectioned FIB milled rSIL at an angle of 52°. Image was taken in a FEI XL830 DualBeam. The lens surface underneath the protecting metal layer is shown, as well as height and radius of the rSIL.

Knowing the height *h* and the radius *R* (or half width) of the rSIL enables the calculation of a possible radius of curvature *r* of the spherical refractive lens shape, which is based on the Pythagorean Theorem (see Fig. 72 and (66)). It has to be kept in mind, that the vertical dimensions in the image of the cross section need to be scaled according to the viewing angle (multiplied by 2 at 30° and by 1.27 at 52°). Height *h* and radius *R* of the rSIL need to be measured accurately, because the error in calculating *r* is determined by twice the error in *h* plus twice the error in *R*. Given the fine details of the images used for the upcoming graphical analysis (Fig. 73, Fig. 74), it can be expected that the error in *R* is negligible compared to that in *h*. The precision of the AFM measurement of the next chapter leads to both parameters having a similar influence, but also becoming less erroneous than during the graphical analysis.

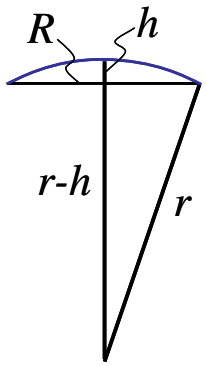

Fig. 72: Calculating the radius of curvature *r* of a spherical cap from its height *h* and radius *R* (or half width) using the Pythagorean Theorem.

$$r^2 = R^2 + (r - h)^2$$
$$r = (R^2 + h^2) / 2h \quad (66)$$

h : height of the rSIL [µm]
R : radius of the rSIL [µm]
r : radius of curvature of the rSIL [µm]

At first a graphical approach was taken to illustrate and verify a consistent radius of curvature over the whole lens surface. A circle with the previously calculated radius (Fig. 71, Fig. 72, (66)) was virtually tilted (= scaled in height according to the viewing angle, divided by 2 for 30° and by 1.27 for 52°) and superimposed on the image of a FIB cross section (Fig. 73 at 30° tilt). A more detailed measurement of this method was done by looking at the FIB cross section in a scanning electron microscope (SEM) (Fig. 74 at 52° tilt). In both cases it can be seen, that the lens surface is in good agreement with the ideal spherical shape.

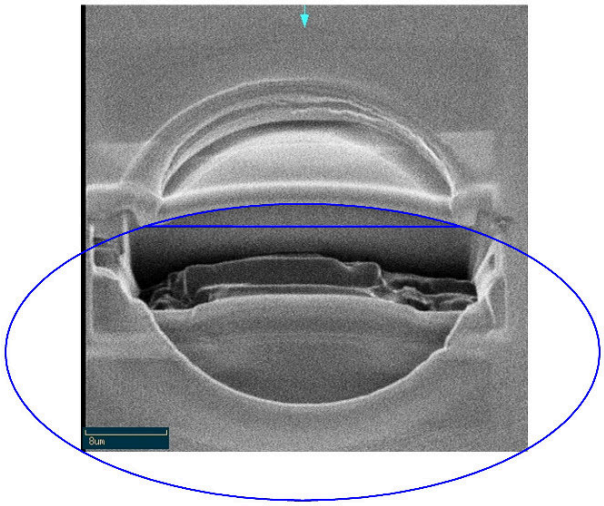

Fig. 73: Graphically comparing an ideal spherical shape to the refractive SIL shape (created by unassisted ion beam milling) shows a good agreement. The sample is tilted by 30° in this secondary electron FIB image. The circle representing the ideal shape is also virtually tilted by 30° by dividing its height in half and then superimposed on the FIB image. The line width corresponds to a vertical dimension of about 360 nm. A more precise graphical analysis can be seen in the next figure.

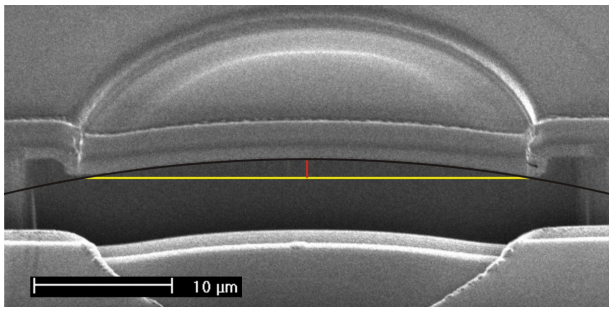

Fig. 74: More detailed analysis (introduced in Fig. 73) of the refractive lens shape using a SEM and a tilt angle of 52° (part of Fig. 71). The dimensions of this rSIL are also illustrated: Height 1.4 µm (red) and width 32 µm (yellow). These are used to calculate the 95 µm radius of the circle (black), which closely and consistently matches the lens shape. The line width used in this image corresponds to a vertical dimension of about 140 nm, giving enough precision for a graphical analysis.

5.1.3 Non-destructive lens analysis – Hardware used: AFM

Apart from the graphical analysis described in 5.1.2, the FIB created lens shapes were also analysed with an atomic force microscope (AFM) or scanning force microscope. The basic principle of AFM is illustrated in Fig. 75. The FIB cross section of 5.1.2 was chosen for a first analysis, because it is common to FIB users and relatively efficient. In contrast to the FIB cross section, the AFM is non-destructive, three-dimensional and more precise: The resolution of the AFM in z-direction is far better than that of a FIB or SEM image showing a full lens shape. On the other hand, precise AFM scans can also be very time-consuming. Nonetheless, the AFM topology analysis was used as a standard procedure for all SIL shapes presented from here on.

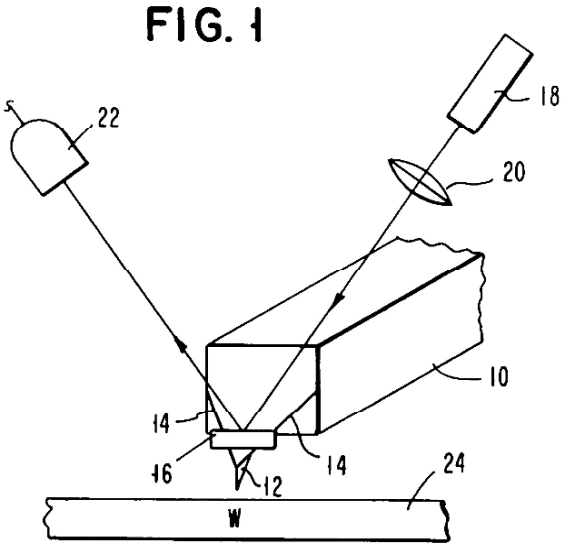

Fig. 75: Scheme of an AFM from the patent “Atomic Force Microscope” (US RE37299) [64]. The surface of a sample “24” is scanned by a tip “12”, which is attached to a cantilever “16”. The displacement of the tip, proportional to the topology of the sample, is measured by a laser beam “18” reflected from the cantilever to a sensor “22”. The sensor is commonly a four-segmented photo-diode.

The AFM systems used in these experiments were at first a “Nano-R” tool from Pacific Nanotechnologies and later an “NTEGRA Aura” from NT-MDT. The “NTEGRA Aura” can be seen in Fig. 76 and Fig. 77. It can scan an area of up to 100 µm x 100 µm and a maximum height of about 10 µm. The data of the scanned surface is collected in a 256 x 256 matrix. The author recommends the very helpful and nicely illustrated website of the manufacturer for detailed information on AFM principles and basics [65], [66]. A thorough review of AFM can be found in [67].

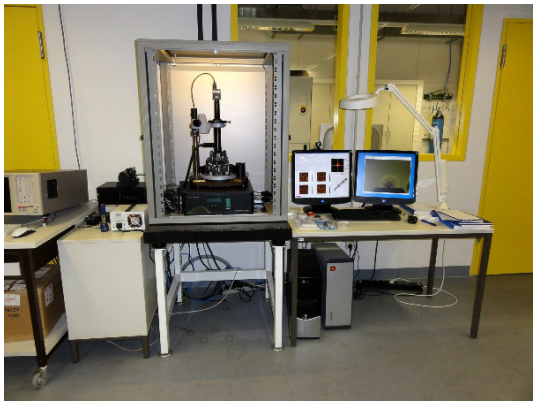

Fig. 76: The “NTEGRA Aura” AFM system from NT-MDT at TUB.

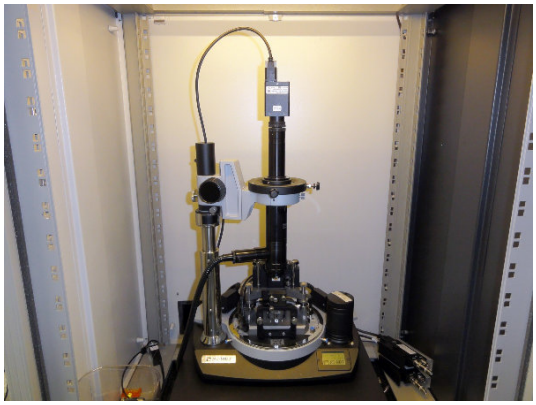

Fig. 77: Base unit, scanning head and optical microscope of the “NTEGRA Aura” AFM system.

5.1.4 Analysis of AFM data

The first AFM scans of rSILs created by unassisted FIB milling were done with a “Nano-R” tool from Pacific Nanotechnologies (now part of Agilent Technologies) with the support of the Department of Physics at TUB before the author had access to the “NTEGRA Aura" AFM system introduced in 5.1.3 on-site. These scans also consist of 256 by 256 values. Fig. 78 shows a 3D topography image of the AFM data from the rSIL discussed in this chapter. A small ring around the lens from the cleaning step can be observed as well as the general spherical shape. Closer analysis of the surface showed a roughness below 10 nm, suitable for optical application. A vertical and a horizontal profile of the lens can be seen in Fig. 79 and Fig. 80 along with the GUI of the AFM software “SPM Cockpit”. The profiles indicate the circular symmetry of the lens and confirm the parameters previously measured in “Analysis of lens shape using FIB cross section”.

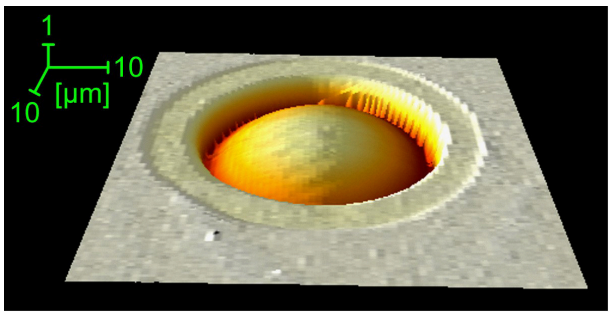

Fig. 78: 3D topography image of AFM scan from rSIL created by unassisted FIB milling. The circular cleaning step after the milling is visible around the SIL.

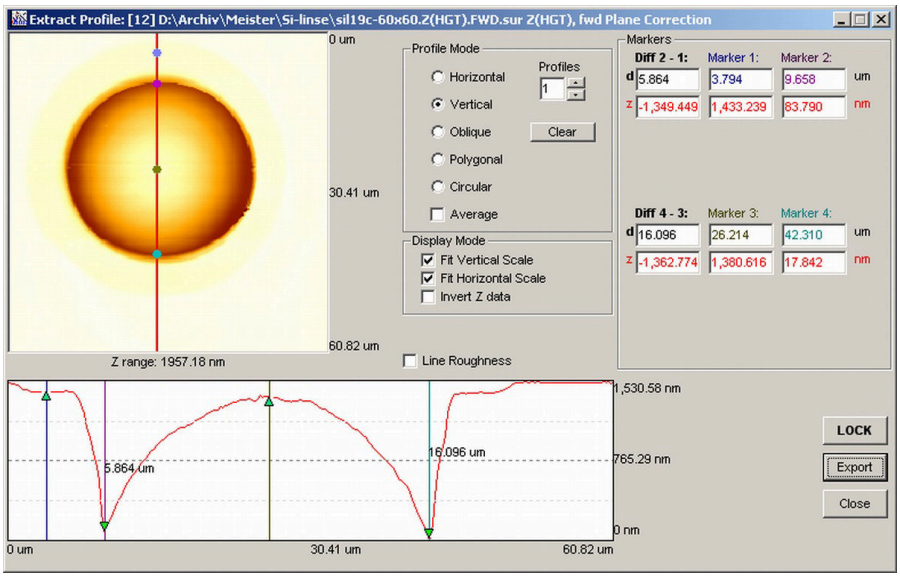

Fig. 79: Vertical profile of AFM scan from FIB milled rSIL.

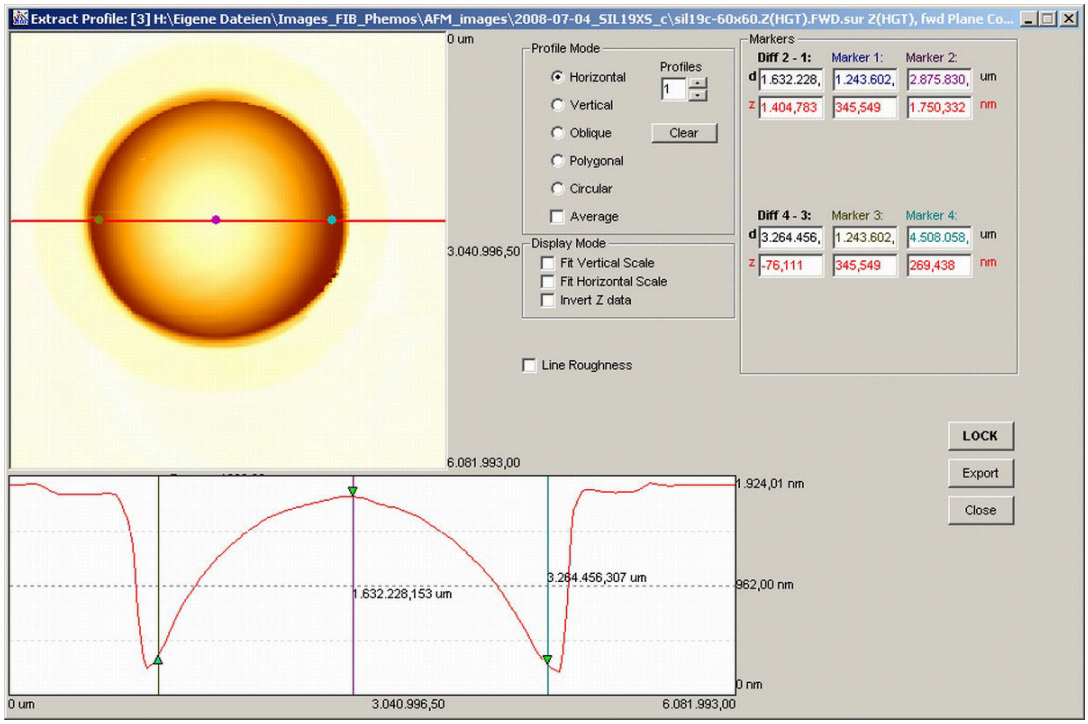

Fig. 80: Horizontal profile of AFM scan from FIB milled rSIL.

The data of the horizontal AFM profile from the FIB milled rSIL (Fig. 80) is used to compare the lens surface to an ideal spherical shape with a radius

of curvature of about 95 µm as previously calculated in chapter 5.1.2. Fig. 81 shows both shapes and Fig. 82 the vertical difference between them. This is not necessarily the way the light travels through the lens. Towards the edge of the lens, the path of light is actually shorter than the vertical difference analysed in Fig. 82. The vertical deviation is below ±50 nm for the most part. Using an infrared wavelength for imaging through silicon with $\lambda > 1$ µm leads to the fact that the deviation is below $\lambda/4$ even when taking the shortened wavelength inside silicon into account. The wavelength is divided by the index of refraction, which is 3.504 if $\lambda = 1300$ nm and 3.551 if $\lambda = 1064$ nm [68] for the two lasers used in the LSM in this work (see 2.9). Therefore the wavelength inside silicon is 371 nm or 300 nm, respectively. This proves that the small rSIL shape created by unassisted FIB milling is of good optical quality.

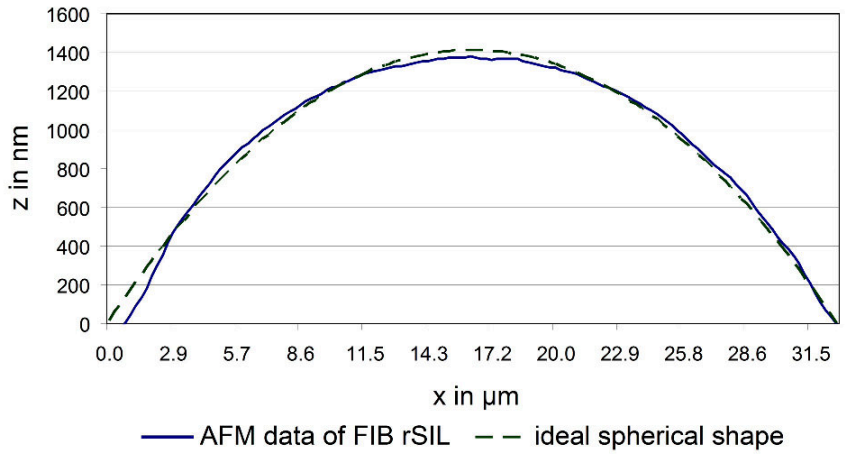

Fig. 81: Comparing horizontal profile of AFM scan from FIB milled rSIL to an ideal spherical shape. The data from the measurement is manually fitted to a semi-circle with a radius of curvature of about 95 µm.

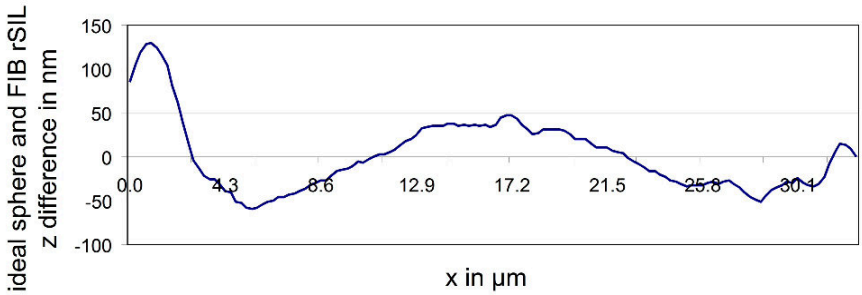

Fig. 82: Difference between ideal spherical shape (radius of curvature about 95 µm) and horizontal profile of AFM scan from FIB milled rSIL. Stronger deviation on the left is partially due to the scanning direction of the AFM.

All of the following AFM measurements were done with an “NTEGRA Aura" system. It uses the same basic principles as the “Nano-R”, but offers a larger amount of flexibility in terms of modifications on the tool and sample placement. The sample holder system introduced in 4.5 takes advantage of the latter. The 3D-illustration of an AFM scan from a SIL taken with an “NTEGRA Aura" can be seen in Fig. 83. This SIL was created with the same FIB recipe as the one in Fig. 78 through Fig. 82.

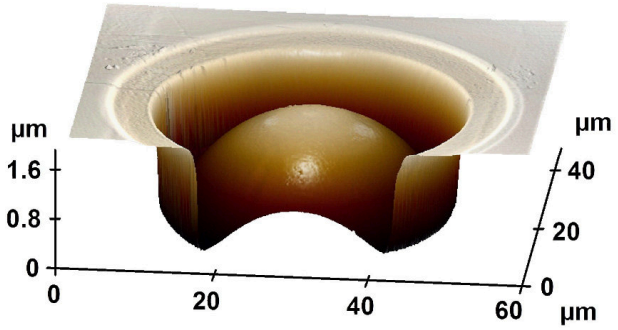

Fig. 83: 3D illustration of AFM scan taken with “NTEGRA Aura” from an rSIL created by unassisted FIB milling. This measurement also showed the spherical shape and the previously mentioned dimensions. The circular cleaning step removing the amorphous layer from FIB milling is again visible around the SIL.

5.1.5 Improvement of optical imaging through silicon using the rSIL created by unassisted FIB milling

Since shape and surface properties of the rSIL created by unassisted FIB milling met the requirements of an optically working lens, the next step was to create this rSIL on test patterns to analyse its optical effects. In this chapter two different types of patterns were used to get a first impression of the optical benefit of this rSIL: a fill shape pattern and a resolution test pattern. The latter was introduced in chapter 2.9 on page 45. The fill shape pattern consists of a grid of approximately 1 µm wide elements with 1 µm space in between (see [69] for details on fill shape design). The milled rSIL was created on a 55 µm thick sample and examined with the confocal laser scanning microscope (LSM) of the Phemos 1000 using a 1300 nm wavelength and a 0.5 NA objective. Fig. 84 shows the corresponding LSM images without and with rSIL. The first things noticed in the image with the rSIL are the visible field of view (FOV) throughout the entire width of the lens, the magnified structure underneath the rSIL and the increased contrast. The additional magnification and improvement in resolution are discussed in detail in chapter 5.1.9. The change in contrast underneath the rSIL is analysed by the intensity values along a line scan as shown in Fig. 85 through Fig. 87.

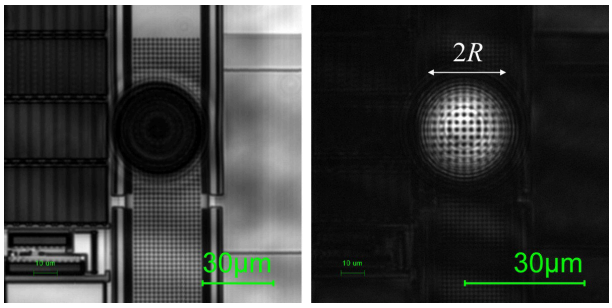

Fig. 84: Optical analysis of rSIL created by unassisted FIB milling. The diameter (2*R*) of the rSIL is about 32 µm. The pattern recurring reliably underneath the SIL is a grid of metal fill shapes of 1 µm pitch. It was used to determine the SIL's optical benefit. The scale on this and the following images is adjusted according to the magnification of the lens.

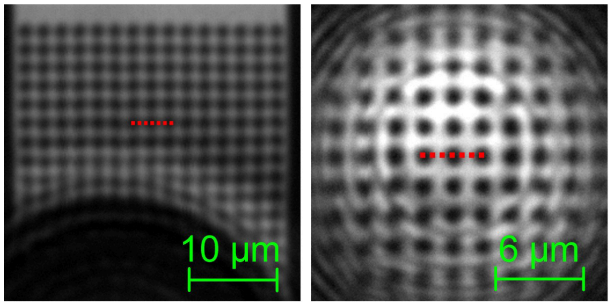

Fig. 85: Detail from LSM image without and with FIB created rSIL. Dotted line shows position of a line scan, which is displayed in detail in Fig. 86 and analysed in Fig. 87.

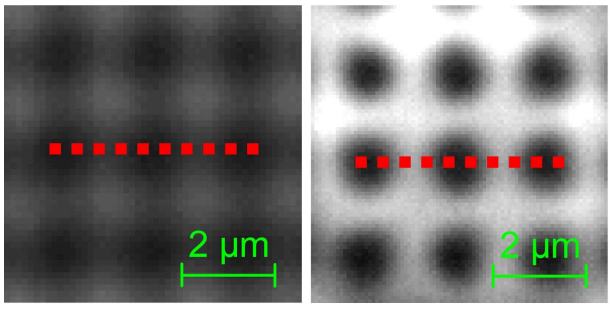

Fig. 86: Close up of the same area without (left) and with (right) FIB created rSIL. Images are brought to the same scale for better comparison. Intensity values along the dotted line were being analysed in Fig. 87.

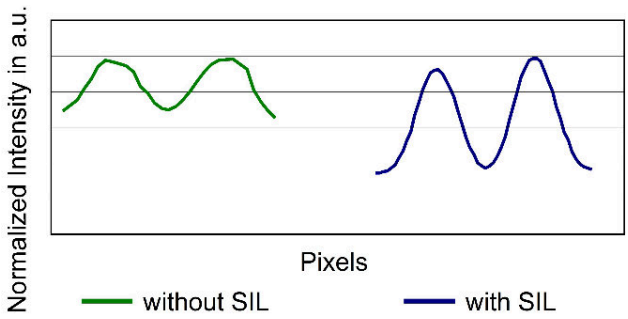

Fig. 87: Intensity values measured along the dotted lines in Fig. 85 and Fig. 86. The image with FIB created rSIL shows a steeper gradient between dark and bright areas, indicating an improvement in image quality and resolution.

Both images without and with rSIL (Fig. 84 - Fig. 87) were taken with the regular automated settings of the LSM. No additional editing was applied. The reflected intensity values without rSIL turned out to have a maximum 15 % higher than with rSIL (normalised for better comparison in Fig. 87), which can be explained by the relatively small opening angle of this rSIL. However, the overall range between minimum and maximum was about twice as large with rSIL, creating a steeper gradient between the dark and bright areas. This indicates an improvement in resolution, which is also demonstrated in the next paragraph. The contrast was improved by an average factor of 1.7, calculated from the data presented in Fig. 87 and according to [25] p. 551.

Next part in the optical testing of the rSILs created by unassisted FIB milling was the application on resolution test patterns. The samples in use were “Azuma Optical Probe Test Chips” introduced in chapter 2.9 on page 45 and supplied to the author by DCG Systems. They consist of various test structures including defined resolution test charts with bar targets. Such a target can be seen in Fig. 88 from the backside of the chip through 35 µm of bulk silicon.

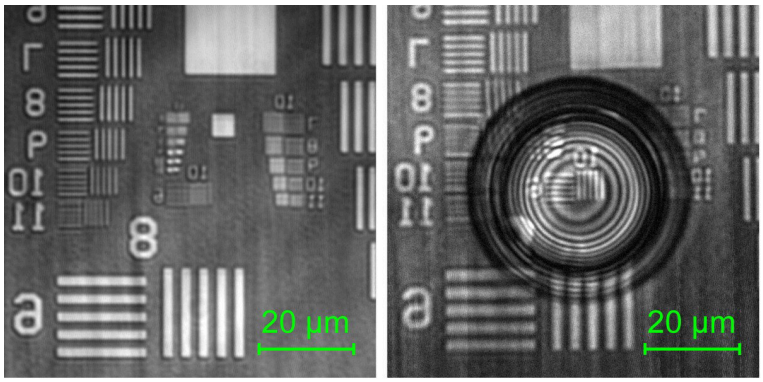

Fig. 88: Testing the rSIL created with unassisted FIB milling for improvement in image resolution. The maximum resolution with a 100x 0.5 NA objective, at laser wavelength of 1064 nm and a sample thickness of roughly 35 µm is about 1200 nm. It is shown that the pattern “10-6” in the centre of the LSM image with a pitch value of 980 nm is well resolved with the rSIL, but not without. Both scales correspond to the regular size of the structures. The one on the right does not take the magnification inside the rSIL into account.

The left image of Fig. 88 is without rSIL and the one on the right shows a milled rSIL placed over pattern “10-6”. The LSM can resolve around a 1200 nm pitch size in this set-up without SIL, corresponding to a size between pattern “9-10” and “9-11”. Pattern “10-6” with a pitch size of 980 nm is clearly resolved with the rSIL, using a 1064 nm laser wavelength and a 0.5 NA objective. To further test the resolution limit, this FIB milled rSIL was created on a 60 µm thick sample with the same resolution test chart (Fig. 89).

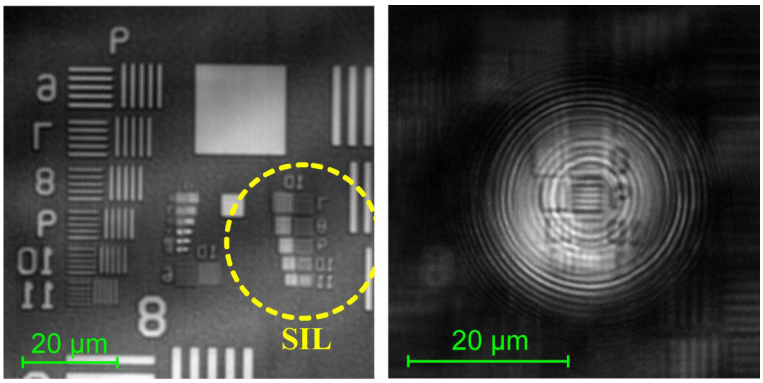

Fig. 89: LSM images (100x 0.5 NA objective, 1064 nm laser wavelength, 60 µm sample thickness) without and with FIB created rSIL. The pattern “10-9” is resolved with the rSIL and has a pitch value of 690 nm, showing an improvement in resolution of about 1.8x. The scale of the right image is adjusted according to the magnification of the lens.

While maintaining the same LSM set-up as in Fig. 88, the rSIL is able to resolve pattern “10-9” with a pitch value of 690 nm, indicating an improvement in resolution by a factor of 1.8. In this case the factor of improvement in resolution is equal to the additional magnification of the lens. This fact and the general behaviour of additional magnification and improvement in resolution with the FIB milled rSIL is analysed and explained in the chapters 5.1.8 and 5.1.9. Chapter 5.1.9 also shows why a sample thickness of approximately 60 µm is the ideal condition for the milled rSIL. Overall, the experiments on resolution test patterns could prove that the use of the rSIL created by unassisted FIB milling has a significant optical benefit, despite its relatively small dimensions. This was expected from the analysis of the intensity profiles in the beginning of this chapter.

5.1.6 Using FIB created rSIL for emission analysis of active devices

Since the experiments of 5.1.5 demonstrated an improvement in resolution despite the small dimensions of the rSIL, the experiments of this chapter

also show the use of the FIB milled rSIL on an active device for emission analysis.

The 1064 nm laser, which was utilised in some of the experiments in chapter 5.1.5, was an optional system feature and had limited availability at the Phemos tool at TUB. The standard 1300 nm wavelength has a slight influence on the achievable resolution: Using the Rayleigh criterion in equation (29), along with the two wavelengths and the corresponding refractive indices for lightly doped silicon [68], shows that the theoretical resolution changes by about 20 % when using the 1300 nm laser instead of the higher resolving 1064 nm. On the other hand, the absorption coefficient, and thereby the inverse penetration depth, improves by a factor of about 10^5 (again based on [68]). Therefore, the standard laser with 1300 nm wavelength was used in the experiments of chapter 5.1.9 and thereafter.

The FIB milled rSIL was created on a series of transistors forming a ring oscillator. Examining the milled rSIL through 77 µm of sample thickness, at 1300 nm wavelength and with a 0.5 NA objective showed an additional magnification of 2.4x (Fig. 90). More importantly, fine details of the image could also be resolved. The wells of the individual devices could be clearly distinguished. The lines in between had a width of 240 nm, according to CAD layout data. It can however not be assumed, that the resolution increased in these dimensions, since the opening angle of the rSIL on this sample thickness is relatively small. The LSM can resolve a pitch size down to about 1550 nm in this set-up (see Fig. 33 on page 49). Even if the resolution did improve by the factor of additional magnification, which would contradict to the fact that resolution depends on the opening angle, a pitch size of 650 nm corresponding to a line width of only 325 nm could be resolved. The visibility of these spacers can therefore only be explained by a strong change in reflectivity among the differently doped materials.

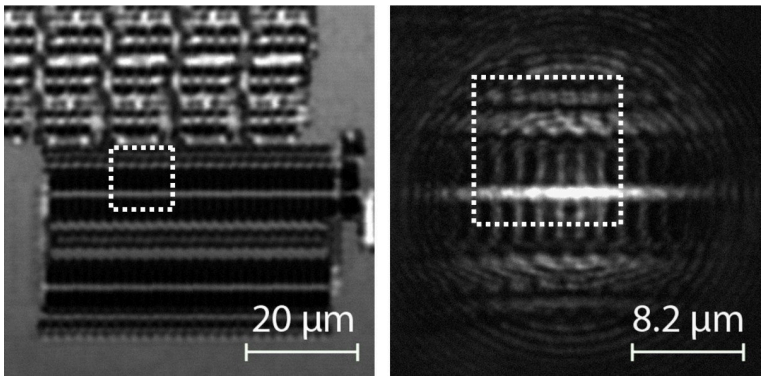

Fig. 90: Using the rSIL created by unassisted FIB milling on an active device – a ring oscillator. The wells of the individual devices can be clearly distinguished with rSIL on the right. The LSM images were taken with a 1300 nm laser and a 0.5 NA objective. In the next figure an emission analysis is performed on the same area of the device, without and with rSIL as marked by the dotted rectangle. Sample thickness was about 77 µm and additional magnification 2.4x.

The device of Fig. 90 was not only examined in a reflective laser image, but also by photon emission analysis (PEM) [6]. In this analysis, the Hamamatsu C4880-79 cooled silicon CCD camera of the Phemos 1000 captured the emission signal of the device. The device had to be turned on during the measurement, with the ring oscillator running and the MOSFETs continuously switching, to create an emission. The area marked by the white dashed rectangle in Fig. 90 was looked at closely in the emission image of Fig. 91. A remarkable difference without and with FIB milled rSIL is the ability to distinguish between the individual devices just like in the reflected laser image. Arrows in the right image of Fig. 91 point out the separating spaces.

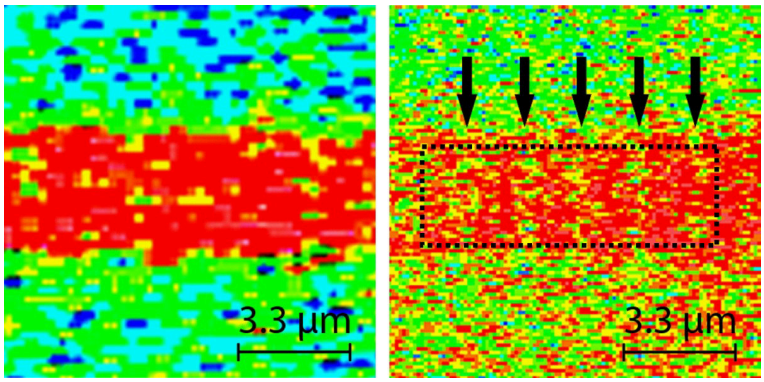

Fig. 91: An emission analysis is performed on an operating ring oscillator in the area marked in Fig. 90 without (left) and with (right) the unassisted FIB created rSIL. In the emission image the individual devices can be distinguished with rSIL, just like in the LSM image. The spaces of lower emission between the devices are marked by arrows. A series of horizontal line scans is performed in the black dotted rectangle and analysed in Fig. 92.

A series of 25 horizontal line scans was measured in detail to further quantify the result of the emission analysis with FIB milled rSIL. The region of these lines is marked by the black dotted rectangle in Fig. 91. Calculating the average of all of the intensity values from the line scans lead to the graph in Fig. 92.

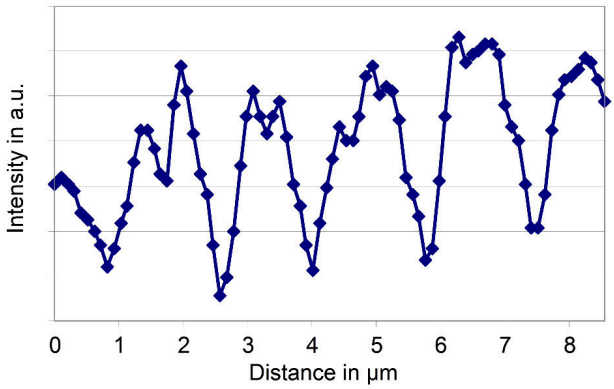

Fig. 92: Average data from 25 horizontal line scans of the emission signal in arbitrary units and as indicated in Fig. 91. The measured intensity values have a lateral spacing of about 100 nm. A reduced signal between the devices is visible, as was expected from the emission image.

The areas of reduced intensity between the devices can again be clearly identified in Fig. 92. For an improvement in the quantity of the emission signal, however, a larger SIL shape offering a larger opening angle would be needed. The latter is the motivation for the rSIL creation in a single-step chemistry-assisted FIB process of chapter 5.2. It has to be mentioned, that in terms of intensity another analysis without FIB milled rSIL, also performing a series of averaged line scans, brought out similar results. Therefore the benefit of the rSIL created by unassisted FIB milling is an improvement in resolution even without additional image editing or data averaging. The improvement depends on the sample thickness used, as shown in the images of this chapter as well as 5.1.5 and analysed in detail later in 5.1.9.

5.1.7 Applying anti-reflective coating to the FIB created rSIL using PECVD

Most of the LSM images presented so far showed aberrations from the spherical shape of the rSIL and interferences at the silicon-air-interface. One approach to this problem is presented in this chapter, which was to create an anti-reflective coating (ARC) on the surface of the rSIL (Fig. 93). This layer has a thickness depending on the wavelength it is optimized for and the refractive index of the coating material. Generally the ARC thickness is taken to be the wavelength it is optimized for, divided by the refractive index of the ARC times 4 (see (67)). The refractive index of the ARC is part of the formula, because the shortened wavelength inside the ARC has to be taken into account. One assumption used in this calculation is that most of the light hits the surface close to a vertical angle. Once this is granted, it creates a situation where the light reflected from the initial sample surface reaches the ARC-air-interface after travelling twice the ARC thickness meaning half a wavelength. This leads to destructive interference on the surface and thereby the whole purpose of the ARC,

which is to have more illumination inside the material. Under this condition a stronger reflectance from the object plane and less from the sample surface (Fig. 93), yielding better contrast in the LSM image, can be expected.

$$t_{ARC} = \lambda_{opt} / (4 \cdot n_{ARC}) \quad (67)$$

t_{ARC} : thickness of the ARC [nm]

λ_{opt} : wavelength for which the ARC is optimized (1064 nm in this case) [nm]

n_{ARC} : index of refraction of the ARC material (about 1.9 for the type of silicon nitride used in this chapter) [-]

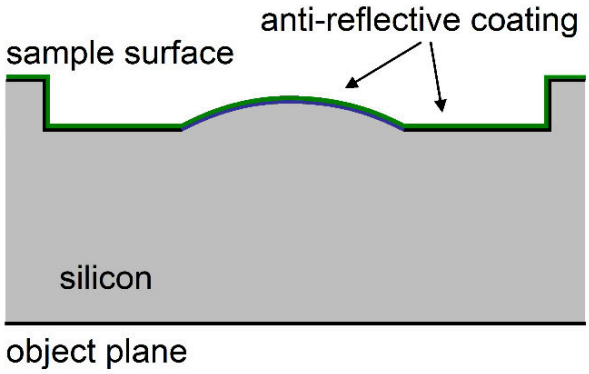

Fig. 93: Anti-reflective coating (ARC) was applied to the rSIL created by unassisted FIB milling in an additional process of plasma enhanced chemical vapour deposition (PECVD). The deposited material was silicon nitride (Si_3N_4) at a thickness of 142 nm, optimized for 1064 nm laser wavelength. The optical benefit of this coating can be seen in Fig. 94.

The ARC on the FIB milled rSIL was created outside of the FIB tool by plasma enhanced chemical vapour deposition (PECVD). It consists of silicon nitride (Si_3N_4 – exact stoichiometry unknown) which was built up to a thickness of 142 nm. The calculated thickness of the ARC would be 140 nm with a refractive index of the silicon nitride of about 1.9 in this case

and an optimization for the 1064 nm wavelength. This calculated thickness of the ARC matches the achieved thickness quite well. A limiting aspect of this presented method, which is also the reason why the ARC wasn't used in all of the presented experiments, is that the high temperature vacuum PECVD process is not suitable for every sample, especially if packaged.

The optical benefit of the FIB milled rSIL and the ARC can be seen in Fig. 94. The LSM image on the left shows few details, which could be visibly improved with the FIB milled rSIL, but were also accompanied by strong noise and aberration (image in the middle). Both of which were significantly reduced with the ARC (right image of Fig. 94).

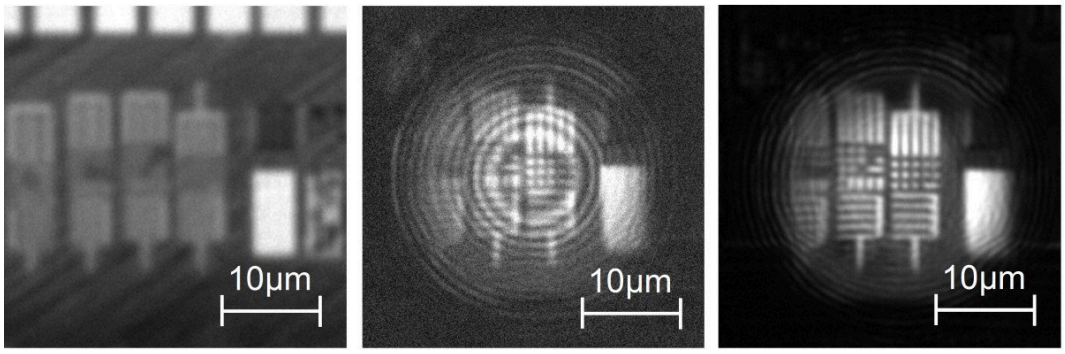

Fig. 94: LSM images taken by 1064 nm laser wavelength and a 0.5 NA objective without FIB milled rSIL (left), with milled rSIL (middle) and with milled rSIL including anti-reflective coating (right). The ARC showed to have a significant positive influence on the contrast and the aberrations of the image. The scale was adjusted to the additional magnification of the rSIL.

The intensity values of the reflected signal were measured to analyse the effect of the ARC in detail: Three line scans were performed over the same image feature from Fig. 94, as illustrated in Fig. 95. The thereby gathered data is shown in Fig. 96.

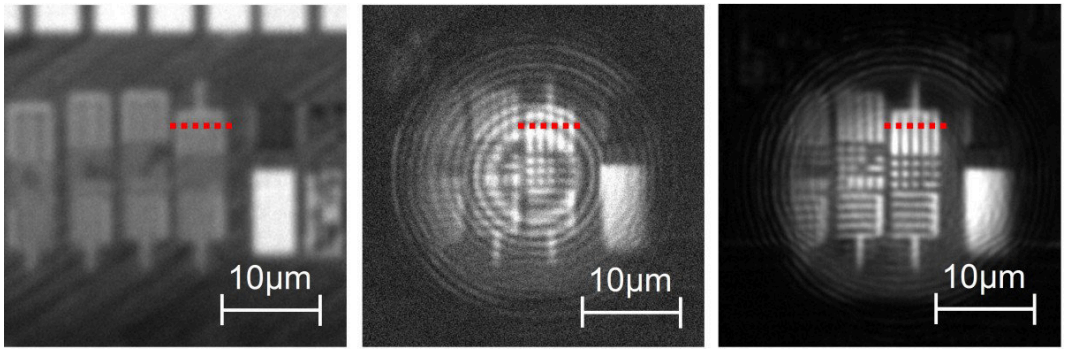

Fig. 95: Three line scans were performed on the same image feature previously shown in Fig. 94. The intensity values along the dotted lines were analysed without SIL (left), with milled rSIL (middle) and with milled rSIL including ARC (right). The results are plotted in Fig. 96.

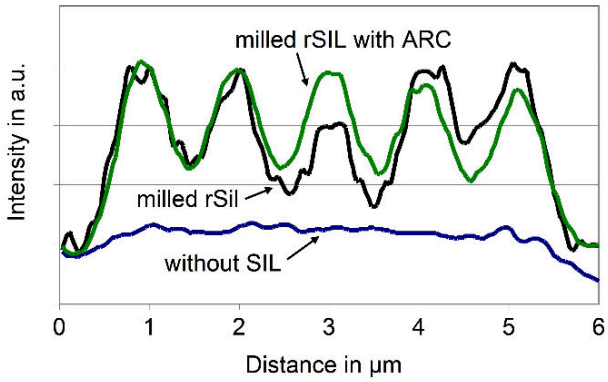

Fig. 96: Intensity values of the scans illustrated in Fig. 95. The milled rSIL makes the structure of 1 µm pitch size clearly visible and the ARC eliminates the noise signal.

The plot of the intensity values in Fig. 96 without SIL, with milled rSIL and plus ARC shows that the 1 µm pitch structure is well resolved with the milled rSIL. Adding the ARC does not necessarily change the resolution, since it doesn't influence the geometry of the lens. It does, however, eliminate the noise signal. The latter is seen as small ripples in the curve of the intensity signal from the milled rSIL without ARC (Fig. 96). The result of the ARC is that the real structure is imaged more precisely, as illustrated by the smooth and homogenous wave pattern with ARC in Fig. 96. This

proves that the use of an ARC on the FIB milled rSIL leads to an improvement in image quality by reducing aberrations and noise.

Another attempt was made to create a double-layer ARC out of tantalum pentoxide and silicon dioxide (Ta_2O_5 and SiO_2), which did however not show results as good as the single-layer ARC. Furthermore it should be mentioned that the coating did not always have a positive effect as obvious as the one presented in Fig. 94. The next logical step, since the SIL is created inside a FIB tool, would be to also create the ARC as part of the FIB rSIL process. Depositing a silicon dioxide ARC inside the FIB is common for FIB trenching [70]. So far, the application of this method was not successful, possibly due to the different topology of the rSIL compared to the mostly flat FIB trench. Therefore, in summary it can be said that the silicon nitride ARC created outside of the FIB tool by PECVD is currently the best solution, if it can be applied to the sample despite its high temperature vacuum process.

5.1.8 Flexible FIB SIL – removing FIB SILs by polishing

Two main aspects motivated the series of experiments called “Flexible FIB SIL” presented in this chapter. The first was to show that even though the FIB created SIL is changing the surface of the sample, it does not need to be a permanent change. It can be “undone” by polishing away a few micrometers of the material. The second aspect was to determine the influence of the sample thickness on the additional magnification of the rSIL and most importantly on the improvement in resolution as analysed in chapter 5.1.9 (“Increased resolution and additional magnification with a constant lens shape, depending on sample thickness”).

The term “flexible” relates to the fact that the FIB milled rSIL is created, removed and then recreated on the same sample. The recipe and thereby the shape of the rSIL remained the same throughout the experiments. The

shape and curvature was kept constant to reliably identify the influence of the sample thickness. Furthermore, adjusting the curvature of the FIB milled rSIL with every step in sample thickness would have been very complex due to the non-linear FIB process.

The custom-made sample holder system presented in chapter 4.5 was used to prepare a set of samples including optical test structures. These samples where then used for FIB milled rSIL creation as illustrated in Fig. 97. Next was a polishing step to recreate the initial sample surface on a slightly thinner sample (Fig. 98). The sample thereby regained its original surface quality, verified in the LSM (Fig. 98, Fig. 100). The creation of the FIB milled SIL was thereby carried out three times (Fig. 97, Fig. 99, Fig. 101) on every single sample.

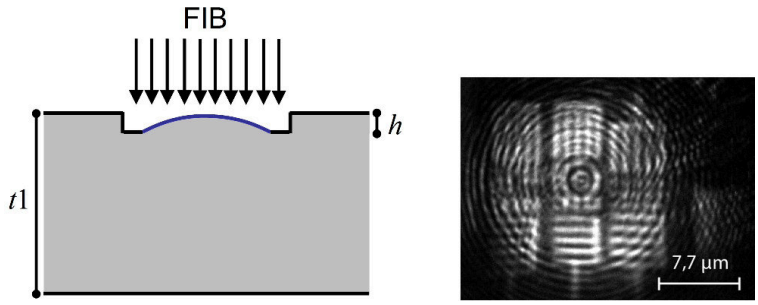

Fig. 97: Verifying the influence of the sample thickness on the optical performance of the FIB created rSIL. First step with relatively thick sample created an LSM image (right) with large magnification. Shape and curvature of rSIL are kept constant throughout these experiments to make the sample thickness the only varying parameter.

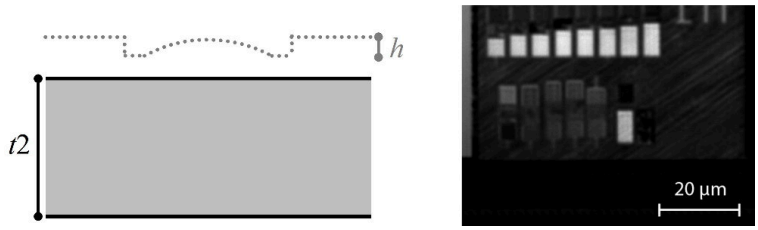

Fig. 98: Polishing away a few micrometers recreated the initial blank surface on a thinner sample now with thickness $t2$. LSM image on the right shows sample without SIL on the exact same spot as Fig. 97.

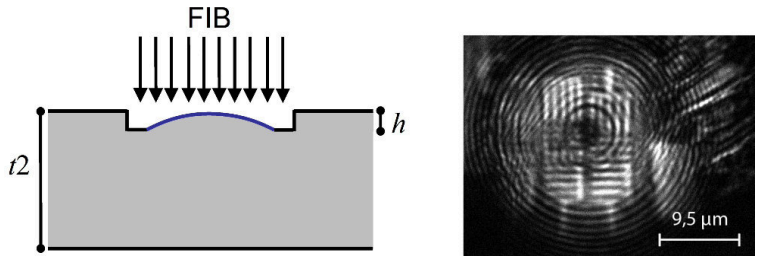

Fig. 99: Creating another rSIL of the same shape on the same spot to analyse the influence of the sample thickness. LSM image on the right shows lower magnification and fewer aberrations.

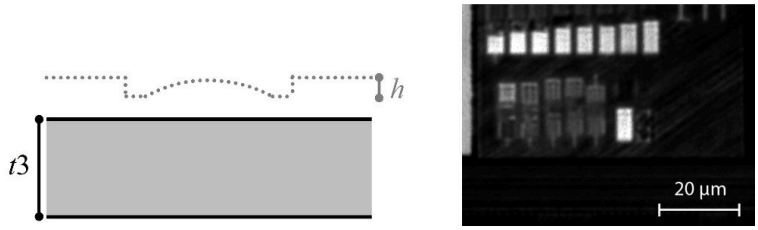

Fig. 100: Sample was polished a second time, just like in Fig. 98. This step again recreated the initial unaltered sample surface.

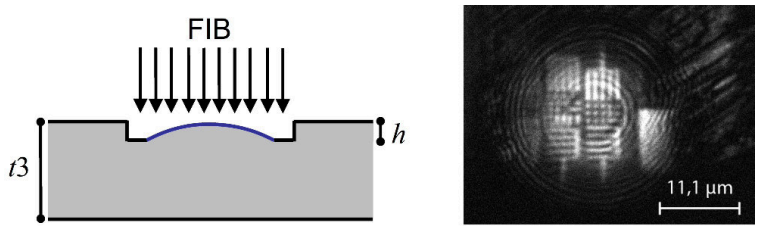

Fig. 101: Creating the FIB rSIL a third time on an even thinner sample, again at exactly the same spot. The LSM image shows the lowest magnification, but also the fewest aberrations among the three presented images with decreasing sample thickness (Fig. 97, Fig. 99 and Fig. 101).

The sample thickness after every polishing step was recorded. Furthermore LSM images were taken with and without rSILs from which the additional magnification was measured. Though the magnification is not necessarily a criterion for image quality or resolution, it was chosen as a parameter since it can be well measured and helped the author to better understand the behaviour of the rSIL. The measured values of additional magnification related to the sample thickness are presented in chapter 5.1.9 along with a discussion on possible improvement in resolution.

5.1.9 Increased resolution and additional magnification with a constant lens shape, depending on sample thickness

The sample thickness has a significant influence on the imaging properties of the consistent rSIL shape created by unassisted FIB milling, as it is explained by the optical theory in this chapter. Accordingly, a series of experiments with LSM images was presented in chapter 5.1.8. Values of additional magnification were measured during these experiments along with the corresponding sample thicknesses. They are being analysed in this chapter for a better understanding of the ideal set-up of the milled rSIL. Furthermore the possible improvement in resolution, which is the overall goal, is being discussed.

The additional magnification can be calculated using the imaging properties of a sphere described by the first order lens formula (68) [25]. These are adapted to the conditions of the FIB created rSIL and illustrated in Fig. 102. In this simplified analysis the opening angle is not taken into account, but it will be later on, when the possible improvement in resolution is discussed (Fig. 108). The opening angle has a significant influence on resolution (see equation (29)). For the FIB created rSILs, additional magnification is not necessarily equivalent to the improvement in resolution. This is due to the fact that the FIB created rSILs are only the cap of a hemisphere and not a full hemisphere, because an efficient process, which can be realized with the FIB is needed. The additional magnification is used as a first parameter to analyse the rSILs.

The main variables for calculating the additional or transverse magnification are the sample thickness t, the radius of curvature r and the index of refraction inside and outside the rSIL. The thickness t is expected to be equal to the distance between the top of the rSIL and the point **A** on the object plane (see Fig. 102). The radius of curvature is the consistent distance between the surface of the rSIL and the centre of curvature **B**. The index of refraction outside the rSIL is the one of air (=1) and inside it is taken to be around 3.5, since the rSIL is created out of silicon and used in the infrared wavelength range. With these parameters it is possible to calculate the transverse magnification (69) or additional magnification achievable with the FIB created rSIL. The first order lens formula needs to be solved for the image distance (70) and then inserted into the previous formula to lead to an equation of the additional magnification in relation to the sample thickness (71). While doing so, it needs to be kept in mind, that the object distance is equal to the sample thickness and that the radius of curvature is negative by definition, because the lens curves around the object. The latter is already taken into account in equation (71). The absolute value of the radius of curvature needs to be used for the

calculation of the additional magnification. This sign convention is dealt with differently in the German DIN, but leads to the same results. Since one main reference used in this work is “Optics” by Hecht [25], the author chose to also apply the sign convention presented in that book.

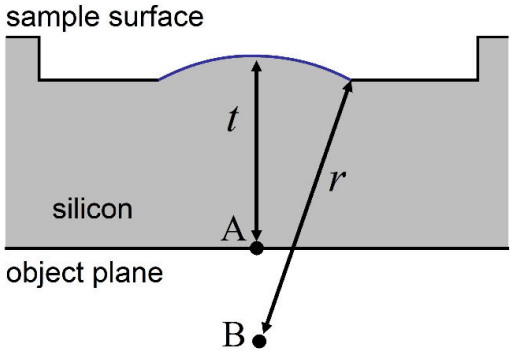

Fig. 102: Parameters and set-up used to calculate the additional magnification of the FIB created rSIL for a sample thickness smaller than the radius of curvature of the rSIL.

$$n_1 / s_o + n_2 / s_i = (n_2 - n_1) / r \quad (68)$$

$$M_T = - (n_1 \cdot s_i) / (n_2 \cdot s_o) \quad (69)$$

$$s_i = n_2 / ((n_2 - n_1) / r - n_1 / s_o) \quad (70)$$

$$M_T = r \cdot n_1 / (r \cdot n_1 - t \cdot (n_1 - n_2)) \quad (71)$$

n_1 : index of refraction in object space (3.5 in this case)

n_2 : index of refraction in image space (1 in this case)

s_o : object distance (= sample thickness t in this case)

s_i : image distance

r : radius of curvature (negative in this case)

M_T : transverse magnification

All of the presented experiments and also the just introduced calculations use a set-up of the FIB milled rSIL with a sample thickness smaller than the radius of curvature of the thereby hemispherical or central rSIL. An aplanatic rSIL with a sample thickness larger than the radius of curvature

(by a factor of 1+1/n [17]) could not be achieved, because it requires a larger opening angle of the rSIL and offers less tolerance in terms of proper sample thickness versus radius of curvature.

Plotting the values of the additional magnification over the sample thickness leads to Fig. 103. The radius of curvature of the FIB milled rSIL of about 95 µm is used in this calculation. It can be noticed that for a sample thickness reaching the value of the radius of curvature, the magnification is equal to the index of refraction of the rSIL material (3.5 for silicon in this case). For thinner samples, the difference between sample thickness and radius of curvature increases and thereby the additional magnification decreases. On the contrary this condition leads to a larger opening angle of the rSIL, which is beneficial for the improvement in resolution. This is discussed in detail later in Fig. 105 and Fig. 106.

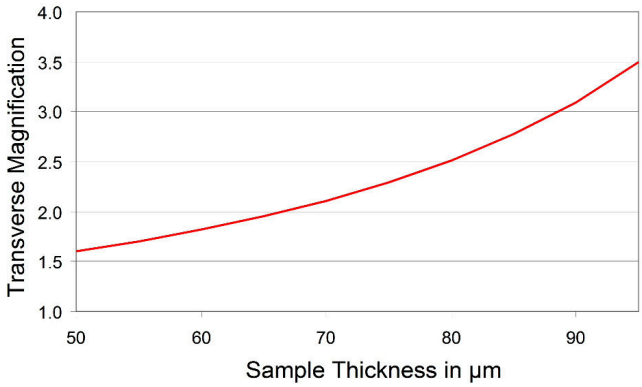

Fig. 103: Plot of theoretical dependence of additional transverse magnification of the FIB created rSIL with a radius of curvature of 95 µm on the sample thickness based on formula (71). Note that the magnification corresponds to the index of refraction (silicon = 3.5 in this case) for a sample thickness equal to the radius of curvature. This would be the ideal case of a central or hemispherical rSIL, if the rSIL can supply a large enough opening angle.

A series of magnification values for different sample thicknesses was recorded during the experiments of the “Flexible FIB SIL” in chapter 5.1.8.

In summary, 4 samples were each used for the creation of 4 milled rSILs, which were then polished 3 times. Therefore 48 rSILs were created and analysed with a 0.5 NA and a 0.7 NA objective, using 1064 nm and 1300 nm laser wavelength. This created close to 192 values of additional magnification. The different objectives and wavelengths did not have a uniform effect. This can be understood, because the opening angle did not show an influence on magnification, and the refractive index of silicon differs only by 4 % between 1064 nm and 1300 nm.

The measured values of additional magnification are plotted in Fig. 104 along with the theoretical characteristic. They deviate from theory, because of slight errors in the measurement of the sample thickness, difficulties in detecting the exact value of additional magnification and the fact that the magnification is also influenced by the chosen focal point. An increasing difference for thicker samples can be noticed. Apart from this, the average values of the measurements generally follow the theory, which proves that the presented calculations can be applied to the FIB milled rSIL.

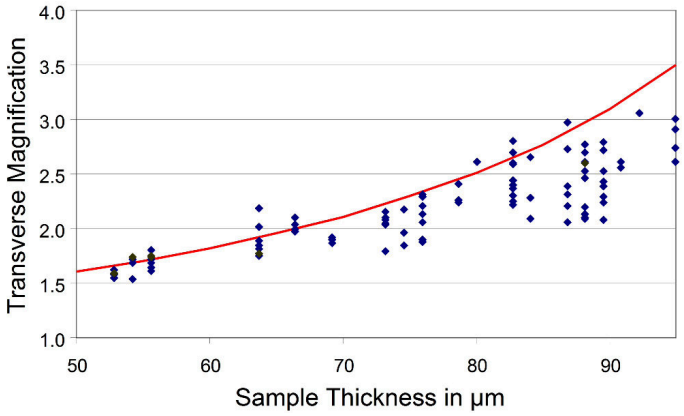

Fig. 104: Measured values of additional transverse magnification from the “flexible FIB SIL” experiments. In average, the measurements follow the tendency of the theoretical calculations presented earlier in Fig. 103 based on formula (71).

Since the additional magnification of the rSIL only increases image features, but not necessarily their resolution, the upcoming analysis deals with the possible improvement in resolution, while using the constant shape of the FIB milled rSIL. The main aspect in this analysis is the opening angle and thereby the numerical aperture (NA) of the rSIL. Two extreme conditions can be assumed, one with a sample thickness close to the radius of curvature of the rSIL (Fig. 105) and another with a sample much thinner than the radius of curvature (Fig. 106). The first would achieve a larger additional magnification, but also a smaller opening angle with the relatively small FIB milled rSIL shape. Refraction and also reflection would be zero for a sample thickness equal to the radius of curvature.

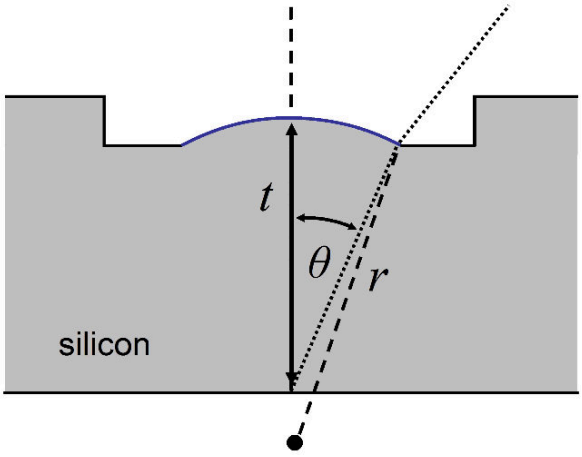

Fig. 105: Comparing the two extreme conditions for the same FIB created rSIL shape – sample thickness close to radius of curvature gives large additional magnification, but also creates a small opening angle. This theoretically reduces resolution and showed to create stronger aberrations in the LSM images, than rSILs on thinner samples. The limited dimensions of the FIB SIL cause this effect. With an unlimited SIL shape, a sample thickness equal to the radius of curvature would be ideal for a hemispheric SIL in bulk silicon.

The second leads to less additional magnification, but a larger opening angle and thereby a higher improvement in resolution, which is the

ultimate goal. It can already be seen in Fig. 106, that this improvement in resolution is restricted by the opening angle of the rSIL in air. Most obviously, total internal reflection needs to be avoided. Furthermore an opening angle larger than that of the used objective doesn't lead to an additional improvement. Both of these aspects are discussed and calculated later in Fig. 108.

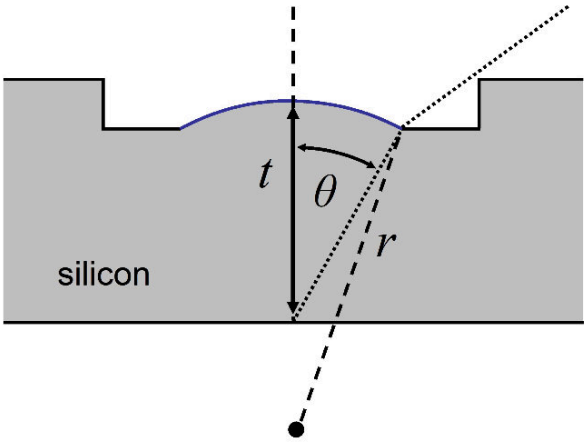

Fig. 106: Comparing the two extreme conditions for the same FIB created rSIL shape – sample thickness much smaller than radius of curvature gives a lower additional magnification, but a larger opening angle. The latter theoretically improves resolution, as long as it doesn't surpass the opening angle of the used objective. In addition LSM images in thinner samples showed to have fewer aberrations.

Resolution, as introduced earlier in chapter 2.5 and discussed for immersion microscopy in chapter 3.1, is proportional to the wavelength λ divided by the numerical aperture NA. The NA consists of the opening angle with respect to the optical axis and, as a significant factor for immersion microscopy, the index of refraction in object's space (41). In this formula, the index of refraction mathematically represents the shortened wavelength in a material of higher index, which ultimately increases the resolving power. The author defines the possible improvement in resolution as the ratio between the NA of the rSIL and the NA of the objective without SIL (73). Note that for the NA of the rSIL in silicon used at

infrared wavelength the index of refraction is 3.5 and for the objective in air it is 1. Calculating the possible improvement in resolution for the FIB milled rSIL shape on various sample thicknesses and for an objective with 0.5 NA, as it was used in all of the LSM experiments presented so far, results in the dashed curve of Fig. 107.

$$Res \propto \lambda / NA \tag{72}$$

$$NA = n \cdot \sin\theta \tag{(41))}$$

$$\eta_R = NA_{rSIL} / NA_{objective} \tag{73}$$

Res : resolution in terms of smallest resolvable pitch size [nm]

λ : wavelength used for imaging (1064 or 1300 nm in this work)

NA : numerical aperture [-]

n : index of refraction (3.5 in silicon or 1 in air) [-]

θ : (half) opening angle [°]

η_R : possible improvement in resolution when using the FIB rSIL [-]

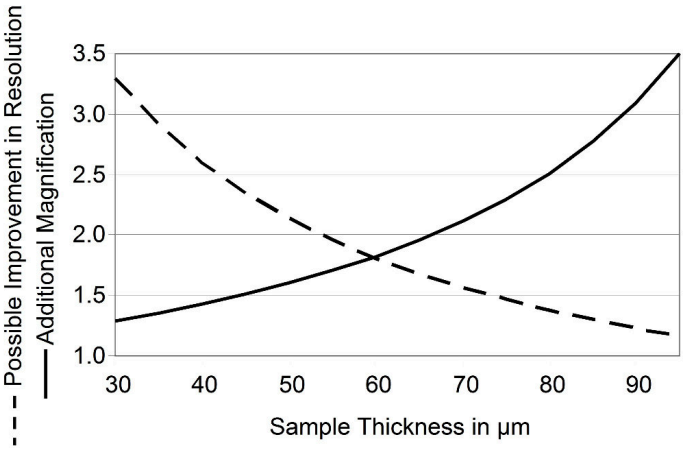

Fig. 107: Connecting additional magnification (as described in Fig. 103) and theoretically possible improvement in resolution for the constant FIB milled rSIL shape used with a 0.5 NA objective. Basic idea is illustrated in Fig. 105 and Fig. 106.

At first sight, the plot in Fig. 107 suggests that the possible improvement in resolution would continuously increase with thinner samples. This however

is not entirely the case. As mentioned earlier in connection to Fig. 106, the opening angle of the rSIL in air has a significant influence on how much of the possible improvement in resolution can actually be used. In short, the outer angle in air can of course not be larger than 90°, otherwise total internal reflection would occur. In addition, an opening angle larger than that of the used objective can also not be made full use of. A model was set up for a basic resolution analysis based on the opening angle and NA of the rSIL. The inner and outer angles on the spherical surface of the rSIL were analysed and calculated in detail, as illustrated in Fig. 108.

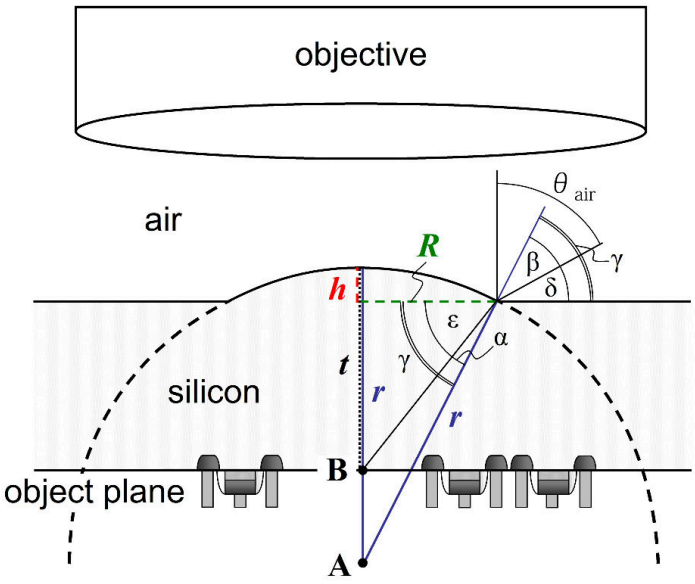

Fig. 108: Illustration of the angles inside and outside the FIB created rSIL. Main goal was to find the opening angle in air θ_{air} based on the sample thickness t, the radius of curvature r, the height h and the radius of the rSIL R for a set-up with $t < r$. Corresponding results can be seen in Fig. 109 and Fig. 110.

The following equations (74 - 79) including the parameters introduced in Fig. 108, were used to calculate the outer angle “delta” (80) as the angle above the horizontal of the outmost ray of the FIB milled rSIL shape. From this, the opening angle of the rSIL in air “theta$_{air}$” (81) was derived.

$$\gamma = \tan^{-1}((r - h) / R) \quad (74)$$

$$\varepsilon = \tan^{-1}((t - h) / R) \quad (75)$$

$$\alpha = \gamma - \varepsilon \quad (76)$$

$$n_{si} \cdot \sin\alpha = n_{air} \cdot \sin\beta \quad (77)$$

$$\beta = \sin^{-1}((n_{si} / n_{air}) \cdot \sin\alpha) \quad (78)$$

$$\delta = \gamma - \beta \quad (79)$$

$$\delta = \tan^{-1}((r - h) / R) - \sin^{-1}[(n_{si} / n_{air}) \cdot \sin(\tan^{-1}((r - h) / R) - \tan^{-1}((t - h) / R))] \quad (80)$$

$$\theta_{air} = 90° - \delta \quad (81)$$

α, β, γ, δ, ε, θ_{air} : see Fig. 108

r : radius of curvature of the rSIL

t : sample thickness

h : height of the rSIL

R : radius of the rSIL

The influence of the sample thickness on each of the inner and outer angles can be seen in Fig. 109. The shape of the rSIL is constant for this calculation (r = 95 µm, h = 1.4 µm, R = 16 µm). “delta” needs to be larger than 0° to avoid a condition similar to total internal reflection. In practice it needs to be even larger to overcome the outer wall of the rSIL (which was not analysed in detail in this calculation). The opening angle of the rSIL in air “$theta_{air}$”, which should match that of the objective used, is also determined based on “delta” and in relation to the sample thickness (Fig. 110).

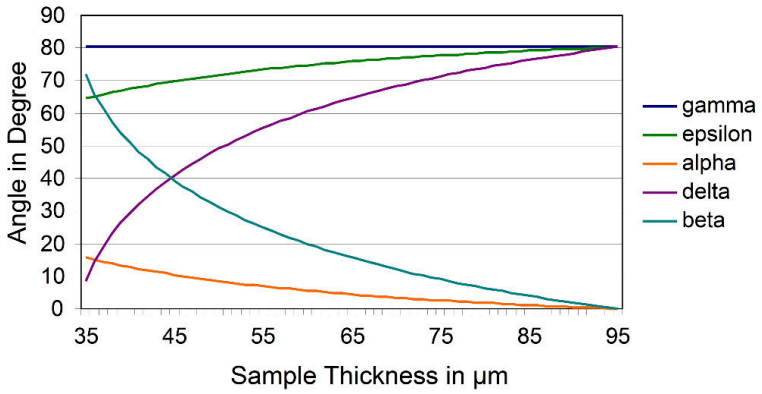

Fig. 109: Results from the calculation of the angles inside and outside the FIB created rSIL of constant shape.

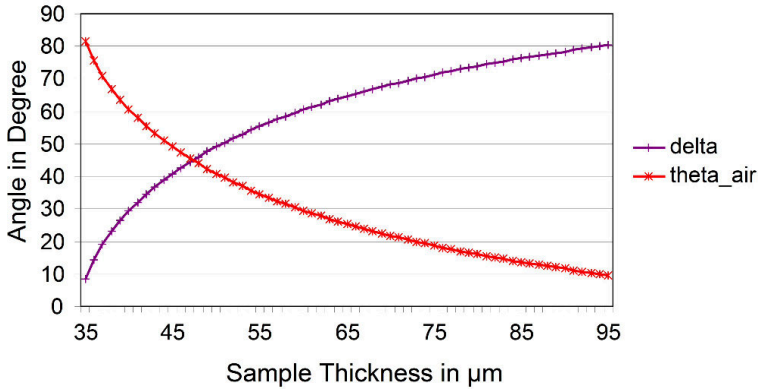

Fig. 110: The outside angles “delta” and “$theta_{air}$” (see Fig. 108) of the presented rSIL shape (r = 95 µm, h = 1.4 µm, R = 16 µm) created by unassisted FIB milling.

“$theta_{air}$” should be larger than the opening angle of the objective in use to take full advantage of the resolving power of the objective. For example, an objective with a numerical aperture of 0.5 has (half) an opening angle of 30° and one with 0.7 has about 45°. With this data, the sample thickness offering the best compromise for the presented FIB milled rSIL shape for each objective can be determined. For 0.7 NA it should be about 47 µm and for 0.5 NA about 59 µm. This explains why the increasing “possible improvement in resolution” towards thinner samples in Fig. 107 is merely theoretical and why the experiment on a 60 µm thick sample

(Fig. 89 and in detail in Fig. 112) is the best solution for the milled rSIL shape.

To verify that a sample thickness close to the radius of curvature really isn't a better solution, the FIB milled rSIL was also created on a sample with a thickness close to the radius of curvature of 95 µm. The resulting LSM image can be seen in Fig. 111.

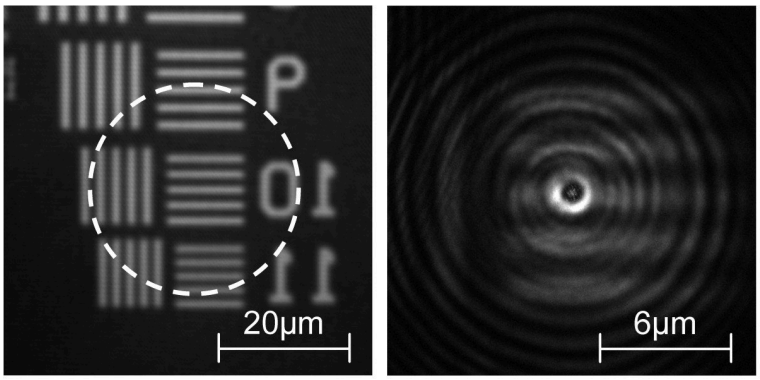

Fig. 111: Experiment of rSIL created by unassisted FIB milling with a sample thickness close to the radius of curvature of 95 µm (right). Left image shows test pattern without SIL and also where rSIL was created (dashed circle). Additional magnification is at 3.2x and thereby close to the theoretical maximum. However, the 1300 nm LSM image taken with a 100x 0.5 NA objective shows strong aberrations and very low contrast. This can be explained by the small opening angle, which the rSIL offers at this sample thickness.

A 1300 nm wavelength was used in Fig. 111, due to the increased sample thickness and a limited availability of the 1064 nm option in the Phemos at TUB (see page 104 for 1064 nm vs. 1300 nm discussion). An additional magnification of 3.2x was observed, but also strong aberrations and low contrast, which indicate that this rSIL set-up did not lead to an improvement in resolution. The experiment with the ideal set-up for this rSIL on a 60 µm thick sample was presented earlier in Fig. 89 and can be seen in detail in Fig. 112.

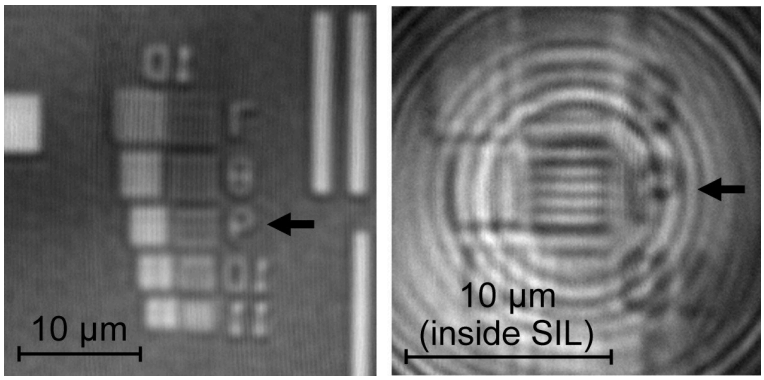

Fig. 112: Detailed results of rSIL created on 60 µm thick sample by unassisted FIB milling presented earlier in Fig. 89. This set-up shows to be a good compromise between additional magnification and opening angle as discussed in Fig. 107 and calculated in Fig. 110. In this 1064 nm LSM image the pattern with 690 nm pitch (arrow) is resolved using the FIB rSIL on the right. Thereby the resolution is improved by a factor of 1.8, equal to the additional magnification in this case.

The set-up used in Fig. 112 showed to be the ideal compromise between additional magnification and improvement in resolution for the small FIB milled rSIL shape. The LSM can resolve down to about 1200 nm pitch size without rSIL at 1064 nm laser wavelength and with a 0.5 NA objective (see Fig. 32 on page 48). With the milled rSIL a pitch size of 690 nm is resolved. The resolution is therefore improved by a factor of 1.8x, which is equal to the additional magnification for this particular set-up. This condition also proves the theory presented in Fig. 107, connecting additional magnification and possible improvement in resolution. It furthermore shows, that the best results achievable with the milled rSIL shape may have been reached, and that a larger SIL is needed for further improvement. This is the motivation for the rSIL creation in a single-step chemistry-assisted FIB process presented in the upcoming chapter 5.2.

5.2 rSIL creation in a single-step chemistry-assisted FIB process

The opening angle and the corresponding numerical aperture are the key aspects of the resolving power of a lens. The previously presented rSIL created by unassisted FIB milling already showed to bring an improvement in resolution (5.1.5 and 5.1.9) and some benefit for emission analysis (5.1.6), despite its small dimensions (32 µm width and about 95 µm radius of curvature). Larger lens shapes could so far not be successfully realized due to the limited machining capabilities of the unassisted FIB milling. One main problem of unassisted FIB milling was the redeposition of material [55] resulting in a saturation of the milling process (discussed in chapter 4.3 on page 78). This limited the ability to create steep angles of curvature and large SIL shapes in a reasonable processing time. The use of an assisting chemistry for rSIL creation (see Fig. 113) addresses this problem and also offers an improved etch rate, resulting in a larger SIL shape with a wider opening angle. In order to make full use of this opening angle, a significant outer gap becomes more important than for the smaller rSIL shape of chapter 5.1. Therefore a new geometry parameter needs to be taken into account. Fig. 114 illustrates this outer radius of the rSIL.

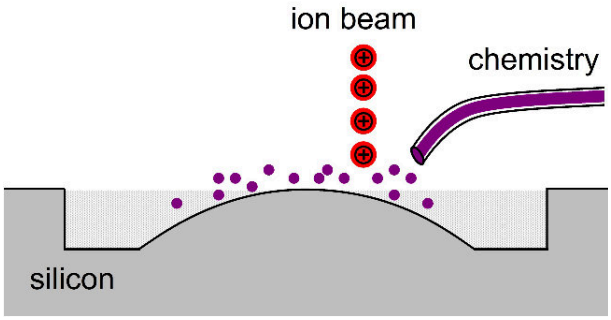

Fig. 113: Creating an rSIL in a single chemistry-assisted FIB processing step. The added chemistry offers the removal of a larger amount of material, but also has a more complex process characteristic.

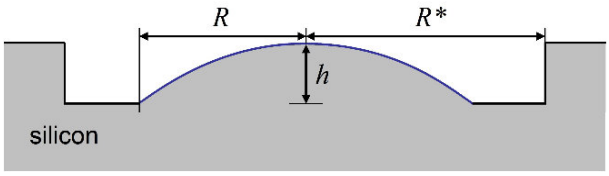

Fig. 114: Basic parameters of the rSIL created with chemistry assistance. Due to the larger shape, a significant outer gap is now more important than for the smaller rSIL created by unassisted FIB milling in chapter 5.1. The resulting rSIL shape is designed to have a height h of about 5 µm and a radius of curvature of 65 µm. The outer radius R^* needs to be 30 µm at a radius of the rSIL R of 25 µm, in order to avoid light being reflected or blocked by the sidewalls.

Comparing the rSIL shape created by unassisted FIB milling in chapter 5.1 and the one created with chemistry-assisted FIB etching in this chapter shows the increased potential of the "etched rSIL" (see Fig. 115). The parameters of the milled and the etched rSIL are listed in Tab. 1. The rSIL shape presented in this chapter is designed to have a height of about 5 µm, with a radius of curvature of 65 µm, a radius of the rSIL (or half width) of 25 µm and an outer radius of 30 µm. Twice the outer radius is equal to the width of the FIB box used during the process. Assuming, just for comparison, the use of both rSIL designs in a central rSIL set-up with a radius of curvature equal to the sample thickness (which is not necessarily the ideal case, as discussed in 5.1.9) results in an opening angle against the optical axis of 22.6° for the etched design and of 9.7° for the milled design. Therefore the etched rSIL design offers an opening angle more than twice as large. Furthermore it covers 2.5 times the area of the milled rSIL design.

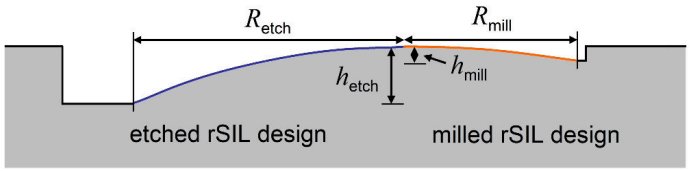

Fig. 115: Detailed comparison of the rSIL created by unassisted FIB milling in chapter 5.1 ("milled rSIL design") and the rSIL created by a single chemistry-assisted FIB process in this chapter ("etched rSIL design"). The increased lens area and the smaller curvature of the etched design lead to a larger opening angle, offering a higher potential for an improvement in resolution.

Tab. 1: Parameter listing of the "etched" rSIL design created with chemistry assistance and the "milled" rSIL design created by unassisted FIB milling, as illustrated in Fig. 115.

parameter	etched rSIL	milled rSIL
R : radius of the rSIL	25 µm	16 µm
h : height of the rSIL	5 µm	1.4 µm
r : radius of curvature	65 µm	95 µm

Since the process for the etched rSIL design needed to go deeper into the silicon material (see "height of the rSIL" in Tab. 1) and also be used on a much larger area, an efficient assisting chemistry was needed. The question of which type of FIB assisting chemistry would be the ideal choice for rSIL creation, was discussed earlier in chapter 4.3 and resulted in the iodine-based chemistry ethylene diiodide (EDI). How the etching behaviour could be influenced by the FIB bitmap was also shown in chapter 4.3 and implemented in the corresponding program code in Appendix 7.3. Based on this, some of the bitmaps from the development of the presented method can be seen in Fig. 116. Their difference is the exponent in the sphere formula (65) (page 82, chapter 4.3), which mostly influences the

gradient on the edge of the rSIL. Fig. 117 shows a numerical representation of these bitmaps, which illustrates the gradient of the greyscales and thereby the dwell times on the edge of the rSIL more clearly.

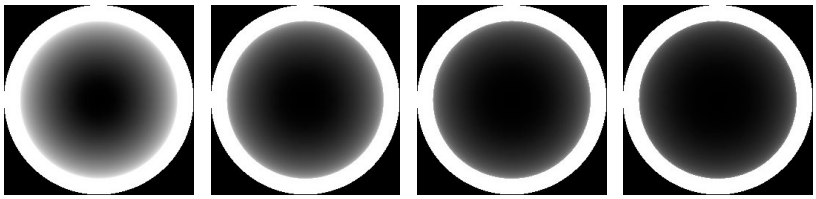

Fig. 116: Excerpt of the bitmaps used to develop the ideal rSIL shape which could be created in a single chemistry-assisted FIB process. Main difference of the bitmaps is the distribution of the greyscale values towards the edge of the rSIL, which could be controlled by the exponent of equation (65) (page 82, chapter 4.2), used to program the bitmaps. Fig. 117 illustrates the difference of these bitmaps numerically.

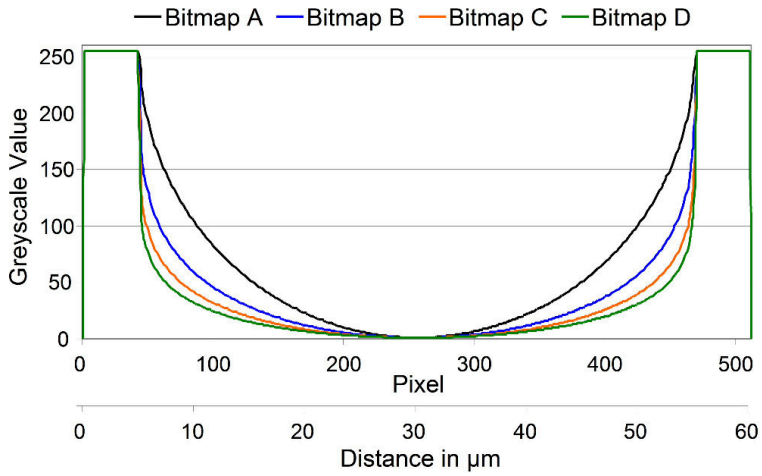

Fig. 117: Central profiles showing the greyscale values from the bitmaps shown in Fig. 116, which were used to develop the rSIL created in a single chemistry-assisted FIB process. This plot better illustrates the difference in greyscale value distribution towards the edge of the SIL.

The process of the chemistry-assisted rSIL creation with a FIB and the thereby achieved rSIL shape was optimized using the previously presented dwell time variation (equation (65), Fig. 116, Fig. 117). The resulting shape gained close proximity to an ideal spherical shape in the

centre region. Fig. 118 illustrates the data of an AFM scan, which verified that the basic design parameters of the rSIL were met. The height was about 5 µm, the inner and outer radius about 25 µm and 30 µm. Fig. 119 shows three profiles from the series of rSIL shapes created during the development of the process in relation to an ideal spherical shape. “Shape 3” matches the ideal shape in the centre region, but not over the whole lens area. Despite this noticeable deviation, an optical benefit with this shape could be proven in the LSM.

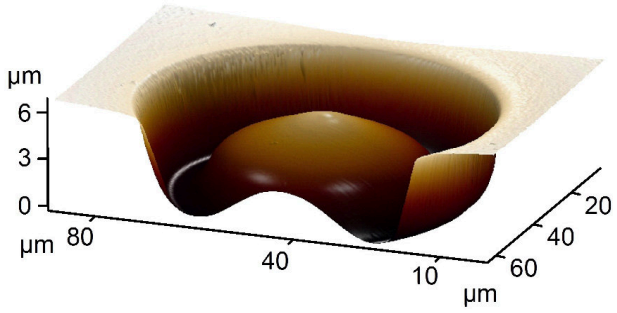

Fig. 118: Data from an AFM scan of an rSIL shape created with one of the bitmaps shown in Fig. 116 by a single chemistry-assisted FIB process in 40 minutes of processing time using an ion beam of 8 nA. The basic parameters (R, R^*, h – see Fig. 114) were reached, but a perfectly spherical shape was not achieved for the entire SIL surface (see detailed profiles in Fig. 119).

A 1300 nm wavelength and a 0.7 NA objective were used to create the LSM images in Fig. 120. The standard 1300 nm laser of the Phemos was used, because the optional 1064 nm laser wasn’t available at the time of the experiment. This had a slight influence on the resolution, but also improved the transparency of the silicon significantly (see page 104 for 1064 nm vs. 1300 nm discussion).

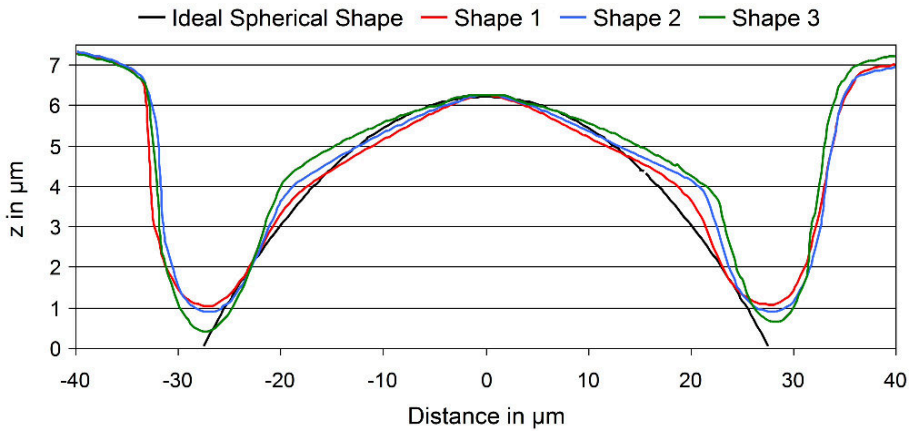

Fig. 119: Profiles of rSIL shapes created during the development of a chemistry-assisted rSIL FIB process. Shape "3" meets the ideal spherical shape in the centre region, which already showed to have a positive optical effect for LSM imaging (see Fig. 120).

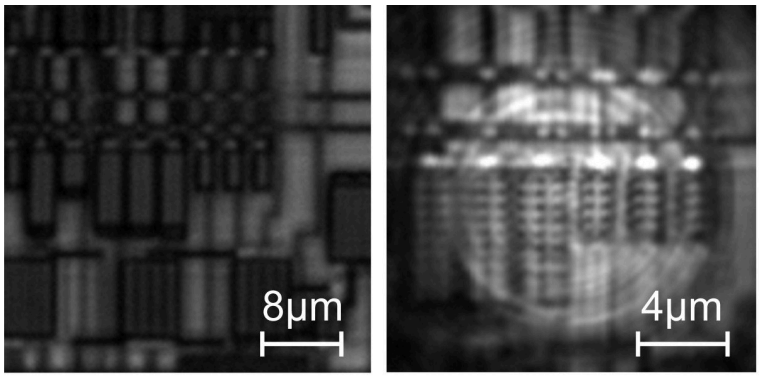

Fig. 120: LSM image without (left) and with (right) the rSIL shape created by a single chemistry-assisted FIB process on a 57 µm thick sample. This rSIL gives a significant improvement in resolution despite its not entirely perfect shape. The LSM image was taken at 1300 nm laser wavelength with a 0.7 NA objective.

Using the rSIL created by the chemistry-assisted FIB process led to a significant improvement in resolution. Image features with a width of about 370 nm could be easily resolved using the rSIL (referring to the "teeth of the comb structure" in Fig. 120). Though this structure is not a resolution test pattern with standardised pitch sizes, and Fig. 120 does not illustrate the limit of resolution using the etched rSIL, a rough comparison can still be made: The LSM can resolve a pitch size down to about 1100 nm

without rSIL, which corresponds to a line width of 550 nm (see Fig. 31 on page 48). Therefore the experiments were able to verify that a chemistry-assisted FIB process with an iodine-based chemistry is another promising solution for the creation of an rSIL in silicon. Further efforts are being made to achieve full control over this process for more precise and a larger variety of rSIL shapes.

5.3 dSIL creation in a single-step chemistry-assisted FIB process

While the previous chapters dealt with solid immersion lenses based on the principles of light refraction (rSILs), the author also chose to experiment with SILs based on diffraction. The exact type which was used is a binary diffractive SIL as introduced in chapter 3.3. For simplicity they will be referred to as “dSIL” in this work. Their creation with a FIB seems appealing, because the amount of material, which needs to be removed, is small compared to the rSILs. A more challenging aspect is to reliably produce the fine structures of a dSIL. The creation of dSILs in a single chemistry-assisted FIB process (see Fig. 121) is presented in this chapter. Details of the process are discussed along with the limits, which were encountered.

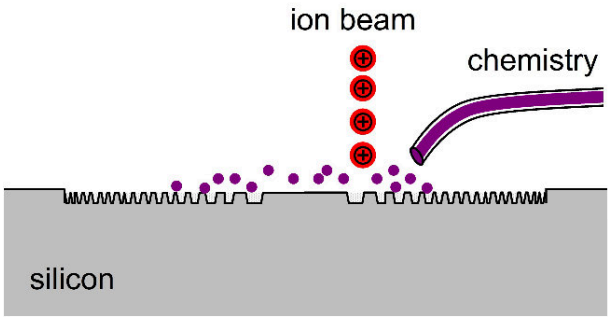

Fig. 121: Creation of a binary diffractive SIL in a chemistry-assisted FIB process.

5.3.1 Basic parameters of the FIB created dSIL

Before programming the FIB bitmap and preparing the sample, the basic parameters of the process needed to be defined. A sample thickness around 70 µm was used for good transparency of the silicon sample during infrared imaging inside the OptiFIB and a decent starting value for possibly following FIB editing. Another even more important aspect influencing the sample thickness was the opening angle, which should be realized by the dSIL. The dSIL was chosen to be used in a set-up equivalent to a central refractive SIL with a focus shift factor of one (see 3.2, 3.3, 3.4) for larger tolerances in sample thickness and virtual radius of curvature. The focus shift factor defines the ratio between sample thickness and virtual radius of curvature (see "P_0" and "P" in Fig. 39 on page 58). Using this set-up and the condition that at least the opening angle of a 0.7 NA objective (roughly 45°) should be achieved, meant a radius of the dSIL of about 75 µm. Therefore the full width of the dSIL, equal to the size of the needed FIB box, resulted in 150 µm. This value is still practical for FIB editing and enables surface editing within a reasonable processing time. It also leads to a pixel area of the FIB bitmap which was suitable for the process. The area of one pixel in a 150 µm by 150 µm FIB box with a bitmap resolution of 512 by 512 pixels is 290 x 290 nm^2. This size correlates well with the approximate diameter of the 2 nA beam current, which is about 250 nm (see ion beam diameters in Tab. 3 in Appendix 7.5 on page 163). Using this beam current means no overlap has to be taken into account and only a small underlap, which gives the opportunity to precisely recreate the pattern of the FIB bitmap. Based on this, the ion beam current of 2 nA was chosen for a good compromise between precise and efficient surface editing. At last the dwell time was set to 700 ns per pixel or a greyscale value of 10 in the area where the surface would be exposed to the ion beam. Thereby an efficient

surface processing without a depletion of the iodine-based chemistry could be expected.

These parameters (70 µm sample thickness equal to virtual radius of curvature, 75 µm radius of the dSIL fitting a 0.7 NA objective, 150 µm FIB box, 2 nA beam current) and a chosen wavelength of 1300 nm were used with the theory of dSILs presented in chapter 3.3 and 3.4 and in combination with chemistry-assisted FIB etching in bitmap mode introduced in 4.1, 4.2 and 4.3 to create the FIB bitmaps for dSIL creation. Appendix 7.4 lists the full program code for the dSIL bitmaps. One of which is shown again in Fig. 122. Moiré artefacts can be noticed in the bitmap, which occur after fitting the initially round dSIL structures into the FIB bitmap of limited resolution. The influence of these artefacts is analysed in the development of the process presented later.

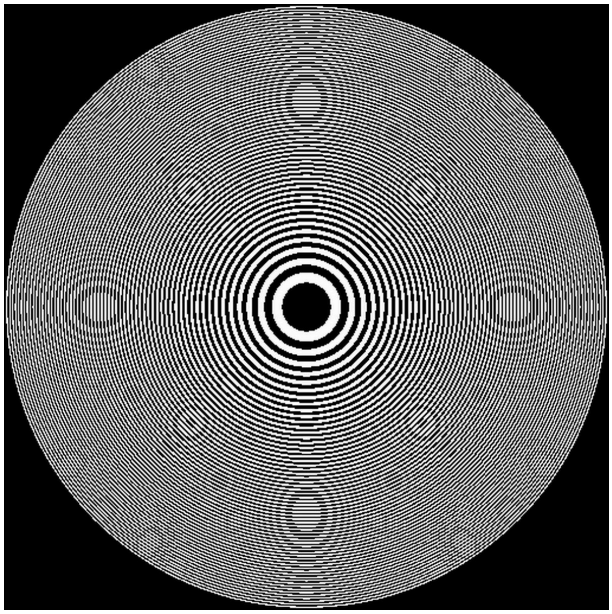

Fig. 122: FIB bitmap used for the binary dSIL creation with the OptiFIB. Moiré artefacts (off-centred circles) appear after placing the ideal round shapes of the dSIL into the rasterised FIB bitmap.

5.3.2 Creating the dSIL with the OptiFIB

The last missing parameter was the processing time. According to [20], a depth of about λ/(2(n - 1)) should be achieved for a binary dSIL structure. With the previously mentioned wavelength of 1300 nm and a corresponding index of refraction in silicon of about 3.5, this leads to a target depth of 260 nm. After a series of experiments, a processing time of 15 minutes was found to create the required depth in the centre of the dSIL. Fig. 123 and Fig. 124 show infrared OptiFIB images of the sample before and after dSIL creation with the presented parameters. The first was mostly used for navigation and the latter for process control. A FIB image of the dSIL from secondary electrons can be seen in Fig. 125. A more precise analysis, also used to measure the depth of the structure and thereby determine the proper processing time, was the AFM analysis illustrated in Fig. 126. The second optical image (Fig. 124), the FIB image (Fig. 125) and also an AFM measurement indicated that the Moiré artefacts from the FIB bitmap were in fact transferred into the physical shape of the dSIL. These artefacts were analysed and reduced during the development of the process (see later Fig. 129 and Fig. 136).

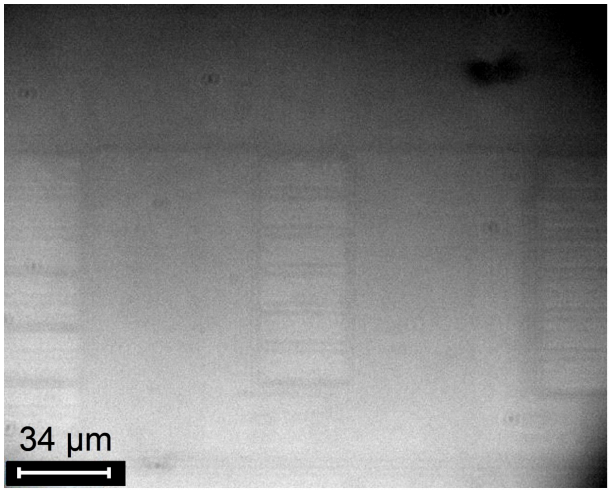

Fig. 123: Optical image from the infrared optics of the OptiFIB through 70 µm of bulk silicon before dSIL creation.

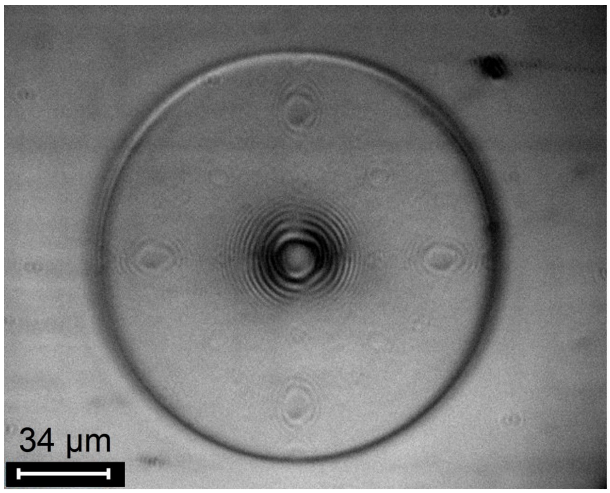

Fig. 124: Optical image from the infrared optics of the OptiFIB showing a FIB created dSIL. The image is focused on the surface to show the lens structure. Imaging through the lens did not work due to the non-monochromatic illumination. The OptiFIB uses filtered light of a Xenon lamp for illumination. The spectral width of the chosen 1000 nm filter is 70 nm.

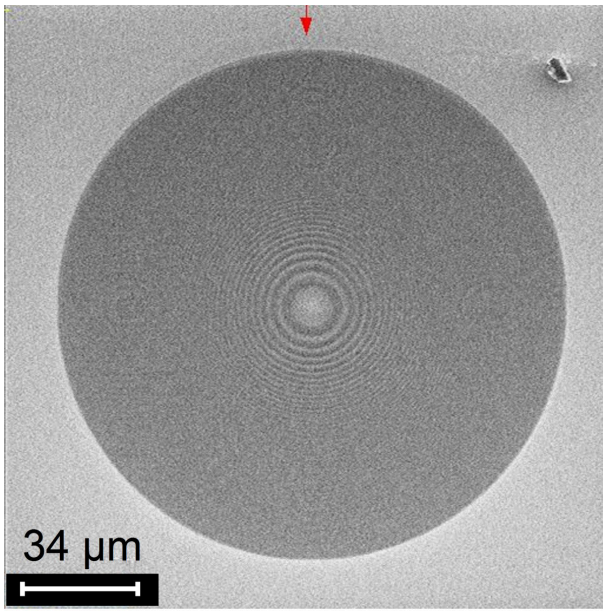

Fig. 125: Secondary electron image from the FIB after dSIL creation. Inner rings are visible, outer ones are too small to be resolved in this view. One can slightly make out the Moiré artefacts from the FIB bitmap, just like in the optical image Fig. 124: outer circles above, below, to the left and to the right of the centre.

5.3.3 Analyzing the FIB created dSIL

The AFM measurement of the FIB created dSIL shape (Fig. 126) showed that the pattern of the dSIL rings matched the expected dimensions and also that the depth had the required value, at least in the central part of the dSIL. It can be expected that the influence of the shape of the AFM tip is only minor for these depths. Looking at the aspect ratio of the tip from a manufacturer's SEM image, a full width of the tip of 250 nm can be assumed at a scanning depth of 300 nm [71]. The smallest width of the outermost zones is around 360 nm (see parameter "rj_deltamin" in the dSIL program of chapter 7.4), with a depth of only 260 nm or less. Therefore the measured deviations of the outer rings in depth and shape were mostly real and had to be kept in mind during the development.

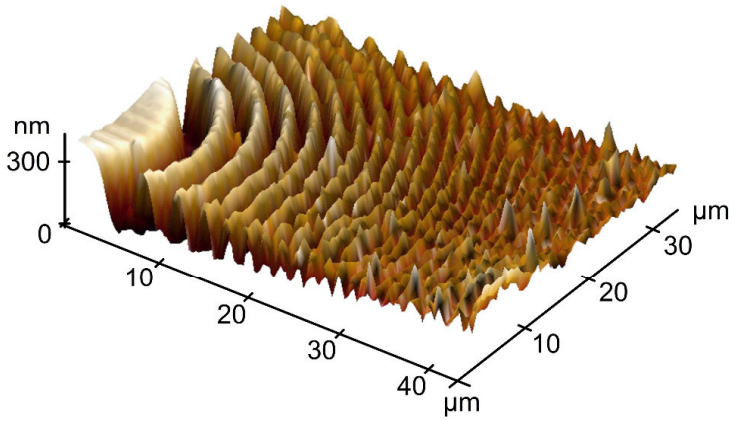

Fig. 126: AFM scan of the inner part of the FIB created dSIL. It can be observed, that the distances between the rings mostly match the expected values. Depth and shape of the inner rings are acceptable, while the rings towards the outside show strong deviations.

The dSIL was also analysed optically in an LSM to determine its effect despite the not fully ideal shape. Fig. 127 is an LSM image of one of the first FIB dSIL experiments and it shows an immediate optical benefit: The resolution visibly improved by using the FIB created dSIL. The image

feature which can be described as horizontal dashed line (see arrow in Fig. 127) has a width below 500 nm and is clearly resolved with the dSIL.

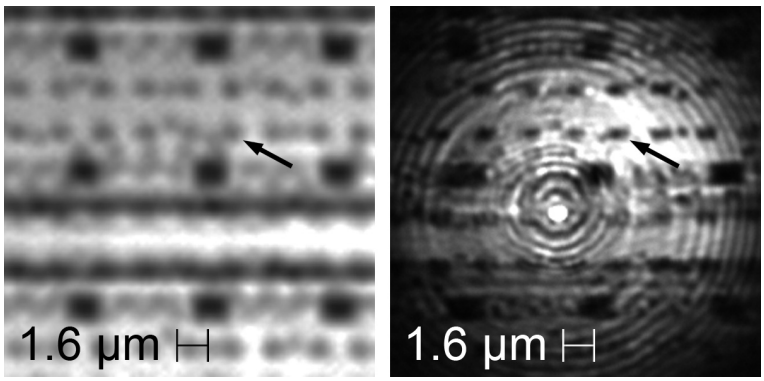

Fig. 127: LSM images left without and right with FIB created dSIL. The marked "horizontal dashed line" has a width below 500 nm as is clearly resolved with dSIL. The dSIL image still shows aberrations. This and all of the following LSM images of FIB created dSILs were taken with 1300 nm laser wavelength, a 0.7 NA objective and a sample thickness of about 70 µm. The images were cropped and scaled to show the same features.

Also apparent in the LSM image of Fig. 127 are aberrations. One possible reason for this was expected to be an error in the calculation of the radii during the first dSIL experiments. In the beginning the position of the steps was mistakenly thought to be best placed between the calculated radii and not right on the values of the radii as illustrated in Fig. 38 in chapter 3.3. This error was corrected and the corresponding LSM image showed a reduction in aberrations in the outer part of the field of view (Fig. 128). However a strong reflectance in the centre remained.

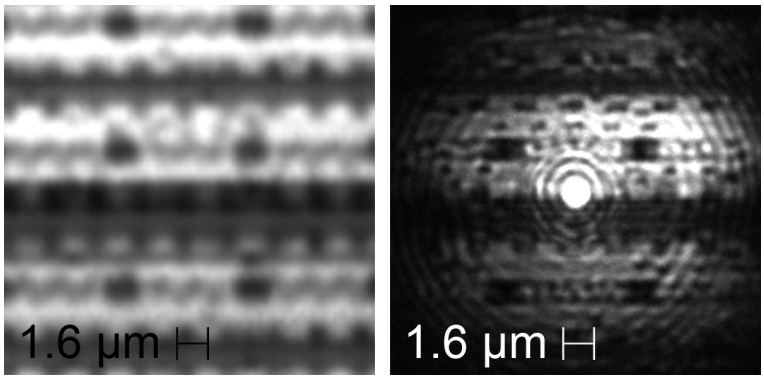

Fig. 128: LSM images taken with a 1300 nm laser. Left without and right with FIB created dSIL after optimizing the radii calculation. Aberrations towards the outside of the field of view could be reduced, but those in the centre remained.

5.3.4 Optimizing the FIB created dSIL

The first FIB created dSIL experiments were able to prove that the theory of dSILs could be transformed into optical components in silicon with a single-step chemistry-assisted FIB process. However, they also showed that some development of the process still needed to be done in search for an aberration-free LSM image. Motivated by this, a series of analysing and optimizing steps was set up. It consisted of determining the influence of the non-ideal outer rings, redesigning the FIB bitmap by taking the ion beam diameter into account, starting at a low level in the centre of the dSIL, increasing the greyscale values towards the outside of the dSIL, using a smaller beam current with smaller beam diameter and applying anti-aliasing during the creation of the FIB bitmap.

The influence of the non-ideal outer rings of the dSIL structure was determined by sequentially reducing the diameter of the dSIL pattern in the FIB bitmaps. This was achieved by leaving the pixels beyond a certain value of radius to stay black, meaning a greyscale value of 0 and a blanked ion beam (see (61) on page 70). All other parameters were kept constant (FIB box size, ion beam current, processing time) to maintain a

reproducible experimental environment with the same pixel area and ion beam diameter. Two of these cut bitmaps can be seen in Fig. 129 next to a regular dSIL FIB bitmap. They were used to create dSILs with a diameter of 120 µm and 90 µm instead of the initial 150 µm. Analysing the resulting dSILs in an LSM showed the same aberrations, but fewer image details as the diameter of the lens declined. The second result follows basic optical theory, where a smaller opening angle offers less resolution. Nevertheless, the dSILs still produced an image down to a diameter of 90 µm. Smaller dSILs e.g. with 60 µm diameter on the same sample could not be brought into focus. In conclusion, these experiments indicated that the outer rings of the FIB created dSIL do contribute to the imaging properties of the lens despite their non-ideal shape. The basic design of the process regarding size of the FIB box and number of rings was therefore maintained.

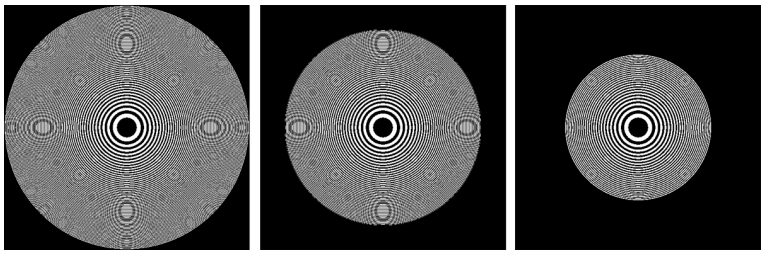

Fig. 129: Series of FIB bitmaps used to analyse the influence of the non-ideal outer rings of the FIB created dSILs.

Next part in the optimization of the FIB dSIL process was to take the diameter of the ion beam into account during bitmap programming. So far an ion beam diameter fitting precisely the pixel size was assumed. To verify or correct this assumption, an ion beam being bigger than the pixel area (290 x 290 nm^2, see 5.3.1) or scanning along the edge of the pixels was considered. In this case the resulting shape would be larger than the area predefined in the bitmap. The programming of the dSIL FIB bitmaps was adjusted accordingly. The underlying idea is illustrated in Fig. 130. The top image shows a side view of the created structure with the proper

outer positions of the ion beam for this structure (diameter symbol). The vertical dashed lines going from top to bottom image visually transfer these positions onto the FIB bitmap. The bright areas of the bitmap become a bit smaller with this procedure and possibly create the target shape more precisely, depending on beam scanning and beam diameter. An LSM image of a dSIL created with a FIB bitmap taking the ion beam diameter into account is shown in Fig. 131. This procedure again created a lens working in general, but could not reduce the aberrations in the image.

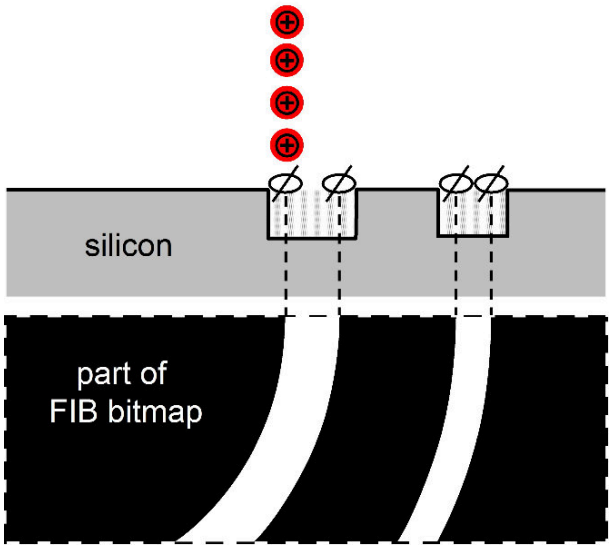

Fig. 130: Optimization of the FIB bitmaps taking the ion beam diameter into account. Top drawing shows desired dSIL shape and the corresponding outmost positions of the ion beam (diameter symbol). Bottom drawing shows part of FIB bitmap programmed according to these positions.

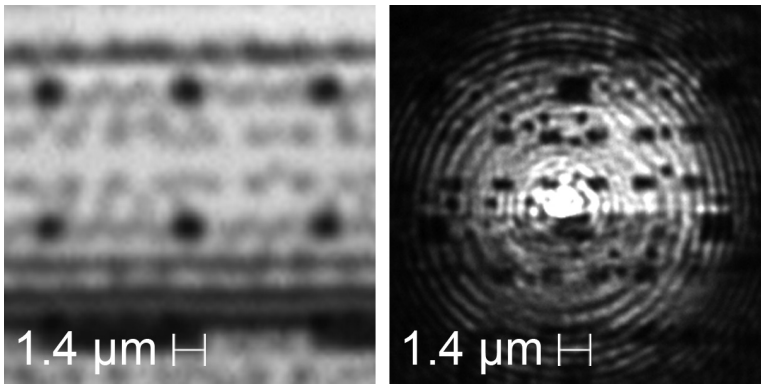

Fig. 131: LSM images taken with a 1300 nm laser. The ion beam diameter was taken into account in this experiment as described in Fig. 130. It resulted in a working dSIL, but not in an overall improvement of the image quality.

The next idea for optimizing the FIB dSIL used increasing greyscales towards the outside of the dSIL. The purpose of this was to enhance the processing of the outer rings. The width of these rings is very small, down to almost single pixels (smallest zones around 360 nm, see 5.3.3, pixel width 290 nm). A prolonged dwell time in this area was expected to improve the shape of these fine structures. Experiments were carried out with bitmaps programmed accordingly. Fig. 132 shows part of the greyscale values of the centre row of such a bitmap. The experimental results were again optically working dSILs, but without an improvement in image quality. An AFM and a SEM analysis showed that the shape of the outmost rings did not change significantly; merely the step between the last ring and the initial sample surface became deeper.

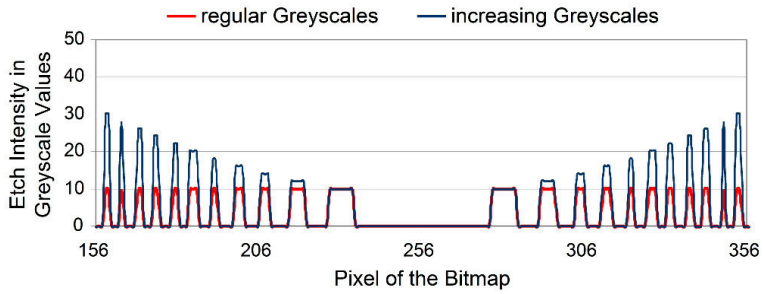

Fig. 132: Central part of regular greyscales and as a modification with increasing values.

Another aspect of the previously presented dSILs which ought to be addressed was the bright spot in the centre of the LSM images shown so far. This strong difference in intensity came from the increased illumination by and reflection of the laser in this area. The laser could be coupled into the sample more easily through the centre, likely because of better transparency due to the absence of FIB processing in this part of the surface. Therefore the reflection from this spot of the object plane back through the centre and partially through the rest of the lens surface was also stronger. Exposing the centre of the dSIL to the ion beam was the chosen method to possibly change this. The most FIB processing in the centre could be achieved by a dSIL shape following the same optical principle, but starting on a low level (see Fig. 133). The greyscale values of the part of the middle row of a corresponding bitmap can be seen in Fig. 134. The dSILs created with this method showed a similar behaviour as the previous ones, again without an improvement in the LSM image. Though this result did not optimize the dSIL, it could verify that the FIB processing with the assisting iodine-based chemistry did not have a major effect on the transparency of the silicon surface. It could therefore be expected that the chemistry fully removed the thin surface layer of gallium implanted into the silicon by the ion beam.

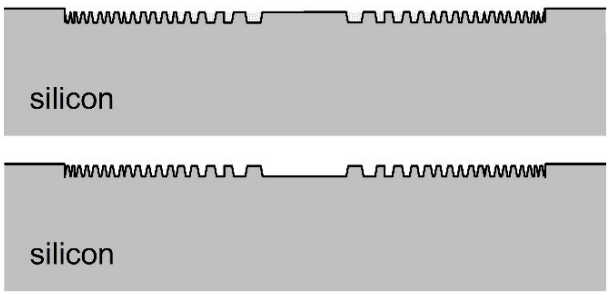

Fig. 133: Another modification of the FIB created dSIL was to use a low centre in order to address the bright spot in the centre of the LSM images. Results showed that this change did not make a difference. Optical theory was proven and these shapes worked similarly to the ones with a high centre.

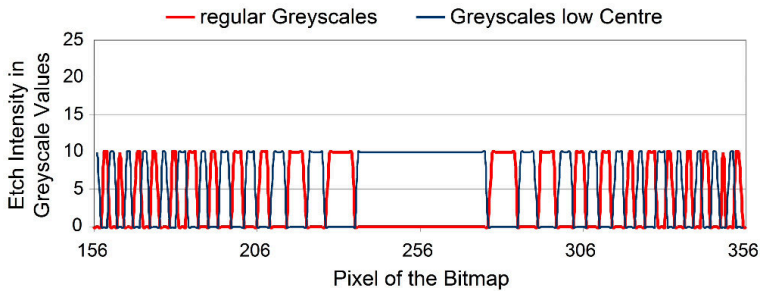

Fig. 134: Greyscale values used to create a dSIL shape with a high and low centre.

The ion beam current of the dSIL FIB process was modified second to last in search for an optimization. A smaller ion beam current with a smaller beam spot size can create finer structures, but also removes less material. In this case an ion beam current of 1 nA was used instead of the initial 2 nA. 15 minutes of processing were kept constant. The depth again showed high tolerance, because the thereby created dSIL structures maintained their optical functionality, though having a slightly changed depth. The inner zones were not influenced much by the smaller beam current, since their dimensions are beyond beam diameter. As for most of this optimization, the outer zones were to be improved. This could be partially achieved and, as shown in the beginning of this chapter (Fig. 129), even non-perfect outer zones contribute to image creation. The aberration in the middle of the LSM image could be reduced, while the rest of the image still left room for improvement (Fig. 135).

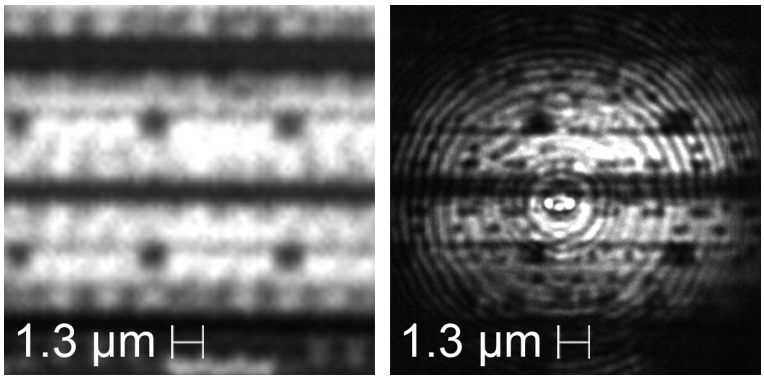

Fig. 135: LSM images taken with a 1300 nm laser. A smaller ion beam and a bitmap with ion beam diameter consideration were used to create this dSIL. The lens generally works optically, but still shows aberrations. A positive effect is the reduction of the bright spot in the centre of the FOV.

The last part in the optimization of the FIB created dSIL process dealt with the Moiré artefacts in the FIB bitmap. To do this, the rings of the dSIL were calculated just as before and then fitted into a bitmap programmed to a larger size of 4096 by 4096 pixels (factor of 8^2 of the initial bitmap). This size was found reasonable and practicable, because an increment in size by an even factor was chosen for better scaling and at 5120 by 5120 pixels (factor of 10^2, leading to over $26 \cdot 10^6$ data points) the author's computer did not have sufficient memory for the calculation, though containing up-to-date hardware. The enlarged bitmap was then scaled down to an OptiFIB compatible size of 512 by 512 pixels using an anti-aliasing filter. This filter uses intermediate greyscale values to better recreate the ideal curved shape in a rasterised bitmap. For example, if 51 % of a pixel were covered by a white ring of the ideal dSIL pattern, this pixel would so far have been fully white in the final FIB bitmap. With the anti-aliasing filter this pixel was given a greyscale value right in between the two extrema. In the presented process this would be a greyscale value of 5 for the given example, between 0 and 10. Other percentages of coverage were handled by the same principle. The reduction of the Moiré

patterns became instantly visible in the FIB bitmaps, as illustrated in Fig. 136 and in detail in Fig. 137.

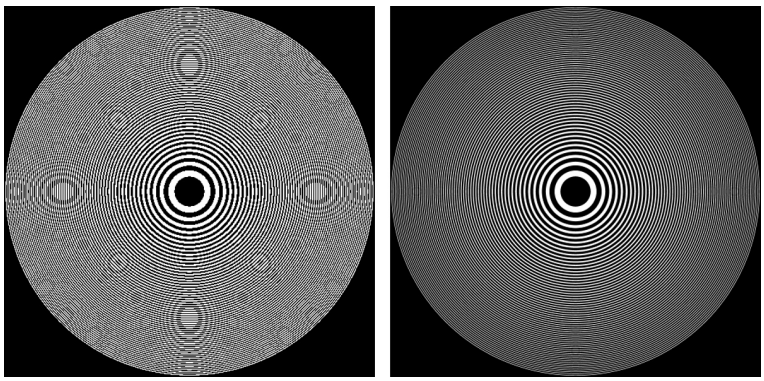

Fig. 136: FIB bitmaps without (left) and with anti-aliasing (right). Anti-aliasing uses intermediate greyscale values to better recreate the initially round shapes. A significant reduction of the Moiré patterns is the result. Details can be seen in Fig. 137.

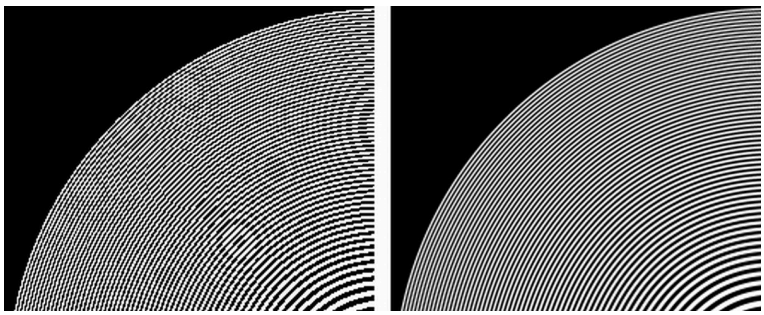

Fig. 137: Details of the FIB bitmaps without (left) and with anti-aliasing (right) shown in Fig. 136. The radii of the rings and the resolution of the bitmap are in both cases the same. Anti-aliasing helps to better recreate these rings in the rasterised bitmap.

dSIL experiments carried out with FIB bitmaps using anti-aliasing, taking the ion beam diameter into account and with a reduced beam current of 1 nA again created optically working lenses. The resulting LSM image can be seen in Fig. 138.

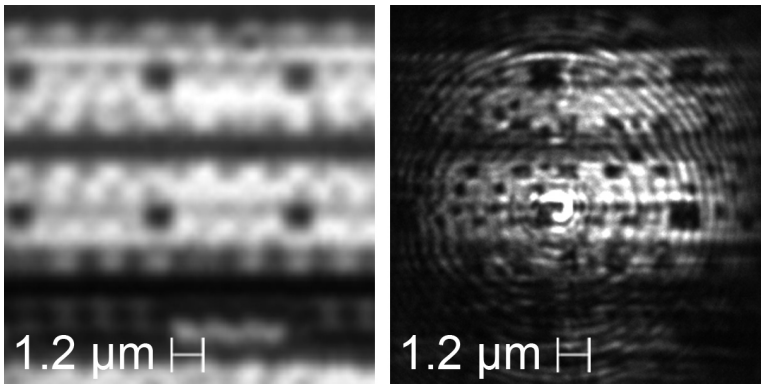

Fig. 138: LSM images taken with a 1300 nm laser. Left without and right with FIB created dSIL. A smaller ion beam current of 1 nA, a bitmap taking the ion beam diameter into account and anti-aliasing (see Fig. 136) were used in this experiment. It again created a working dSIL, but not a significant improvement in image quality.

However, all these optimizing methods couldn't eliminate the aberrations still present in the image. The combination did however lead to better results than applying the methods individually. Using bitmaps adjusted to the ion beam diameter also showed some benefit during the optimization. This is remarkable, as the ion beam diameter was initially chosen to fit the pixel area and thereby be a negligible parameter.

5.3.5 dSIL conclusions

It can be said, that compared to the dSIL experiments presented in the very beginning in Fig. 128, the optimizing methods improved the aberrations in the centre of the dSIL, but shifted them towards the rest of the field of view. A combination of both, leading to an aberration-free image could not be achieved. The optimized dSILs showed an increasing additional magnification (see scales of LSM images) which can be explained by small changes in sample thickness and a little shift in the virtual radius of curvature of the dSIL. The resolution remained the same, judging from visual analysis. In conclusion, the dSIL creation in a single-step chemistry-assisted FIB process showed to be somewhat robust

towards parameter changes and created generally working dSILs that could be brought into focus. The anisotropy of a masked plasma etch, as known from other FIB-assisted dSIL experiments [20] and needed for an ideal dSIL shape, could not be achieved despite numerous efforts and had to be left to further development.

5.4 Comparing chemistry-assisted FIB created rSILs and dSILs

Chapters 5.2 and 5.3 were able to prove the concept of creating rSILs and dSILs in a single chemistry-assisted FIB process. This leads to the question of which type of SIL better suits which application? The current chapter discusses a series of aspects of both SIL types and thereby helps to answer this question.

For better optical comparison, the rSIL created in a single chemistry-assisted FIB process (see 5.2) was also applied to the same sample as the dSIL of chapter 5.3. The LSM image (Fig. 139) with rSIL showed more details than without rSIL and had fewer aberrations than the dSIL images. Looking at the LSM images in direct comparison shows that the dSIL, despite the larger amount of aberrations, achieved a higher improvement in resolution for the presented SIL dimensions. This can be explained by the larger opening angle of the ideal dSIL shape.

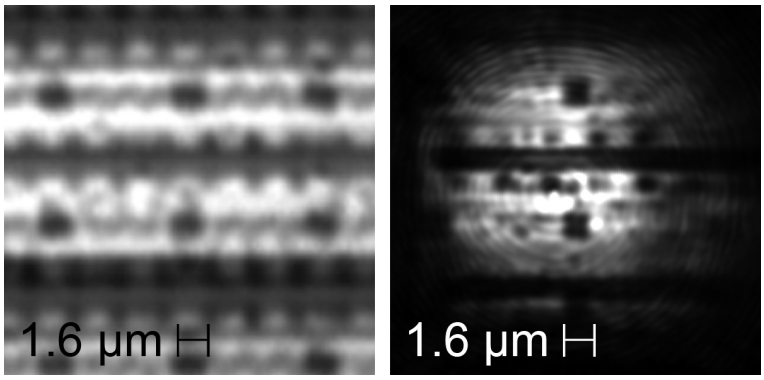

Fig. 139: LSM images taken with a 1300 nm laser. Left without and right with FIB created rSIL. The sample had a thickness of 55 µm and was analysed with a 0.5 NA objective matching the ideal opening angle of the rSIL. Images were scaled and cropped to show the same features.

Apart from the opening angle, Tab. 2 lists a series of additional parameters of the two FIB created rSIL types presented in chapters 5.2, 5.3 and 5.4. A similar table comparing common rSILs placed on the sample surface, dSILs created out of silicon (by combined FIB masking and plasma etching) and regular liquid immersion microscopy can be found in [14] p. 60.

Tab. 2: Comparison of diffractive and refractive SILs created with FIB in 5.2, 5.3 and 5.4.

	dSIL	**rSIL**
Diameter	150 µm	50 µm
Processing time	15 min	55 min
Ideal maximum depth	0.26 µm	≈ 5 µm
Width of processed area	150 µm	60 µm
Field of view (FOV)	≈ 20 µm	≈ 14 µm
Ratio of FOV / processed area	≈ 0.13	≈ 0.23
Needed ion beam current	1 - 2 nA	> 8 nA
Ion beam diameter	~ 140 - 250 nm	~ 1300 nm
Designed radius of curvature = sample thickness (hemispheric SIL model applied)	70 µm	65 µm
Adjustment to different sample thickness	easy	difficult
Maximum opening angle for ideal shape on sample thicknesses presented in 5.3 (dSIL) and 5.4 (rSIL) (70 µm for dSIL, 55 µm for rSIL)	47°	24°
Usable wavelength	monochromatic (1300 nm in this design)	broadband

Comparing the sets of parameters of Tab. 2 reveals how much faster a large SIL can be created by using a dSIL type, due to the much smaller amount of material removal. The ratio of the usable field of view over the required processing area is however better in the case of an rSIL. One could imagine an extreme situation, like the bottom of a small FIB trench, where the slightly smaller processing area of the rSIL could make a difference. For this specific condition, it has to be kept in mind that the sidewalls of the trench may require tapering according to the aspired opening angle. Looking at the ion beam current for each SIL again points out how much more material needs to be removed for the rSIL. The corresponding larger ion beam diameter makes precise FIB processing more challenging, but still feasible for the round rSIL shapes.

Both SIL types offer a certain tolerance in terms of sample thickness. Adapting a process to a new theoretically ideal sample thickness (which is equal to the radius of curvature in the hemispheric SIL model used in this work) is very easy for the dSIL, since it mostly means just designing a different FIB bitmap. For the rSIL this may be more difficult, because the whole etching behaviour of the FIB process may require a revision for a different lens shape.

One of the most appealing arguments in favour of the dSIL is the potentially wide opening angle. Thereby a larger NA and a higher improvement in resolution can be expected. In the presented FIB created SIL experiments, this advantage was partially defeated by the quality of the dSIL LSM images, which still contained more aberrations than some of the rSIL LSM images. Final aspect of the comparison is the spectral regime that these SILs allow. The rSIL is not dispersive in an ideal hemispheric rSIL set-up, as long as the silicon remains transparent. It would therefore be the right choice for broadband applications, such as photon emission microscopy (PEM) [6]. The dSIL is by its physical nature

designed for monochromatic light (see 3.3). There is some tolerance in this, but generally a narrow spectrum is needed for a dSIL. Therefore laser-based applications like laser stimulation techniques [8], [9] can make good use of the dSIL.

The data for this comparison comply with the presented experiments. It should be noted that during further optimization some parameters may need to be changed and thereby shift an advantage from one SIL type to another. Right now it can be said that in summary each SIL type has its advantages and specific fields of applications, which gives the motivation to develop both methods to their full potential.

6 Summary, conclusion and outlook

Three specific models of FIB created SILs are being presented in this work. Two of them are spherical refractive SILs (milled and etched rSIL) and one is a binary diffractive SIL. The milled rSIL, created by unassisted FIB milling, is 32 µm wide, has a height of 1.4 µm, a radius of curvature of 95 µm and needs well below 20 minutes of processing time. The individual processing steps are 10 minutes milling and one minute cleaning, to be precise. Albeit being of small dimensions, the milled rSIL successfully improved the resolution of an LSM by a factor of 1.8 and resolved 345 nm thick lines in a 690 nm pitch structure through 60 µm of silicon using a 1064 nm laser and a 0.5 NA objective (chapter 5.1.5). It was also used for light emission making small image features visible (chapter 5.1.6). Hence, it could not improve the signal-to-noise ratio (SNR) due to its small opening angle. Furthermore an ARC was deposited on the milled rSIL, significantly enhancing image contrast and reducing noise (chapter 5.1.7). It was shown, that FIB created SILs can easily be removed from a sample by polishing, despite the fact that they are cut into it (chapter 5.1.8). The influence of the sample thickness was investigated in depth. The ideal set-up for the presented milled rSIL was determined to be a sample thickness of 59 µm (chapter 5.1.9), close to the 60 µm used earlier.

With all this, the capabilities of FIB created SILs were demonstrated, but also the limits of the milled rSIL. Therefore a larger refractive SIL was developed and created by chemistry-assisted FIB etching (chapter 5.2). The etched rSIL is designed to be 50 µm wide, with a height of 5 µm and a

radius of curvature of 65 µm. Its creation takes less than 60 minutes of processing time.

An even larger SIL was realized in the kind of a binary dSIL, also by a chemistry-assisted FIB process (chapter 5.3). The FIB created dSIL is 150 µm wide, is made of structures only about 260 nm deep, has a virtual radius of curvature of 70 µm and needs merely 15 minutes of processing time. The LSM images of the etched rSIL and the dSIL showed significant improvement in resolution and contrast, but were not quite aberration-free. This can be explained by process inherent deviations from the perfect shape. The images did however prove the general functionality of the corresponding process.

The direct comparison of both techniques (chapter 5.4) illustrates that the rSILs are to be chosen for broadband applications, such as light emission. They have a good ratio of FOV over processed area, but are more complex to shape since a large amount of material needs to be removed. The dSILs on the other hand are designed for monochromatic, laser-based applications. Cutting them into precise patterns, like those achieved by traditional masked reactive ion etching [42], remains challenging with the FIB. Their advantage is that they can be created over large areas and easily adapted for various sample thicknesses. Therefore either type has its benefits and individual applications. Once the perfect shape is met, the effective NA of the etched rSIL, as shown in chapter 5.2 on a 57 µm thick sample or in chapter 5.4 on 55 µm, is about 1.5 (for definition of NA see equation (41) on page 52). The dSIL achieves a NA of 2.5 on 70 µm of silicon, as demonstrated in chapter 5.3. Both cases lead to a significant improvement in resolution (see resolution according to Rayleigh in equation (29) on page 34), and motivate to develop the presented methods to their full potential.

With its theory, the detailed process information and the proof of concept of the presented techniques, this work contains everything that is needed for further development and application of FIB created SILs - except a FIB tool. Future aspects may include analytic programming to optimize the FIB etched rSIL, by which a pixel wise feedback of an acquired shape onto the next experimentally created shape is meant. The FIB dSILs may benefit from a compound zone design implementing different orders of diffraction in a single dSIL pattern, as published for x-ray zone plates [72]. In any case, this work will be beneficial to those involved in the field of FIB created SIL techniques for the improvement of optical imaging through silicon.

7 Appendix

7.1 Verifying the quadratic dSIL equation $\alpha a_j^2 + \beta a_j + \chi = 0$ (54)

This chapter explains the mathematical operations leading to equation (54) on page 60. An illustration of the parameters can be found in Fig. 39 on page 58. The initial step is to extract the square root of (53) and insert it into (51).

$$\alpha a_j^2 + \beta a_j + \chi = 0 \qquad ((54))$$

$$k^2t^2 + r_j^2 = a'^2_j \qquad ((53))$$

$$a'_j = na_j + t(k - n) - jm\lambda_0 \qquad ((51))$$

This results in

$$\underbrace{\sqrt{k^2t^2 + r_j^2}}_{a_j\text{'see (48)}} = \underbrace{na_j + t(k - n) - jm\lambda_0}_{a_j\text{'see (46)}}. \qquad (82)$$

Now (52) is solved for r_j^2 and placed into (82). Part of the thereby created equation is combined in a new parameter $A = t(k - n) - jm\lambda_0$.

$$t^2 + r_j^2 = a_j^2 \qquad ((52))$$

$$\sqrt{k^2t^2 + a_j^2 - t^2} = na_j + \underbrace{t(k - n) - jm\lambda_0}_{A} \qquad (83)$$

The entire equation (83) is squared and later solved for 0 with t^2 extracted.

$k^2t^2 + a_j^2 - t^2 = n^2a_j^2 + 2nAa_j + A^2$

$t^2(k^2 - 1) + a_j^2 - n^2a_j^2 - 2nAa_j - A^2 = 0$

From this, the parameter α can instantly be verified. The rest of the equation is declared in parts as B and C.

$$\underbrace{(1 - n^2)}_{=\alpha}a_j^2 + \underbrace{2n(-A)}_{B}a_j + \underbrace{t^2(k^2 - 1) - A^2}_{C} = 0$$

B can be verified to be equal to β when inserting A.

B: $2n(-A) = 2n[t(n - k) + jm\lambda_0] = \beta$

Finally, part C is equal to χ after a bit of calculation, verifying equation (54).

C: $t^2(k^2 - 1) - A^2 = t^2(k^2 - 1) - [t^2(k - n)^2 - 2t(k - n)\, jm\lambda_0 + (jm\lambda_0)^2]$

$= t^2(k^2 - 1 - k^2 + 2kn - n^2) + 2t(k - n)jm\lambda_0 - (jm\lambda_0)^2$

$= t^2(2kn - n^2 - 1) + 2t(k-n)jm\lambda_0 - j^2(m\lambda_0)^2$

$= \chi$

7.2 Program code of OptiFIB bitmaps for creating rSILs by unassisted FIB milling (see chapter 5.1)

```
%-------------- create base coordinates and matrix --------------
% amount of pixels in x- and y-direction
nxy = 512;

% nxy equal rows going from -255 to 256 in nxy steps
x = ([0:1:nxy-1]*0+1)'*[0:1:nxy-1]-255;
% nxy equal columns going from -255 to 256 in nxy steps
y = [0:1:nxy-1]'*([0:1:nxy-1]*0+1)-255;

% creating the base matrix using the Pythagorean theorem to give
% each element the value of its radius (distance from the centre
% of the matrix in pixels)
matrix = sqrt(x.^2+y.^2);
```

```
%- create greyscales for sputtered rSIL based on spherical model -
% radius of rSIL in pixels, a distance of 8 pixels to the edge of
% the bitmap was chosen
r1 = 248;

% upper half of a spherical shape 2*r1 wide and r1 high,
nm1 = abs(r1^2 - x.^2 - y.^2).^(1/2);

s = 1.66; % scaling factor for the sputtered rSIL process
nm2 = nm1/s; % adjusting the spherical shape

% inverting the shape to achieve minimum greyscale value
% in the middle of the rSIL
nm3 = nm2(256,256) - nm2;

% greyscale values are lifted by "1" (= gsmin) to avoid zero ion
% beam processing in the centre of the rSIL
data = nm3 + 1;
% outside of rSIL is filled with greyscale value "0"
data (matrix > r1) = 0;


%---------------------- create bitmap file -----------------------
% filename according to "bm-rSIL-r1-gsmin-gsmax-s.tif"
filename = strcat('bm-rSIL-',num2str(r1),'-1',num2str((r1+1)/s),
'-',regexprep(num2str(s),'[.]','_'),'.tif');

% creates the OptiFIB compatible image file, "data/255" is used
% because the range of greyscales needs to be between 0 and 1
imwrite(data/255,filename,'tif','Compression','none');
% reloading the created bitmap for verification
image = imread (filename, 'tif');
```

7.3 Program code of OptiFIB bitmaps for creating rSILs in a single-step chemistry-assisted FIB process (see chapter 5.2)

```
%-------------- create base coordinates and matrix --------------
% amount of pixels in x- and y-direction
nxy = 512;

% nxy equal rows going from -1 to 1 in nxy steps
x = (([0:1:nxy-1]*0+1)'*([0:1:nxy-1]/(nxy-1))-0.5)*2;
% nxy equal columns going from -1 to 1 in nxy steps
y = (([0:1:nxy-1]/(nxy-1))'*([0:1:nxy-1]*0+1)-0.5)*2;

% creating the base matrix using the Pythagorean theorem to give
% each element the value of its radius (distance from the centre
```

```
% of the matrix in values between 0 and sqrt2 = 1.41)
matrix = sqrt(x.^2+y.^2);


r1 = 213/256;    % inner radius (radius of rSIL) normalised to 1
                 % (1 ^= 256 pixels)
r2 = 256/256;    % outer radius (radius of surrounding ring)
                 % normalised to 1 (1 ^= 256 pixels)
g1 = 255;        % maximum greyscale value for the rSIL
g2 = 255;        % greyscale of surrounding ring
g3 = 0;          % greyscale outside of surrounding ring
 n = 8.0;        % factor of shape adjustment for
                 % chemistry-assisted rSIL in steps of 0.5

% upper half of a spherical shape 2*r1 wide and 1 high,
% "(r1/r1)^2" just used to clearly show initial formula of sphere
nm1 = abs((r1/r1)^2 - (x/r1).^2 - (y/r1).^2).^(1/2);

%--- modifying the spherical shape for chemistry-assisted rSIL ---
% adjusting the shape for chemistry-assisted rSIL
nm2 = nm1.^(2/n);
% inverting the shape to achieve minimum greyscale value in the
% middle of the rSIL
nm3 = 1 - nm2;

% model of the sphere is scaled by maximum greyscale value for
% the rSIL, "-1,+1" lifts the entire previously shifted and
% inverted sphere by a greyscale of 1 to avoid zero ion beam
% processing in the centre of the rSIL
data = (nm3*(g1-1))+1;
% surrounding ring is filled with corresponding greyscale value
data( (matrix > r1) & (matrix < r2) ) = g2;
% area outside of surrounding ring is filled with corresponding
% greyscale value
data( (matrix >= r2) ) = g3;

%---------------------- create bitmap file -----------------------
% filename according to " bm-rSIL-r1-r2-g1min-g1-g2-g3-n.tif "
filename = strcat('bm-rSIL-',num2str(r1*256),'-',num2str(r2*256),
'-1-',num2str(g1),'-',num2str(g2),'-',num2str(g3),'-',
regexprep(num2str(n,'%.1f'),'[.]','_'),'.tif');

% creates the OptiFIB compatible image file, "data/255" is used
% because the range of greyscales needs to be between 0 and 1
imwrite(data/255,filename,'tif','Compression','none');
% reloading the created bitmap for verification
image = imread (filename, 'tif');
```

7.4 Program code of OptiFIB bitmaps for creating dSILs in a single-step chemistry-assisted FIB process (see chapter 5.3)

```
%------------------ calculate dSIL radii --------------------
NA = 0.7;   % numerical aperture of the used objective
lambda = 1.300;     % used wavelength in air in µm
n = 3.5;    % index of refraction of silicon for used wavelength
t = 70;     % sample thickness in µm
k = 1;      % focus shift factor
m = 0.5;    % diffraction factor for the calculation of
            % constructive and destructive interference

% rounded max radius to fit NA of objective + 10%
rmax = round(1.1*t*tan(asin(NA)));

alpha = 1-n^2; % see dSIL theory, alpha does not change if j does

% maximum of loop control variable j is just for backup
% the loop always "breaks"  before reaching the maximum value
% several vectors are filled with j-depending values
% see dSIL theory for further mathematical details
for j = 1:500

    % for the origin of beta and chi see dSIL theory
    beta = 2*n*(t*(n-k)+j*m*lambda);
    chi = t^2*(2*k*n-n^2-1)+2*t*(k-n)*j*m*lambda-(j*m*lambda)^2;

    % solving the quadratic equation
    p = beta/alpha;
    q = chi/alpha;

    % aj with negative root to solve the quadratic equation
    aj = p/2-sqrt((p/2)^2-q);
    % rj calculated using aj
    rj(j) = sqrt(aj^2-t^2);

    % simplified rj for k=1 and m=1 (just for verification)
    rjk1m1(j) = sqrt(2*j*lambda*t/(n-1)+(j*lambda/(n-
1))*(j*lambda/(n-1)));
    if rj(j) >= rmax    % if rj is bigger than max needed radius..
        rj(j) = [];     % delete last entry of rj
        rjk1m1(j) = []; % delete last entry of rjk1m1
        j = j-1;        % j is now the index of the last element
        break
    end
end

rjmax = rj(j); % biggest radius in rj in µm
% distance between the last two radii = smallest dimension of dSIL
rj_deltamin = rj(j) - rj(j-1);
```

```
%-------------- create base coordinates and matrix --------------
% amount of pixels in x- and y-direction
nxy = 512;
% half width of FIB box being large enough to fit used objective
dxy = rmax;

% nxy equal rows going from -1 to 1 in nxy steps
x = (([0:1:nxy-1]*0+1)'*([0:1:nxy-1]/(nxy-1))-0.5)*2;
% nxy equal columns going from -1 to 1 in nxy steps
y = (([0:1:nxy-1]/(nxy-1))'*([0:1:nxy-1]*0+1)-0.5)*2;

% creating the base matrix using the Pythagorean theorem to give
% each element the value of its radius (distance from the centre
% of the matrix in µm)
matrix = sqrt((x*dxy).^2 + (y*dxy).^2);


%--- distribute greyscale values according to calculated radii ---
gslow = 0;      % low greyscale value
gshigh = 010;   % high greyscale value

values = zeros(nxy,nxy);    % create empty matrix for the bitmap
for i = 1:j-1 % go through all of the previously calculated radii
  r1 = rj(i);               % first pick one radius...
  r2 = rj(i+1);             % then pick next radius and then...
  % put gslow in between if index of first radius is even...
  if (round(i/2) == i/2)
    values((r1 <= matrix) & (matrix < r2)) = gslow;
  % or fill area in between with gshigh if index is uneven
  else
    values((r1 <= matrix) & (matrix < r2)) = gshigh;
  end
end

% fill area outside of the last radius with gslow
values( matrix > rj(j) ) = gslow;
% now values contains the greyscale values for the bitmap


%--------------------- create bitmap file ----------------------
% filename according to "bm-dSIL-rmax-f-k-gshigh-m-lambda.tif"
filename = strcat('bm-dSIL-',num2str(rmax),'um-',num2str(f),
'um-',num2str(k),'-gs',num2str(gshigh,'%03d'),'-',
regexprep(num2str(m,'%.1f'),'[.]','_'),'-',
num2str(lambda*1000),'.tif');

% creates the OptiFIB compatible image file, "data/255" is used
% because the range of greyscales needs to be between 0 and 1
imwrite(values/255,filename,'tif','Compression','none');
% reloading the created bitmap for verification
image = imread (filename, 'tif');
```

7.5 Set of ion beam diameters at various beam currents

Tab. 3: Set of roughly defined ion beam diameters at various beam currents, supplied to the author by DCG Systems.

beam current	approximate beam diameter
50 pA	40 nm
100 pA	55 nm
200 pA	60 nm
250 pA	70 nm
500 pA	110 nm
1 nA	145 nm
2-3 nA	245 nm
4 nA	670 nm
6 nA	850 nm
~ 9 nA	1300 nm
12 nA	3600 nm

References

[1] G. E. Moore, “Cramming more components onto integrated circuits, Reprinted from Electronics, volume 38, number 8, April 19, 1965, pp.114 ff.,” *IEEE Solid-State Circuits Newsletter*, vol. 20, no. 3, pp. 33-35, Sep. 2006.

[2] K. J. Kuhn, “Moore’s Law Past 32nm: Future Challenges in Device Scaling,” *2009 13th International Workshop on Computational Electronics*, pp. 1-6, May 2009.

[3] Renesas Electronics Corporation, *Semiconductor Reliability Handbook*, Rev. 1.01. 2008.

[4] S. M. Mansfield and G. S. Kino, “Solid immersion microscope,” *Applied Physics Letters*, vol. 57, no. 24, p. 2615, 1990.

[5] G. S. Kino, “Solid immersion lens,” *Proceedings of SPIE*, vol. 3740, no. June, pp. 2-5, 1999.

[6] C. Boit, “Fundamentals of Photon Emission (PEM) in Silicon – Electroluminescence for Analysis of Electronic Circuit and Device Functionality,” *Microelectronics Failure Analysis: Desk Reference 5th Edition*, pp. 357-369, 2004.

[7] O. Breitenstein, F. Altmann, T. Riediger, D. Karg, and V. Gottschalk, “Lock-in thermal IR imaging using a solid immersion lens,” *Microelectronics and Reliability*, vol. 46, no. 9–11, pp. 1508-1513, Sep. 2006.

[8] F. Beaudoin, R. Desplats, P. Perdu, and C. Boit, “Principles of Thermal Laser Stimulation Techniques,” *Microelectronics Failure Analysis: Desk Reference 5th Edition*, pp. 417-425, 2004.

[9] S. Brahma, J. Heinig, A. Glowacki, R. Leihkauf, and C. Boit, “Distinction of Photo-Electric and Thermal Effects in a MOSFET by 1064 nm Laser Stimulation,” *13th International Symposium on the Physical and Failure Analysis of Integrated Circuits*, pp. 333-339, Jul. 2006.

[10] S. Perungulam and K. S. Wills, “Chip access techniques,” *Microelectronics Failure Analysis: Desk Reference 5th Edition*, pp. 312-322, 2004.

[11] R. Soref and B. Bennett, “Electrooptical effects in silicon,” *IEEE Journal of Quantum Electronics*, vol. 23, no. 1, pp. 123-129, Jan. 1987.

[12] DCG Systems, “DCG Systems - Meridian.” [Online]. Available: http://www.dcgsystems.com/product.meridian-IV.html. [Accessed: 18-Jan-2012].

[13] Hamamatsu, “NanoLens (Solid Immersion Lens).” [Online]. Available: http://sales.hamamatsu.com/assets/applications/SD/e_nanolens.pdf.

[14] S. H. Goh, “Development and characterization of refractive solid immersion lens technology for far-field integrated circuit faillure analysis using laser induced techniques,” National University of Singapore, 2009.

[15] D. a. Fletcher et al., “Microfabricated silicon solid immersion lens,” *Journal of Microelectromechanical Systems*, vol. 10, no. 3, pp. 450-459, 2001.

[16] S. Goh, J. Cho, and J. Lam, “Mobile Diffractive Solid Immersion Lens Design for Backside Laser Based Fault Localization,” in *Proceedings of ISTFA 2010*, 2010, vol. 1, pp. 32-37.

[17] S. B. Ippolito, “High Spatial Resolution Subsurface Microscopy,” Boston University, 2004.

[18] K. A. Serrels, “Ultra-high-resolution optical imaging for silicon integrated-circuit inspection,” Heriot-Watt University, 2009.

[19] T. Koyama, E. Yoshida, J. Komori, Y. Mashiko, T. Nakasuji, and H. Katoh, “High resolution backside fault isolation technique using directly forming Si substrate into solid immersion lens,” *2003 IEEE International Reliability Physics Symposium Proceedings, 2003. 41st Annual.*, pp. 529-535.

[20] F. Zachariasse and M. Goossens, “Diffractive lenses for high resolution laser based failure analysis,” in *Proceedings of ISTFA 2005*, 2005, pp. 1-7.

[21] T. Wilson and C. Sheppard, *Theory and practice of scanning optical microscopy*. Academic Press Inc, 1984.

[22] M. Born and E. Wolf, *Principles of Optics: Electromagnetic Theory of Propagation, Interference and Diffraction of Light*, 7th ed. Cambridge University Press, 2000.

[23] M. Mansuripur, *Classical Optics and its Applications*. Cambridge University Press, 2009.

[24] J. W. Goodman, *Introduction to Fourier Optics*. Roberts & Co, 2005.

[25] E. Hecht, *Optics (4th Edition)*. Addison Wesley, 2002.

[26] G. B. Airy, “On the diffraction of an object-glass with circular aperture,” *Transactions of the Cambridge Philosophical Society*, vol. 5, no. 3, pp. 283-291, 1835.

[27] L. Rayleigh, “Investigations in optics, with special reference to the spectroscope,” *Philosophical Magazine*, vol. 8(50), no. Ser. 5, pp. 403-411, 1879.

[28] C. M. Sparrow, “On spectroscopic resolving power,” *The Astrophysical Journal*, vol. 44, pp. 76-86, 1916.

[29] W. V. Houston, “A compound interferometer for fine structure work,” *Physical Review*, vol. 29, pp. 478-485, 1927.

[30] A. Jones, J. Bland-Hawthorn, and P. Shopbell, “Towards a general definition for spectroscopic resolution,” in *Astronomical Data Analysis Software and Systems IV ASP Conference Series*, 1995, vol. 77.

[31] V. N. Mahajan, “Uniform versus Gaussian beams: a comparison of the effects of diffraction, obscuration, and aberrations,” *Journal of the Optical Society of America A*, vol. 3, no. 4, p. 470, 1986.

[32] “File:Airy vs gaus.svg - Wikipedia, the free encyclopedia.” [Online]. Available: http://en.wikipedia.org/wiki/File:Airy_vs_gaus.svg. [Accessed: 27-Oct-2011].

[33] Zeiss, “Microscopy from Carl Zeiss.” [Online]. Available: http://www.zeiss.de/C1256D18002CC306/0/659347F4EDA5061AC1256E5C0045F690/$file/45_0024_e.pdf.

[34] “Olympus Microscopy Resource Center | Confocal Microscopy - Introduction.” [Online]. Available: http://www.olympusmicro.com/primer/techniques/confocal/confocalintro.html. [Accessed: 27-Oct-2011].

[35] Hamamatsu, “PHEMOS-1000.” [Online]. Available: http://sales.hamamatsu.com/assets/pdf/hpspdf/Phemos1000.pdf.

[36] E. Ramsay, N. Pleynet, D. Xiao, R. J. Warburton, and D. T. Reid, “Two-photon optical-beam-induced current solid-immersion imaging of a silicon flip chip with a resolution of 325 nm.,” *Optics letters*, vol. 30, no. 1, pp. 26-8, Jan. 2005.

[37] F. L. Pedrotti, L. S. Pedrotti, and L. M. Pedrotti, *Introduction to optics*. Pearson Prentice Hall, 2007.

[38] L. Bergmann, H. Niedrig, and C. Schaefer, *Lehrbuch der Experimentalphysik: Optik: Wellen- und Teilchenoptik*. Walter de Gruyter, 2004.

[39] W. J. Smith, *Modern Optical Engineering*. McGraw-Hill, 2008.

[40] E. Whittaker and V. Twersky, “A History of the Theories of Aether and Electricity. The Classical Theories,” *Physics Today*, vol. 5, no. 7, p. 15, 1952.

[41] T. Fricke-Begemann, J. Ihlemann, and J. Meinertz, “Diffraktive Mikrolinsen: Herstellung durch direkte Laserstrukturierung,” in *DGaO-Proceedings 2006*, 2006, no. 5.

[42] E. Coyne and F. Zachariasse, “A working method for prototyping solid immersion blazed-phase diffractive optics for near-infrared laser microscopy,” *Journal of Micromechanics and Microengineering*, vol. 18, no. 4, pp. 1-9, Apr. 2008.

[43] R. Brunner et al., “Diffraction-based solid immersion lens.,” *Journal of the Optical Society of America. A, Optics, image science, and vision*, vol. 21, no. 7, pp. 1186-1191, Jul. 2004.

[44] Clemens Helfmeier, “Focused ion beam system | TikZ example.” [Online]. Available: http://www.texample.net/tikz/examples/focused-ion-beam-system/. [Accessed: 21-Jan-2012].

[45] C. Tsao, Q. Wang, P. Bouchet, and P. Sudraud, “Coaxial Ion-Photon System,” *Microelectronics Reliability*, vol. 41, no. 9–10, pp. 1483-1488, Sep. 2001.

[46] Credence Systems Corporation, “OptiFIB and P3X User Manual 57510467 Rev4,” 2005.

[47] J. Orloff, L. Swanson, and M. W. Utlaut, *High resolution focused ion beams: FIB and its applications: the physics of liquid metal ion sources and ion optics and their application to focused ion beam technology*. Springer, 2003.

[48] N. Kudo, K. Tsunoda, and Y. Terui, “Liquid metal ion source and method for producing the same,” 28-Jan-2000.

[49] M. Lodzinski, “Focused Ion Beam 3-D topology etch process using XeF2 jet gas assistance,” Technische Universität Berlin, 2005.

[50] T. Zarzycki, “Gas Assisted Bitmap Milling to Create 3D Topologies Using a Focused Ion Beam Tool,” Technische Universität Berlin, 2006.

[51] B. Marszałek, “Multiple Bitmap Milling in a Focused Ion Beam Tool to Create 3D Topologies,” Technische Universität Berlin, 2007.

[52] U. Todorovic, “Parameteroptimierung unter Anwendung eines mathematischen Modells für gasunterstützte Ätzprozesse in einer FIB-Anlage zur Erzeugung von 3D-Topologien,” Technische Universität Berlin, 2008.

[53] X. Xu, “Focused ion beam induced deposition and ion milling as a function of angle of ion incidence,” *Journal of Vacuum Science & Technology B: Microelectronics and Nanometer Structures*, vol. 10, no. 6, p. 2675, Nov. 1992.

[54] T. Ishitani, “Improvements in performance of focused ion beam cross-sectioning: aspects of ion-sample interaction,” *Journal of Electron Microscopy*, vol. 53, no. 5, pp. 443-449, Oct. 2004.

[55] K. P. Müller and H.-C. Petzold, “Microstructuring of gold on x-ray masks with focused Ga+ ion beams,” in *Proceedings of SPIE*, 1990, vol. 1263, no. 1, pp. 12-20.

[56] K. Sugano and O. Tabata, “Effects of etching pressure and aperture width on Si etching with XeF2,” *Proceedings of 2000 International Symposium on Micromechatronics and Human Science*, pp. 89-94, 2000.

[57] B. Bahreyni and C. Shafai, “Deep Etching of Silicon with XeF2,” in *Proceedings of the 2002 IEEE CCECE*, 2002, pp. 460-464.

[58] L. R. Harriott, “Digital scan model for focused ion beam induced gas etching,” *Journal of Vacuum Science & Technology B: Microelectronics and Nanometer Structures*, vol. 11, no. 6, p. 2012, Nov. 1993.

[59] P. F. Ullmann, C. G. Talbot, R. A. Lee, C. Orjuela, and R. Nicholson, “A New Robust Backside Flip-Chip Probing Methodology,” in *Proceedings of ISTFA 1996*, 1996, pp. 381-386.

[60] S. Czapski and T. R. Lundquist, “Improved FIB Modification Success-Rate on Analog & Sensitive Digital Devices,” in *Proceedings of ISTFA 1995*, 1995.

[61] H. Ximen and C. G. Talbot, “Halogen-Based Selective FIB Milling for IC Probe-Point Creation and Repair,” in *Proceedings of ISTFA 1994*, 1994, p. 141.

[62] M. Tamura, S. Shukuri, M. Moniwa, and M. Default, “Focused ion beam gallium implantation into silicon,” *Applied Physics A Solids and Surfaces*, vol. 39, no. 3, pp. 183-190, Mar. 1986.

[63] M. Abramo, D. L. Barton, R. H. Livengood, N. Antoniou, and K. N. Hooghan, “FIB Backside Isolation Techniques,” *Electronic Device Failure Analysis*, 2001.

[64] N. M. Amer and G. Meyer, “Atomic force microscopy.” 27-Jan-1997.

[65] “SPM Principles — NT-MDT.” [Online]. Available: http://www.ntmdt.com/spm-principles. [Accessed: 28-Oct-2011].

[66] “SPM Basics — NT-MDT.” [Online]. Available: http://www.ntmdt.com/spm-basics. [Accessed: 28-Oct-2011].

[67] P. J. Eaton, P. Eaton, and P. West, *Atomic force microscopy*. Oxford University Press, 2010.

[68] H.-G. Wagemann and A. Schmidt, *Grundlagen der optoelektronischen Halbleiterbauelemente*. Vieweg +Teubner, 1997.

[69] A. B. Kahng, K. Samadi, and R. O. Topaloglu, “Recent topics in CMP-related IC Design for Manufacturing,” in *Proc. Advanced Metallization Conference*, 2008.

[70] C. Richardson, F. C. LSI, T. Malik, V. Makarov, and others, “Insulator Deposition for Through Conductor Editing,” in *Proceedings of ISTFA 2008*, 2008, pp. 151-156.

[71] “CSG10 — NT-MDT Tips.” [Online]. Available: http://www.ntmdt-tips.com/products/view/csg10. [Accessed: 28-Oct-2011].

[72] A. Kuyumchyan, “High-efficiency and low-absorption Fresnel compound zone plates for hard X-ray focusing,” *Proceedings of SPIE*, vol. 4783, no. 3, pp. 92-96, 2002.

List of Publications

I P. Scholz, U. Kerst, C. Boit, C.-C. Tsao, and T. R. Lundquist, “Creation of Solid Immersion Lenses in Bulk Silicon Using Focused Ion Beam Backside Editing Techniques,” in *Proceedings of ISTFA 2008*, 2008, pp. 157-162.

II P. Scholz, U. Kerst, C. Boit, C.-C. Tsao, and T. R. Lundquist, “A Versatile Design of Solid Immersion Lenses in Bulk Silicon Using Focused Ion Beam Techniques,” in *Proceedings of ISTFA 2009*, 2009, pp. 119-125.

III P. Scholz, C. Gallrapp, U. Kerst, T. R. Lundquist, and C. Boit, “Optimizing focused ion beam created solid immersion lenses in bulk silicon using design of experiments,” *Microelectronics Reliability*, vol. 50, no. 9-11, pp. 1441-1445, Sep. 2010.

IV P. Scholz, U. Kerst, C. Boit, T. Kujawa, and T. R. Lundquist, “Developing a Chemistry-Assisted Focused Ion Beam Process for ‘ On-Demand ’ Solid Immersion Lenses in Silicon,” in *Proceedings of ISTFA 2010*, 2010, pp. 389-392.

V P. Scholz, U. Kerst, C. Boit, T. Kujawa, and T. R. Lundquist, “Instant Solid Immersion Lens creation in silicon with a Focused Ion Beam - comparing refractive and diffractive methods,” in *Proceedings of ISTFA 2011*, 2011, pp. 46-53

List of Tables

List of Figures